FOCUSED ION BEAM PATTERING FOR PHOTONIC AND SEMICONDUCTOR APPLICATIONS

THE APPLICATION OF FOCUSED ION BEAM TECHNOLOGY TO THE MODIFICATION AND FABRICATION OF PHOTONIC AND SEMICONDUCTOR ELEMENTS

By: CONNOR WONG, B. ENG.

Thesis Submitted to the School of Graduate Studies in Partial Fulfillment of the Requirements for the Degree Master of Applied Science

McMaster University © Copyright by Connor Wong, August 2020

McMaster University

Hamilton, Ontario

Department of Engineering Physics

MASTER OF APPLIED SCIENCE (2020)

TITLE: The Application of Focused Ion Beam Technology to the Modification and Fabrication of Photonic and Semiconductor Elements

AUTHOR: Connor D. Wong, B. Eng. (McMaster University)

SUPERVISORS: Dr. Andrew P. Knights, Dr. Nabil Bassim

NUMBER OF PAGES: 116

Abstract

Focused Ion Beam (FIB) technology is a versatile tool that can be applied in many fields to great effect, including semiconductor device prototyping, Transmission Electron Microscopy (TEM) sample preparation, and nanoscale tomography. Developments in FIB technology, including the availability of alternative ion sources and improvements in automation capacity, make FIB an increasingly attractive option for many tasks. In this thesis, FIB systems are applied to photonic device fabrication and modification, semiconductor reverse engineering, and the production of structures for the study of nanoscale radiative heat transfer.

Optical facets on silicon nitride waveguides were produced with plasma FIB (PFIB) and showed an improvement of 3 ± 0.9 dB over reactive ion etched (RIE) facets. This process was then automated and is capable of producing a facet every 30 seconds with minimal oversight. PFIB was then employed to develop a method for achieving local backside circuit access for circuit editing, creating local trenches with flat bases of 200 x 200 μm. Gas assisted etching using xenon difluoride was then used in order to accelerate the etch process. Finally, several varieties of nanogap structure were fabricated on devices capable of sustaining temperature gradients, achieving a minimum gap size with PFIB of 60 nm.

Acknowledgements

There are many people without whom this thesis would have either never existed or otherwise been significantly less entertaining to produce. First among these are my supervisors, Dr. Andy Knights and Dr. Nabil Bassim, who gave me the unexpected yet very welcome opportunity to do this degree. I can't thank them enough for making my life much more interesting than it might otherwise have been, as well as for being the best kind of supervisors.

I would like to thank Dr. Jonathan Bradley for his patience regarding my constant invasions of his lab. These projects wouldn't have been possible without a lot of time spent at those characterization setups.

Alex Krechmer, Alexander Sorkin, and Chris Pawlowicz from TechInsights for their collaboration, ideas, and support, and Alex in particular for an action-packed visit to the CCEM.

Dr. Maureen J. Lagos both for the opportunity to take part in his work and for being an all-round entertaining individual.

Sam Norris for not only showing me the ropes on PFIB but for being excellent conversation, a source of general liveliness, and a good friend.

Henry Frankis for answering a substantial number of questions, for generally being an enormous help, and for being very calm company.

Khadijeh Miarabbas Kiani for her aid in data collection, patience during the occasional long FIB night, and diverting conversation.

The faculty and staff of the Engineering Physics and Materials Science and Engineering departments, and the staff of the CCEM and CEDT for their support and for being excellent colleagues and equally excellent company.

Matei Banica for his work in developing direct write fabrication recipes. Not work for the faint of heart.

Dr. Ross Anthony and Dr. David Hagan for showing me how to run various things around the lab and for being characters that defined the group.

The members of Bassim Group for being good friends and companions on a number of memorable adventures. It was an honor and a pleasure.

Matt Vuk for all the long nights we sat waiting for the PFIB to destroy his waveguides, and for our bizarre adventures into playing go (of which I claim moral victory), to Ramis Arbi who completed our odd little trio for his willingness to entertain any idea no matter how unhinged, and to both of them for our business meetings that inevitably ended as jam sessions.

Lastly, I would like to thank the many friends who have ensured that my time here was time very well spent, my family for their unending support, and my fiancée for continuing to put up with me.

Table of Contents

Abstract iii
Acknowledgements iv
List of Figures viii
List of Figures in Chapter 2 x
List of Tables xi
List of Abbreviations and Symbols xii
Declaration of Academic Achievement xiv
Chapter 1: Introduction 1
1.1 Focused Ion Beam Technology 1
1.2 Optical Telecommunications and Silicon Photonics 1
1.2.1 Optical Facets and Loss 3
1.3 Heat Transfer 4
1.4 Backside Circuit Access 5
1.5 Research Objectives 7
1.6 Focused Ion Beam: Background and Theory 8
1.6.1 Basic Principles of FIB 8
1.6.2 Ion Sources 13
1.6.3 FIB Patterning 19
1.6.4 Gas Assisted Etching (GAE) 22
1.7 Nanoscale Heat Transfer 24
1.8 Automation in FIB 25
1.9 Semiconductor Reverse Engineering 26
1.10 Photonic Waveguides 27
1.10.1 Optical Loss in Waveguides 28
Chapter 2: FIB Optical Facets 29
2.1 Introduction 29
2.2 Background 29
2.3 Experiments and Results 37

2.4 Conclusions (FIB Facets) 44
Chapter 3: Nanoscale Heat Transfer 45
3.1 Introduction 45
3.1.1 Objectives 45
3.2 Experimental 46
3.2.1 Nanogaps: Basic Bridges 46
3.2.2 Thermal Gradients: Complex Bridges 53
3.2.3 Serpentine Structure 56
3.2.4 Heat Lens 58
3.3 Conclusions 62
Chapter 4: Backside Milling with PFIB 63
4.1 Introduction 63
4.1.1 Primary Objectives 64
4.2 Deep Trenches 65
4.3 Gas Assisted Etching 70
4.3.1 Experiments 70
4.4 Final Deep Trenches 77
4.5 OLED Cross-Section 83
5. Conclusions and Suggestions for Future Work 92
5.1 Future Work 92
References 94

List of Figures

Figure 1: Schematic of dual beam FIB-SEM instrument [20] 8
Figure 2: Schematics of LMIS FIB and ICP Source PFIB columns [21] 9
Figure 3: CASINO simulation of 2 keV electron beam in silicon (red indicates backscatter electrons) 10
Figure 4: FIB Sample Interaction and Collision Cascade [20] 11
Figure 5: SRIM simulation of collision cascades from 50 gallium and 50 xenon ions at 30 kV in silicon nitride at normal incidence 12
Figure 6: SRIM simulation of ion ranges for 100 gallium and 100 xenon ions at 30 kV in silicon nitride at normal incidence. 12
Figure 7: Table of Source Ions (2014) [23] 13
Figure 8: Gallium LMIS [24] 14
Figure 9: SRIM Simulation of 50 Gallium ions in Silicon at 30 keV 15
Figure 10: Inductively Coupled Plasma Source Mechanism [25] 16
Figure 11: SRIM Simulation of 50 xenon ions in silicon at 30 kV 17
Figure 12: Spot size (FWHM) vs. Beam Current using different sources [17] 18
Figure 13: Schematic of FIB milling process parameters for a raster scan [29]... 19
Figure 14: Material removal rates for several materials using gallium ions at 30 kV and normal incidence [31] 20
Figure 15: Measured and calculated sputter rates for gallium and xenon at 30 kV [16] 20
Figure 16: Schematic diagram of redeposition in low and high aspect ratio FIB trenches [29] 21
Figure 17: Single pass serial milling (left) vs. multipass parallel milling (right). [32] 22
Figure 18: Straight tube, angled tube [35], and beehive [36] GIS configurations 23
Figure 19: Far field and near field radiative heat transfer schematics [38] 25
Figure 20: Waveguide geometries [40] 27
Figure 21: Initial bridge structure concept 46
Figure 22: Protochip device schematic. Note the close-up view of the heating region. 46
Figure 23: Bridge 1 thinning process. Final width 500 nm. 47
Figure 24: Amorphization trials 1-6 48
Figure 25: Bridge 1 gap (~250 nm wide), and completed structure 49
Figure 26: Bridge 2 showing redeposition on the bridge, amorphized region, and gap side of ~102 nm 49
Figure 27: Smallest nanogap created with PFIB (~60 nm wide) 50

Figure 28: Six test structures produced to compare gap cutting methods. Site 1 cut with PFIB, Site 4 bridge collapsed during fabrication. 51
Figure 29: Site 1 gap image, top view. Note apparent connection. 52
Figure 30: Row A: Site 6 after second amorphization, gap at 0 degrees (top view), and gap at 52 degrees; Row B: New bridge, gap at 0 degrees (top view), and gap at 52 degrees 53
Figure 31: Bridge with barrier holes to reduce heat conduction. T1>T2. 54
Figure 32: Two modified barrier hole structures 54
Figure 33: Gaps on modified bridge structures 55
Figure 34: Characterization holes, close up, mid process, and end results 56
Figure 35: Serpentine bridge structure 56
Figure 36: Twisting of structure after cutting of support struts. 57
Figure 37: Serpentine structure nanogap, bird's eye view 57
Figure 38: Improved characterization holes 58
Figure 39: Heat lens bitmap 58
Figure 40: First heat lens trial. Note that the connective structure is very thin. ... 59
Figure 41: First completed heat lens structure. Note the beginnings of cracks in the membrane. 60
Figure 42: 0.9 scaled heat lens 61
Figure 43: 0.9 scaled heat lens structure 61
Figure 44: 0.9 scaled heat lens structure bridge gap 62
Figure 45: GIS chamber view and SEM view during operation 64
Figure 46: Trench 1: 300 x 300 x 108 μm rectangular mill at 2.5 μA at 12, 30, 60, 72, 120, and 182 minutes 65
Figure 47: Trench 2: Stepped trench done in four 50 μm deep rectangular steps 66
Figure 48: Base of Trench 2, notably smooth 66
Figure 49: Alicona Infinitefocus images and profiles for trenches 1 and 2 respectively. Red lines indicate scan direction for profile 67
Figure 50 Bird's eye view of trench sides A) 1, 2 B) 4, 5 C) 6, 7 D) 8, 9 68
Figure 51 Clockwise from top left: Site 7, deposited pad, close up of cross section, cross section 69
Figure 52 Site 8 and site 8 cross section displaying measurements of both steps 69
Figure 53 Initial xenon difluoride etch test 71
Figure 54 Close up of surface damage from initial GAE test 72
Figure 55: Site 12 GAE test, quality rating 1 74
Figure 56: Sites 18 and 19 GAE tests, ratings 5 and 4 respectively 74
Figure 57: Site 12 cross section 75
Figure 58 Final GAE Test site 26. Done in two steps, 100 microns deep in total. 76
Figure 59 Deep trench mill pattern, four steps 77
Figure 60 T1 50 micron lateral step trench 78

Figure 61 T2 25 micron lateral step trench, cross sectioned 78
Figure 62 T1 and T2 trench bases 79
Figure 63 T2 Cross section 79
Figure 64 T2 right side bottom geometry 80
Figure 65 T1 Cross section 80
Figure 66 T1 Centre surface 81
Figure 67 T1 Left side surface shape 82
Figure 68 Platinum deposition for resistance testing 83
Figure 69: Clockwise from top left: SEM view of cut, Ion beam view of cut, infrared chamber view, navigation camera view 84
Figure 70: Surface after initial mill. Note melted surface quality. 85
Figure 71: Close up of thermal glow captured by infrared chamber camera (4 mm marker is for stage navigation and does not indicate scale) 85
Figure 72: Cut at 25 hours, 16 minutes, 43 seconds 86
Figure 73: Completed cut at 52 degrees 87
Figure 74: Completed cut, bird's eye view 87
Figure 75: Completed cut at 25 degrees with tilt correction 88
Figure 76: First cleaning cross section at 1 μA 89
Figure 77: Both cleaning cross sections 90
Figure 78: Close up of cross section after polishing rounds 91

List of Figures in Chapter 2

Fig 1. Silicon nitride waveguide schematic (not to scale) 34
Fig 2. RSoft simulations of mode profile for silicon nitride strip guides of 1 and 1.2 micron widths 35
Fig 3. A) Etched silicon nitride facet, B) PFIB modified silicon nitride facet (15 nA current) 36
Fig 4. Initial test results comparing etched, FIB at 1 nA, and FIB with an additional 0.1 nA FIB polish cut step on 1 cm guides 37
Fig 5. Cutback measurement results 39
Fig 6. Visual comparison of facets produced with varied FIB currents 40
Fig 7. Total loss vs. current measurements for guides of 3 lengths 40
Fig 8. Automation process flow chart 42
Fig 9. FIB facets produced with iFast automation routine at 15 nA 43
Fig 10. Cutback measurements with 15 nA automated routine in tellurium oxide coated silicon nitride 43

List of Tables

Table 1: Milling Current vs. Time..... 37
Table 2: Loss vs. Length Curve Constants 39
Table 3: Loss vs. Length Constants (Automation Routine) 44
Table 4: GAE Results 73

List of Abbreviations and Symbols

CASINO – Monte Carlo Simulation of Electron Trajectory in Solids

CCEM – Canadian Centre for Electron Microscopy

CEDT – Centre for Emerging Device Technologies

DBR – Distributed Bragg Reflector

FIB – Focused Ion Beam

FIB-SEM – Dual Beam System

GAE – Gas Assisted Etching

GIS – Gas Injection System

ICP – Inductively Coupled Plasma

ICT – Information and Communications Technology

LMIS – Liquid Metal Ion Source

PFIB – Plasma Focused Ion Beam

SEM – Scanning Electron Microscope

Si_3N_4 – Silicon Nitride

SiO_x – Silicon Oxide

SRIM – Stopping and Range of Ions in Matter

TEM – Transmission Electron Microscope

TeO_2 -Tellurium Oxide

WDM – Wavelength Division Multiplexing

XeF_2 – Xenon Difluoride

Declaration of Academic Achievement

I, Connor Wong, declare that this document was written by my hand, and that its contents are primarily my own work with contributions from others as listed here:

- Design and simulation of silicon nitride waveguides carried out by Bradley Group at McMaster University
- Fabrication of silicon nitride waveguides by Lionix
- Initial method for silicon waveguide production by direct writer developed by Matei Banica at McMaster University
- Designs for heat transfer test structures initially developed by Dr. Maureen J. Lagos at McMaster University
- Designs for Bragg gratings determined from simulations by Bruno Frare at McMaster University
- Assistance with Rsoft simulations provided by Arthur Méndez-Rosales and Henry Frankis at McMaster University
- Gas Assisted Etching rate determination conducted in collaboration with Alex Krechmer from TechInsights
- Mill rate experiments conceived in collaboration with Alex Krechmer, Alexander Sorkin, and Chris Pawlowicz from TechInsights
- Optical detector devices and modification designs provided by Dr. David Hagan

All electron microscopy and FIB work was conducted at the Canadian Center for Electron Microscopy (CCEM) at McMaster University.

Chapter 1: Introduction

1.1 Focused Ion Beam Technology

Focused ion beam (FIB) is not a new technology. Initially developed in the 1970s, FIB technology has found application in a number of fields, and widespread use has fueled the development of a variety of hardware and software options for the instrument. [1] It is now common to combine the FIB with an electron beam, giving it additional imaging capacity. This combination, referred to as a dual beam system or FIB-SEM (scanning electron microscope) is ubiquitous with the exception of specialized single beam instruments. Dual beam FIB systems have many uses, being capable of multiple imaging configurations, milling, and deposition. From their original purpose as lithography mask editing tools, FIB systems have come to be applied to a diverse array of tasks, including prototyping and failure analysis, tomography, sample preparation for TEM and atom probe microscopy, and more. [2] This thesis demonstrates the application of FIB to a variety of projects in photonic and semiconductor fabrication for potential research and industrial applications. From optical facets to the production of structures for nanoscale heat transfer experiments, FIB has much to offer.

1.2 Optical Telecommunications and Silicon Photonics

In a civilization that has become increasingly reliant on the informational otherworld that is the internet, the maintenance of the vast network of data that drives the day-to-day operation of our societies is of paramount concern. Ever

growing and ever consuming, this ethereal idiot savant is dependent on a prosaic reality, that of data centres and network infrastructure. While it is easy to be distracted by the promise of nigh unlimited utility and an endless cascade of beguiling illusions, it is these physical realities with which we must concern ourselves, and their real consequences that we must consider. Data centers, and more broadly information and communications technology (ICT) already use a substantial amount of the world's electricity, consuming approximately 4.6 percent in 2012 [3], and projected to consume anywhere from 8% to 21 % by 2030. [4] There are several strategies in place for increasing data center efficiency, including passive cooling measures, weather matching temperature control, moving to "hyperscale" infrastructure, and more, all of which contribute to reductions in power consumption. Despite the promise these methods have shown in terms of curbing increased power usage, demand remains significant, increasing from 500 000 centres in 2015 to greater than 8 million in 2019. [5] This hunt for efficient alternatives to traditional ICT has brought silicon photonics, first investigated in the 1960s, back into the spotlight.

Integrated silicon photonics is to fiber optic cable what an integrated circuit is to electrical cable and possesses similar advantages in terms of production and miniaturization. This low-cost high-volume production advantage is very much the key to extracting value from silicon photonics, as not only does it follow the same wafer scale processing trend, it benefits directly by making use of existing CMOS processing technology and facilities, gaining a significant leg up on development.

While silicon is not without its challenges as a base material, production of on chip light sources, detectors, and modulation to name a few, there is substantial interest in finding solutions due to its ubiquity and convenience, and they are heavily offset by the benefits of high density integration and the bandwidth offered by wavelength division multiplexing (WDM). [6]

There are a multitude of areas where silicon photonics has been implemented or shows great promise, including optical interconnects in data centres, fully integrated optical systems, and the elusive optical computer. A 2013-2024 estimate of the silicon photonics market value placed it at approximately USD 122 million, a target that based on valuations of the 2018 market at this time was heavily exceeded, with the 2018 market estimates ranging from USD 740 million to USD 800 million and expected to continue rising. [7] [8]

To deliver on the efficiency improvements these developments offer, optical loss must be minimized. As such, these technologies all rely on optical facets as the coupling of light from one component to another is an inevitable necessity of photonic systems, and on continuing research efforts. This brings us to the primary motivation driving the work presented in the second chapter of this thesis: the convenient production and modification of optical facets for research purposes.

1.2.1 Optical Facets and Loss

Optical facets for academic and industrial use are produced in a variety of ways. The methods of note include etching, cleaving, dicing, polishing, combinations of the above, and even mechanical milling. [9] [10] Cleaving produces high quality facets but requires additional scoring steps, and when employed on SOI devices requires additional etch steps. [11] Dicing and polishing is widely used but polishing steps are cumbersome, requiring sample stacking and bonding, though it may be possible to achieve good quality facets without polishing if the dicing parameters are optimized. [12]

It would be very convenient to have a method of facet preparation that isn’t reliant on the crystallographic cleavage planes associated with brittle fracture in semiconductors, doesn’t require additional masking or wet steps, is adjustable

enough to account for small variations in facet location, can be applied at various points during processing, and can reliably produce workable quantities of facets in a reasonable amount of time. For this, we turn to the FIB.

Using a FIB to produce optical facets is, like the FIB itself, not a new concept [13], but it is notable that FIB technology has now matured to the point at which automating simple processes is now reasonably accessible, and that with this maturation of the instrument, new options for ion sources have become available. Gallium, the traditional source for FIB instruments and the source used in other attempts to produce optical facets [14] with FIB has been shown to have adverse effects on photonic device function. In addition to the inevitable amorphization it has been shown that gallium tends to channel and may act as a dopant in III-V devices, necessitating post-process annealing steps or etching. [15] The system used for the work presented in this thesis was a Thermo Fisher Helios G4 uXe Plasma Focused Ion Beam (PFIB) with an inductively coupled plasma (ICP) of xenon gas as an ion source. Xenon is attractive for several reasons. Its larger size makes it less likely to channel, it is less likely to interact chemically with the sample [16], and in a more macroscopic sense the ICP source has a much longer lifetime (on the order of years in contrast to the approximately 1500 hours offered by a traditional gallium LMIS) and can sustain larger ion currents, though at the cost of a slightly larger (~30 nm) probe size at lower currents. [17] This combination of characteristics could potentially enable much greater success in applying FIB technology to photonic device fabrication.

1.3 Heat Transfer

Radiative heat transfer has long been considered a well understood field, primarily based on the assumption that Planck's law was sufficient as an explanation for the vast majority of heat transfer phenomena. This assumption has in recent years been

proven false, as when the dimensions involved are smaller than the thermal wavelength, Planckian limits may be violated.

The study of radiative heat transfer on this scale requires the production of test structures with the relevant dimensions that can sustain a temperature gradient. This thesis investigates the use of FIB as a convenient tool for prototyping and fabricating said structures. With FIB, designs for test structures can be rapidly modified and investigated, providing a high degree of customizability.

1.4 Backside Circuit Access

With the advent of the semiconductor industry, semiconductor failure analysis became a vital and profitable field with uses including prototyping, reverse engineering, and more. With FIB, circuits can be edited on a working device without compromising functionality, allowing the operator to cut interconnects, deposit new connections, and lay down contact pads where necessary. This is very useful when prototyping, as it allows modifications to the circuit to be tested without requiring a new photolithography mask, an expensive mask that must be carefully crafted with very high precision in the semiconductor fabrication process. Circuit editing is a similarly powerful tool for reverse engineering devices, as unknown connections can be probed, and predicted paths verified. It can even enable the operator to manually bypass internally designed device security. Unfortunately, there is a caveat to these applications. In modern devices there are often many metal layers. This introduces the problem of accessing the desired device components without destroying the device or tampering with the scene, as it were. This is achieved by gaining backside access, either by bulk removal of the substrate or by creating an access trench.

These two broad approaches must overcome several challenges. The first challenge, impacting bulk and local delayering, is that chips are often bowed in their mounts (primarily due to thermal expansion coefficient mismatch between the chip and packaging, or the between the substrate and metal components) [18], meaning that removal methods that do not take this into account tend to damage parts of the circuit before exposing the entire area of interest. This makes bulk removal slightly more difficult, as the method must take into account the topography of the entire chip. This has been done in the past by probing the surface, with either a physical probe or with lasers and building a contour map before using a CNC mill to remove the bulk. Other methods of bulk delayering include: 1) wet chemical etching, which introduces many variables to account for; 2) dry etching, which introduces potential etch artifacts and heating; 3) lapping, which is not particularly sensitive to topography; and 4) ion milling, which is generally suitable only for very thin samples. [19]

Local delayering avoids the added requirement of mapping the surface provided the trench is perpendicular to the surface at the region of interest. As a method, local delayering is desirable as it allows the user to retain the intrinsic heat sink provided by the substrate material. If the device is required to be fully operational post modification, this is a significant benefit.

Local delayering can be accomplished using several methods. These include the methods used for bulk delayering - albeit with some added masking steps or greater precision requirements - but with the addition of FIB. While it is ill suited to bulk removal, FIB can be used for local delayering as this requires significantly less material removal. For a traditional gallium LMIS FIB, the time required to mill away a meaningful thickness of substrate (100-600 μm) would remain prohibitive but using a high current instrument such as a xenon ICP FIB the process becomes feasible. If gas assisted etching can be used to supplement the beam, FIB is even more feasible.

1.5 Research Objectives

FIB is a versatile tool that today comes in many forms and is well positioned to find its way into new fields. As the work presented in this thesis will show, new varieties of FIB could be the key that unlocks a world of new options for semiconductor and photonic device fabrication.

The research objectives of this thesis are as follows:

- Reducing loss on optical facets, expediting and automating the process
- Developing a recipe for cutting trenches through full depth devices for backside circuit access using PFIB
- Developing a method for producing nanogaps with measurable thermal gradients

1.6 Focused Ion Beam: Background and Theory

1.6.1 Basic Principles of FIB

Both SEM and FIB systems consist primarily of a column which contains the electron or ion source and lenses for columnating, directing, and focusing the beam, as well as a vacuum chamber which contains the sample and various forms of electron and ion detector.

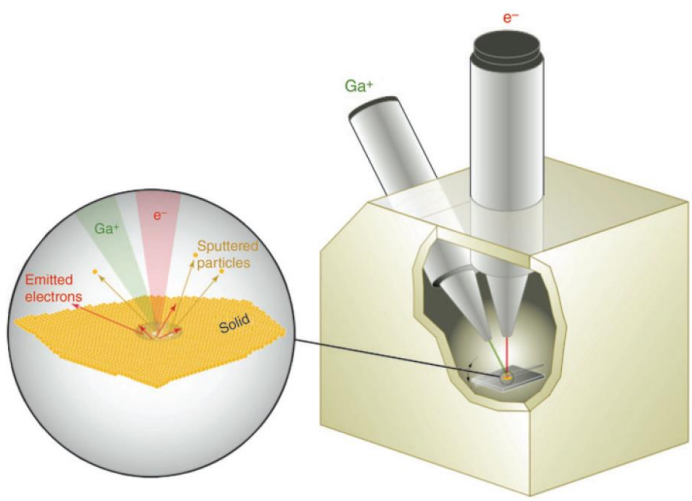

Figure 1: Schematic of dual beam FIB-SEM instrument [20]

These components form a system somewhat analogous to those used in optical systems, giving rise to their description as electron or ion optics. The key conceptual difference in the application of these systems is that the goal of SEM and FIB optics is to focus the source onto the sample, rather than onto the eye.

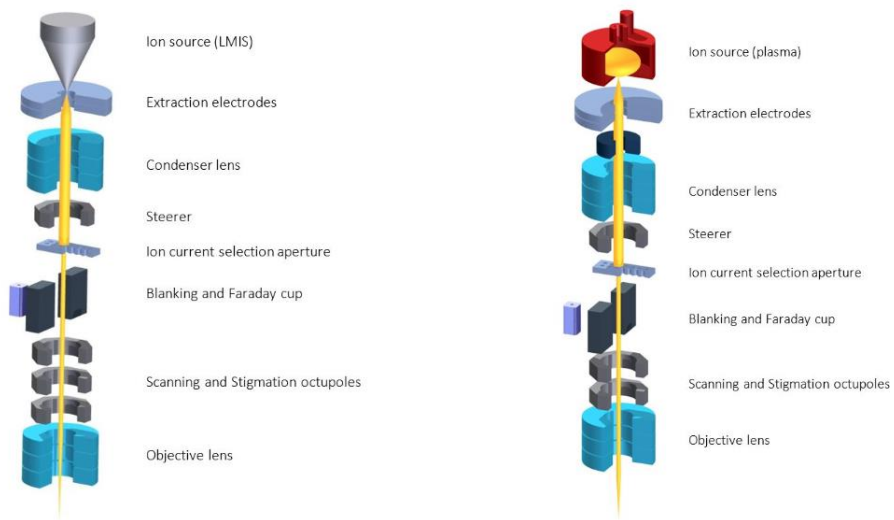

Figure 2: Schematics of LMIS FIB and ICP Source PFIB columns [21]

Both systems work by de-magnifying the source image onto the sample, and then rastering the beam across the sample surface. The products of the interaction between the beam and the sample are then collected by a variety of detectors.

In the case of SEM, rastering the beam across the sample will (depending on the beam and sample characteristics) produce a variety of elastic and inelastic scattering events, including the production of secondary, Auger, and backscatter electrons, x-rays, and phonons, all occurring within a certain interaction volume. Below is a simulation of a 2 keV electron beam interacting with silicon using Monte Carlo Simulation of Electron Trajectory in Solids (CASINO). [22]

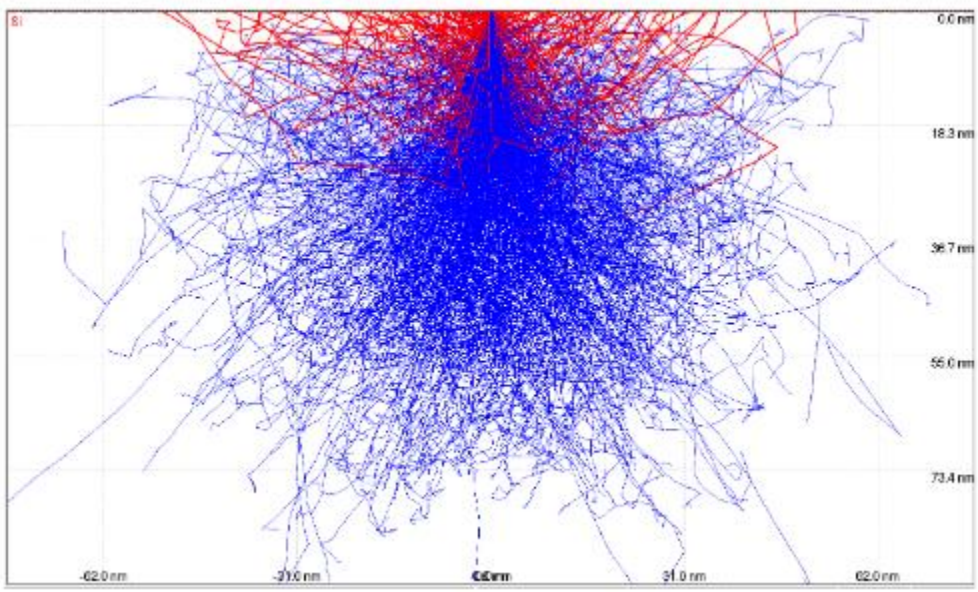

Figure 3: CASINO simulation of 2 keV electron beam in silicon (red indicates backscatter electrons)

The range of a given incident electron is determined by both the beam and sample characteristics and can be described in the following form:

$$R = 2.76 \times E_0^{1.67} \times \left(\frac{A}{\rho \times Z^{0.89}}\right)$$

Where R is the range in nm, E_0 is the accelerating voltage in kV, A is the atomic weight, ρ is the density, and Z is the atomic number of the sample.

In the case of FIB, the interaction of the beam with the sample will produce secondary electrons, recoiled ions, and sputtered substrate particles (secondary ions) and leave some source ions mostly implanted in the sample lattice (at normal incidence). This process is illustrated below in Figure 4.

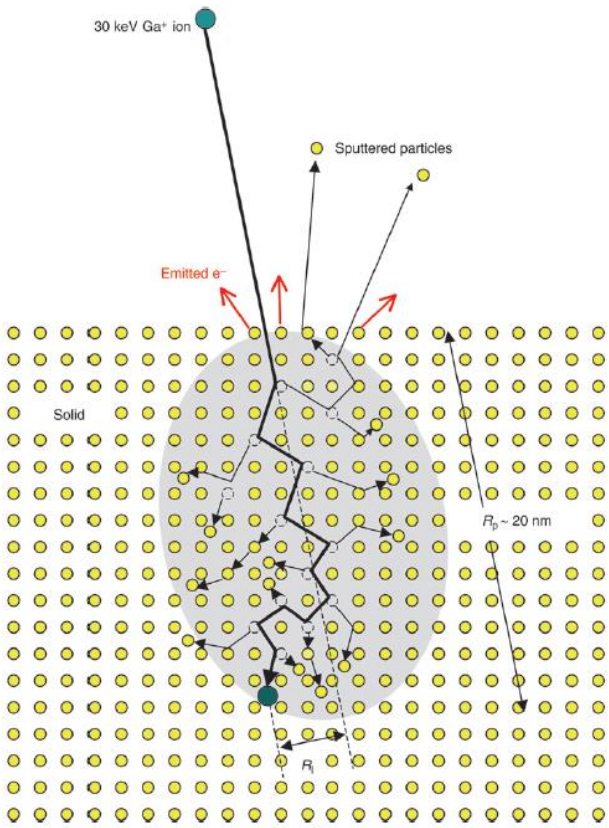

Figure 4: FIB Sample Interaction and Collision Cascade [20]

Also illustrated in Figure 4 is an effect called a collision cascade. Collision cascades are the result of energy transferred from an incident ion displacing an atom from the target (subsequently called a primary knock-on), which may then displace another atom in turn and so on until the energy is expended. With sufficient irradiation by the beam, this will result in the amorphization of the sample lattice to the depth of the cascade. FIB milling takes advantage of the localized sputtering that occurs on impact to deliberately remove material wherever the beam is rastered.

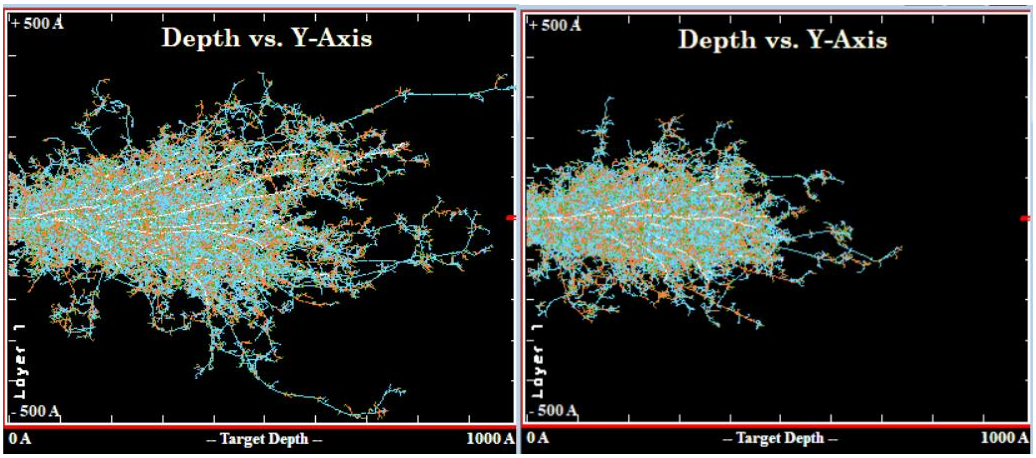

Figure 5: SRIM simulation of collision cascades from 50 gallium and 50 xenon ions at 30 kV in silicon nitride at normal incidence

Shown above are Stopping and Range of Ions in Matter (SRIM) simulations of collision cascades in silicon nitride resulting from 50 gallium and 50 xenon ions with an accelerating voltage of 30 kV at normal incidence. Note that the lattice damage (and the eventual amorphized layer) caused by the gallium ions extends more deeply into the sample.

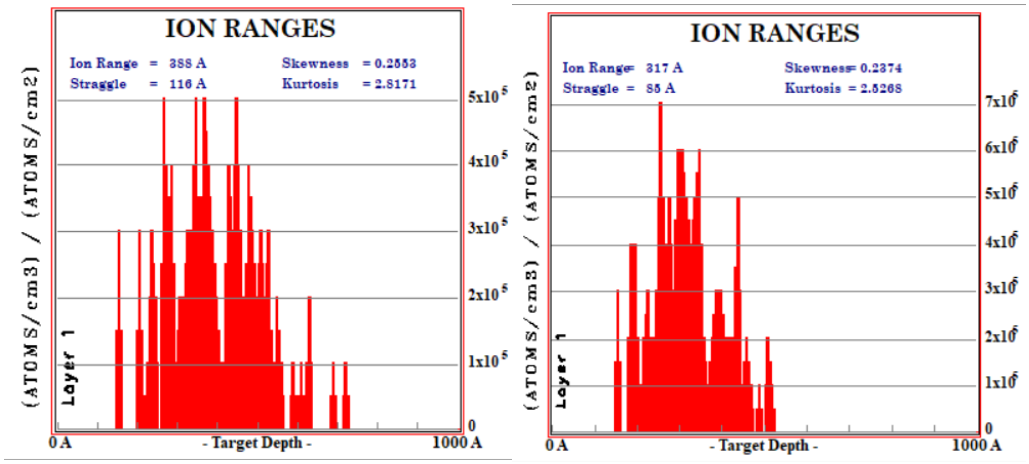

Figure 6: SRIM simulation of ion ranges for 100 gallium and 100 xenon ions at 30 kV in silicon nitride at normal incidence.

1.6.2 Ion Sources

Given the variety of applications of FIB-SEM, it should be evident that different species of ion produced by different physical mechanisms may be appropriate for different tasks. The following subchapter will investigate the mechanisms, advantages, and drawbacks of various ion sources used in contemporary FIB devices. Below is a table containing many of the ions currently available in FIBs and their respective source mechanisms.

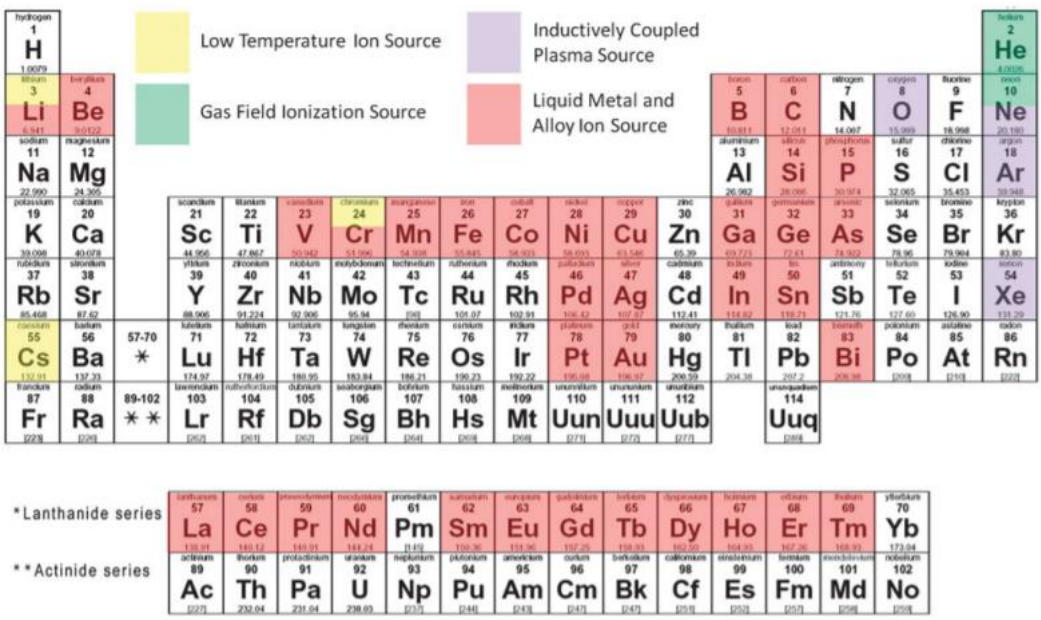

Figure 7: Table of Source Ions (2014) [23]

Liquid Metal Ion Sources (LMIS)

The most common ion source in FIB devices is the gallium Liquid Metal Ion Source or LMIS. Seen in Figure 8, a LMIS source consists of a relatively dull tungsten needle (with a 10 μm end radius) wrapped in a gallium coil that is heated by the

application of a high current. With the appropriate current settings, the gallium will melt and wet the needle, forming a pointed liquid cone at the end called the Taylor cone, with an end radius of approximately 5 nm. [23]

As the extractor voltage is increased, the field will pull an axial spray of gallium ions down towards the aperture. The system is relatively robust and can emit currents ranging from picoamps to near microamps. The relative system simplicity and reasonably long lifetime (1500 hours or more) make the gallium LMIS a reliable option as an ion source. Gallium itself, having a low melting point, low vapour pressure, sufficient size for sputtering, and being relatively non-reactive makes is a very attractive choice as a source ion.

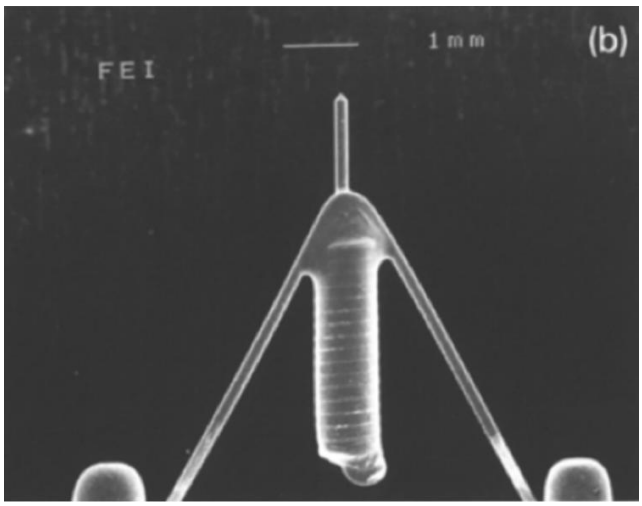

Figure 8: Gallium LMIS [24]

The downsides of gallium sources include; gallium implantation, as it will remain embedded in the target lattice, potentially acting as a dopant atom; and lattice damage. Sufficient irradiation with a gallium beam will amorphize the lattice near

the surface (a simulation of gallium interacting with a silicon target can be seen below in Figure 9).

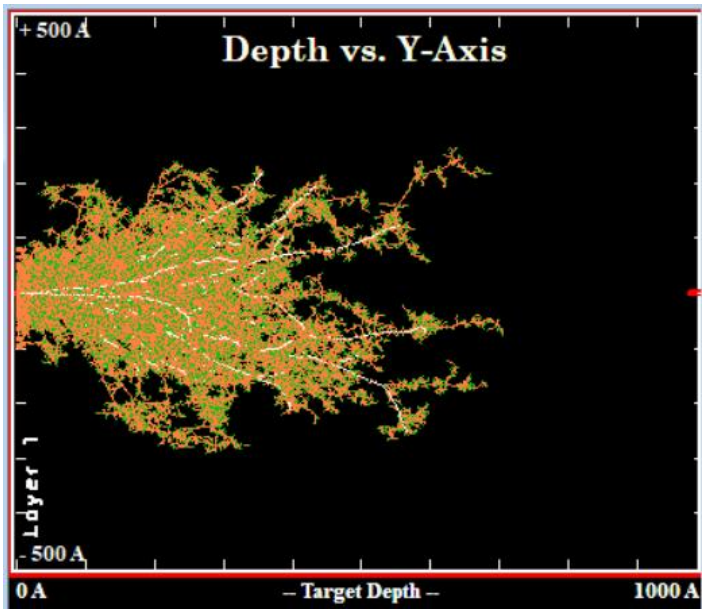

Figure 9: SRIM Simulation of 50 Gallium ions in Silicon at 30 keV

Inductively Coupled Plasma (ICP)

With tomography being a key application of FIB technology, there is demand for FIB configurations that allow for removal of material at a variety of scales. While the traditional Ga LMIS source works well for milling on the tens of microns length scale, and laser ablation can be used for millimeter scale work, the inductively

coupled plasma (ICP) source FIB (PFIB) handles the middle ground, being capable of working on the hundreds of microns and up to the millimeter scale.

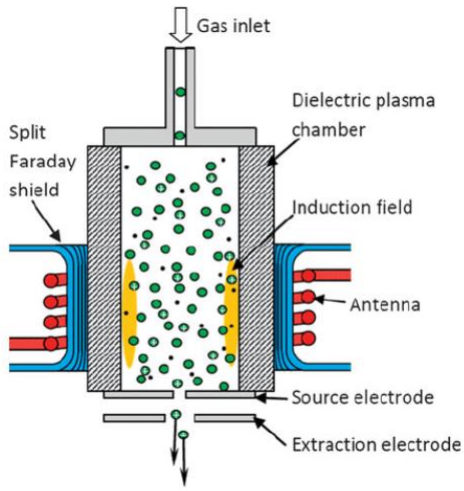

Figure 10: Inductively Coupled Plasma Source Mechanism [25]

The operating principle of current plasma sources is the creation of inductively coupled plasma. To achieve this, gas is fed into a chamber, which is wrapped in a coiled RF antenna. A time varying current with a frequency below the electron plasma resonance frequency but above the ion plasma resonance frequency is passed through this antenna and the resulting electromotive force will sufficiently accelerate electrons around the outer edge of the chamber to cause ionization of the gas. The ions are then accelerated out using a series of electrodes.

As mentioned in the introduction, xenon has been used for ICP sources for some time. A simulation of the collision cascade from 50 xenon ions with an accelerating voltage of 30 kV at normal incidence in silicon can be seen below.

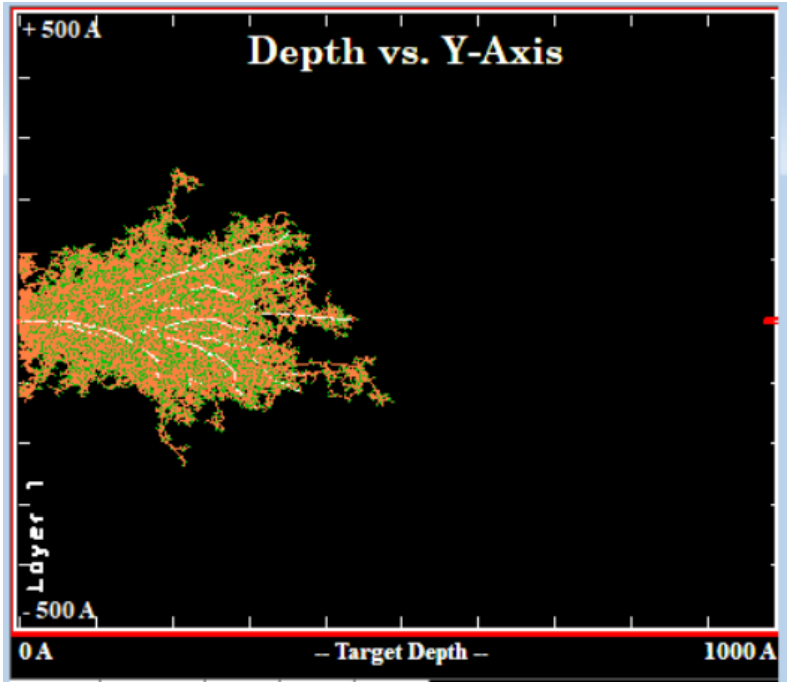

Figure 11: SRIM Simulation of 50 xenon ions in silicon at 30 kV

This collision cascade is notably shallower than that resulting from gallium (shown in Figure 9).

The primary advantages of PFIB include the aforementioned large scale material removal due to high beam current (significant amounts of xenon ions can be produced, but the source size is much smaller than the 5 nm tip of a LMIS source), long term continuous operation due to minimal aging of the ICP chamber (approximately two years [25]) less lattice damage and implantation due to the gases used, and an arguably limitless supply of ions as long as gas reserves are maintained.

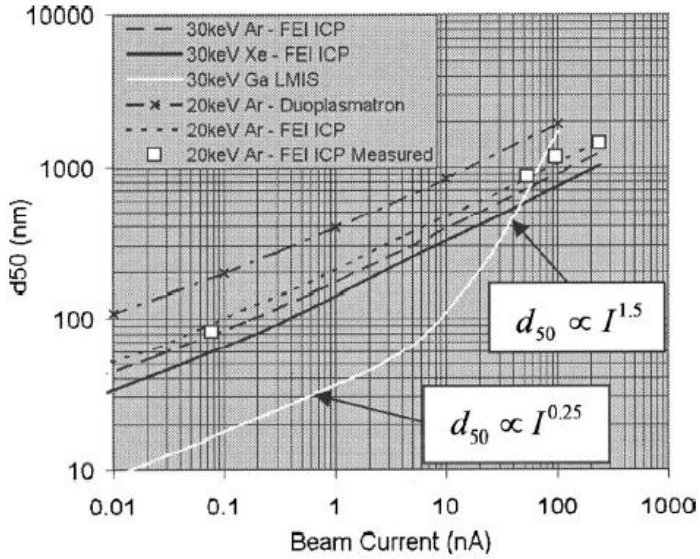

Figure 12: Spot size (FWHM) vs. Beam Current using different sources [17]

While a PFIB still produces larger spot sizes at low current and lower source brightness than its LMIS counterpart, its advantages make it a valuable addition to the field.

Other Sources

There are several other varieties of ion source including Gas Field Ionization Sources (GFIS), Liquid Metal Alloy Ion Sources (LMAIS), Ionic Liquid Ion Sources (ILIS), Magneto Optical Trap Ion Sources (MOTIS), and Low Temperature Ion Sources (LoTIS). These sources offer a range of different options for ion species and beam characteristics, with GFIS offering high brightness and reduced damage for imaging purposes at the cost of low source stability and poor milling yield [26], LMAIS allowing selection between multiple ion species from the same source (using a Wein filter) at the cost of reduced current [27], ILIS offering immense diversity of mass and chemical properties at the cost of reduced source stability and less established methods [28], and MOTIS/LoTIS offering

unusual source materials, high resolution, and low beam energy at the cost of reduced beam current.

1.6.3 FIB Patterning

Milling Parameters

Milling with the PFIB involves the modification of several parameters. These include the beam current (and current density), dwell time, the beam overlap (pitch), scan direction, and scan pattern.

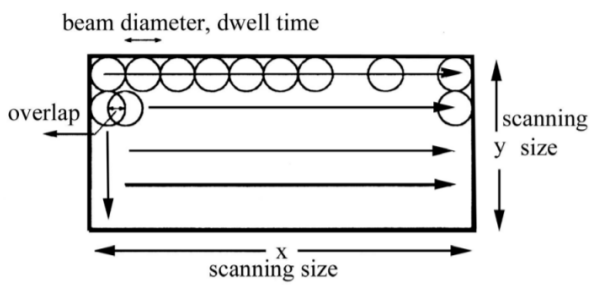

Figure 13: Schematic of FIB milling process parameters for a raster scan [29]

Milling depth in a homogenous target at normal incidence can be described as follows: [30]

$$Depth = n \times (I \times T) \times \frac{A}{\Delta x \times \Delta y} \times R \times \frac{1}{A}$$

Where n is the number of passes, I is the FIB current, T is the dwell time, A in both instances is the total area of the pattern, Δx and Δy are the pitch in the x and y directions respectively, and R is the material removal rate. The material removal rate (in μm^3/nC) is constant for any given material and can be predicted with SRIM or experimentally determined by milling a set pattern and cross-sectioning that pattern (again using the FIB) to measure the depth of the mill. SRIM predictions

tend to overshoot as SRIM does not account for redeposition (see below). [31] Tables of several such values are provided below.

Material	Volume per dose (μm³/nC)			
	Average	Minimum	Maximum	SRIM
Aluminum	0.29	0.11	0.47	0.44
Brass (C27400)	0.30	0.21	0.44	1.09
Phosphor bronze (C52100)	0.20	0.08	0.33	0.77
Titanium	0.46	0.33	0.59	0.22
Lead	2.87	2.44	3.35	2.35
Stainless steel (AISI302)	0.32	0.29	0.36	0.43
Silicon	0.24	0.22	0.26	0.35

Figure 14: Material removal rates for several materials using gallium ions at 30 kV and normal incidence [31]

Material	Sputter rate measured (μm³/nC)		Sputter rates calculated from SRIM (μm³/nC)	
	Ga^+	Xe^+	Ga^+	Xe^+
Diamond	0.09	0.11	0.07	0.09
Si	0.22–0.27	0.35–0.42	0.27	0.37
Al	0.31	0.41	0.37	0.5
Ti	0.31	0.32	0.26	0.28
GaAs	0.86	0.61	1.45	1.61
Cu	0.15–0.55	1.1–1.6	0.69	0.85
Epoxy resin	0.3	0.31	–	–

Figure 15: Measured and calculated sputter rates for gallium and xenon at 30 kV [16]

Redeposition

When material is sputtered by the ion beam, it will redeposit on any surface that can be reached in a straight line in or around the milling area. This phenomenon is known as redeposition and must be accounted for when using the FIB for patterning

tasks. Redeposition introduces a limitation on the aspect ratio of milled trenches, as eventually the sputtered material will be unable to escape the trench. Generally speaking, the maximum aspect ratio achievable with an unassisted FIB beam is 5:1.

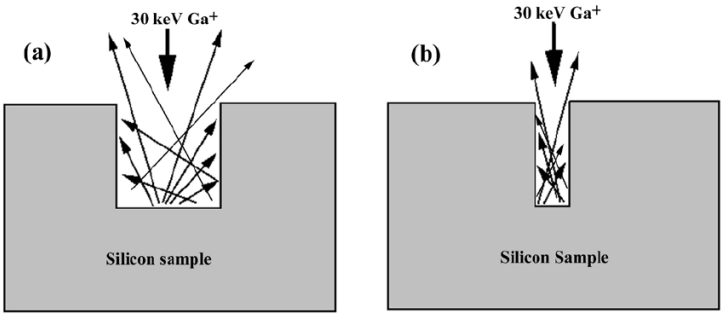

Figure 16: Schematic diagram of redeposition in low and high aspect ratio FIB trenches [29]

Another important aspect of redeposition relates to the beam scan parameters. The direction and type of the scan will affect the geometry of the milled area. Below are images comparing single pass and multipass milling strategies for the creation of 100 nm wide microfluidic trenches with the same current and dose, but with that dose broken into passes of shorter duration for the multipass. Note that in the case of the single pass method, redeposition has significantly affected the trench geometry. The multipass method in this case evades redeposition both by having shorter pixel dwell times (which reduce the effect of the beam profile on the trench topography), and by milling in parallel, preventing non-uniform buildup of redeposited material across the structure. [32]

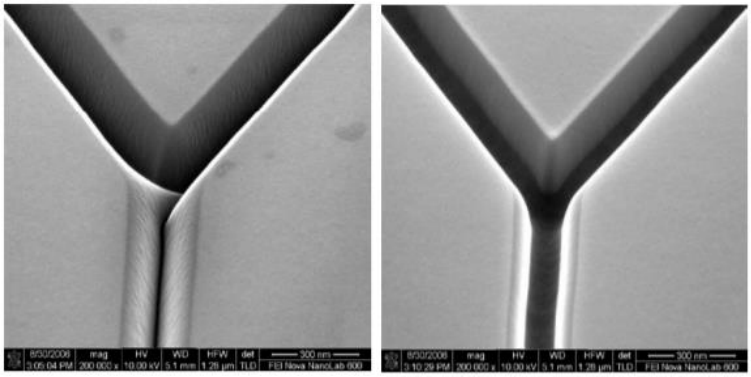

Figure 17: Single pass serial milling (left) vs. multipass parallel milling (right). [32]

1.6.4 Gas Assisted Etching (GAE)

Gas assisted etching (or deposition) involves the introduction of a gas from a reservoir to the chamber by way of a nozzle of some configuration (the system as a whole may be referred to as a gas injection system or GIS). After becoming adsorbed on the sample surface, the gas is then dissociated by the (in this case) ion beam, after which the dissociated products will interact chemically with the sample. Many different molecules can be introduced to the chamber, and thus a variety of options for deposition or etching can be accessed, contributing significantly to the overall flexibility of FIB as an instrument. Important factors include the gas flux to the substrate, generally determined by nozzle geometry and position and gas flow rate, and the spatial distribution of the flux that results from the same factors. [33] It is also important to know the efficiency with which dissociated molecules are replaced by new molecules as this will determine whether the operation is limited by the supply of gas or the supply of ions. [34]

Gas nozzles can take a variety of forms. These include straight nozzles tubes (such as the GIS employed on the Helios PFIB used for the work in this thesis), angled tubes, and beehives.

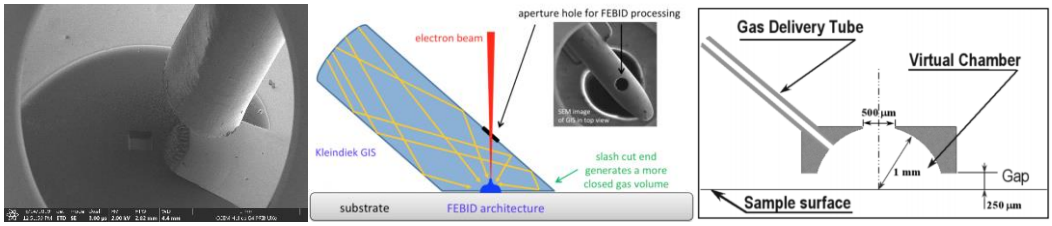

Figure 18: Straight tube, angled tube [35], and beehive [36] GIS configurations

Straight tubes, though simple, robust, and maneuverable suffer from asymmetrical flux and shadowing effects. While the asymmetry in the flux can be minimized by keeping the nozzle at a higher angle of incidence, the shadowing issue remains, especially as it pertains to high aspect ratio etching. [33]

Etch Parameters

Modelling the etch yield for gas assisted processes is somewhat complex. Using a model developed by L. R. Harriot in 1993 for GAE using a digital scan, the etch yield can be written as follows: [37]

$$Y = s\frac{N}{N_0} = \frac{sgF}{N_0}\left[\frac{\left\{1 - exp((\frac{1}{\tau_e} + \frac{1}{\tau_r})t_r)\right\}}{\frac{1}{\tau_e} + \frac{1}{\tau_r}} e^{\frac{-t_p}{\tau_p}} + \frac{1}{(\frac{1}{\tau_e} + \frac{1}{\tau_r} + \frac{1}{\tau_p})}\right]$$

Where s is the maximum yield in atoms per incident ion (the number of reacted surface atoms that can be removed by a single ion), N is the surface density of gas molecules, N_0 is the density of available adsorption sites, g is the sticking probability, F is the gas flux, τ_e is the surface residence time (relating to evaporation), $\tau_r = \frac{N_0}{gF}$ and is the refresh time constant, t_r is the refresh time (time between pixel exposures), t_p is the dwell (exposure) time, and τ_p is the exposure time constant, defined as follows:

$$\tau_p = \frac{N_0}{msI}$$

Where m is the number of gas molecules required to remove one substrate atom, and I is the ion flux (which is considered to be constant with respect to time at each dwell point).

Harriot's model also indicates that the optimal yield will be when the surface layer of adsorbed gas saturates fully during the refresh time, however this model assumes that dissociation requires interaction with the beam. As xenon difluoride (the etch gas used for the work presented in this thesis) is able to dissociate without the assistance of the beam, some modification to the effect may be expected.

Using some assumption regarding the possible values for ion flux, gas flux, and evaporation constants, as well as the aforementioned assumption regarding the maximum yield conditions, the yield equation can be reduced to the following form:

$$Y = se^{\frac{-t_p}{\tau_p}} + \frac{g}{m}\left(\frac{F}{I}\right), t_r \gg \tau_r$$

Harriot also notes that for process control it may be helpful to keep the pixel dwell time significantly longer than the dwell time constant so that the yield is dependent only on the gas and ion fluxes:

$$Y = \frac{g}{m}\left(\frac{F}{I}\right), t_p \gg \tau_p$$

1.7 Nanoscale Heat Transfer

Radiative heat transfer in the near field regime can be differentiated by the significant contribution from tunneling evanescent waves that is not predicted by Planck's law. Mathematically, the process can be described as follows in accordance with the work conducted by Polder and Van Hove in their paper 'Theory

of Radiative Heat Transfer between Closely Spaced Bodies' considering a system of two infinite, parallel isotropic plates separated by a vacuum gap with temperatures T_1 and T_3 where $T_1 > T_3$:

$$Q = \int_0^\infty \frac{d\omega}{2\pi}[\Theta(\omega, T_1) - \Theta_3(\omega, T_3)] \int_0^\infty \frac{d\omega}{2\pi} k\tau(\omega, k, d)$$

In which Q is the net radiative power per unit area exchanged between the plates, ω is the radiation frequency, d is the distance between the plates, and k is the magnitude of the wave vector parallel to the surface planes as per:

$$k = \sqrt{k_x^2 + k_y^2}$$

The second integral covers all values of k including values of k where k > ω/c which represent the evanescent wave contribution. τ(ω, k, d) is the total transmission probability of the waves, which for k > ω/c has a negative exponential dependence on 'd', giving rise to the non-Planckian near field effects.

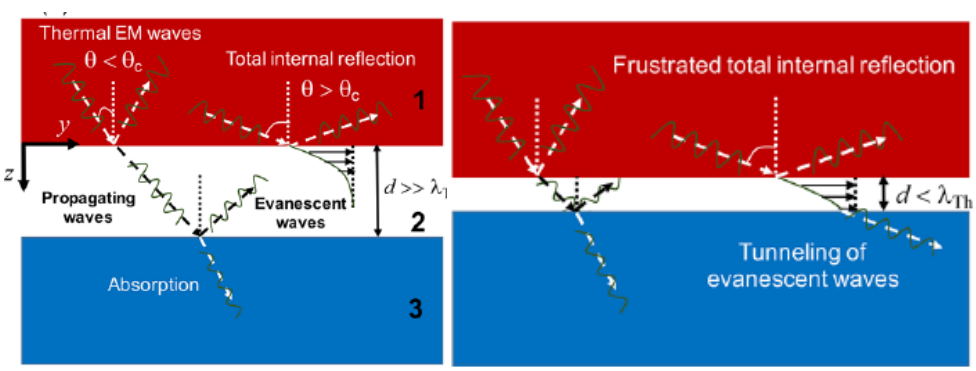

Figure 19: Far field and near field radiative heat transfer schematics [38]

1.8 Automation in FIB

As FIB hardware has developed, so too has FIB software. With newer generation FIB machines, manufacturers have begun to include many software options for a

variety of tasks, including improvements to lithography tools, automated routines for TEM sample preparation, and more convenient UIs for the development of automated processes (such as iFast, the UI provided by ThermoFisher used for the work presented in this thesis). Using pattern matching, drag and drop process development, and some python scripting, it is now very possible to automate processes that would traditionally have required painstaking operator oversight.

In the use of FIB for photonic applications, particularly the modification and improvement of optical facets, manufacturability has been a significant issue. The use of automated routines that can find, target, and execute an operation on a desired device component makes for a significant reduction in process time and required oversight.

1.9 Semiconductor Reverse Engineering

In a field as competitive and fast-paced as the semiconductor industry, garnering an understanding of the systems being used by the competition is an important capacity to have. Because of this, semiconductor reverse engineering has become a significant field.

In order to reverse engineer an integrated circuit device, there are several steps that must be taken. Generally, devices are disassembled and analyzed on a number of levels, starting with the 'macroscale' hardware such as circuit boards in which the packaging and primary components are determined (teardown). This is followed by the investigation of signal paths and operation (system level analysis), delayering to transistor level and mapping components in order to create circuit schematics (circuit extraction), and ending with the determination of materials and fabrication methods used (process analysis). Many different tools and methods are used in

order to complete this process. Of these steps, circuit extraction is the one relevant to this thesis.

In order to extract the circuit, the packaging must first be removed, though for some applications it may be useful to gain access to the circuit without fully removing the packaging. This can be done with a variety of methods depending on the packing material including acid baths, thermal treatments, and mechanical solutions. [39] Once the chip itself has been isolated, the delayering of the chip to the transistor level can be accomplished in several ways as mentioned in the introduction.

1.10 Photonic Waveguides

Waveguides are the basic element of integrated photonic systems, serving the purpose of confining and directing light. There are several varieties of waveguide, as seen below. The waveguides used for the work presented in this thesis are primarily silicon nitride strip waveguides.

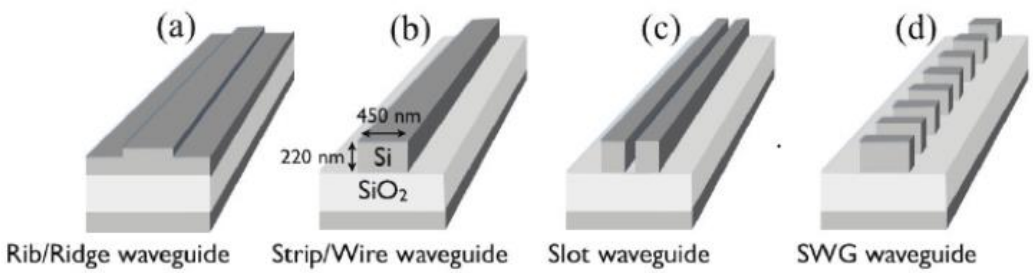

Figure 20: Waveguide geometries [40]

Light propagating through a waveguide does so in distinct optical modes. For this purpose, an optical mode is a spatial distribution of optical energy within a waveguide that is constant with respect to time. A mode can be described mathematically as a solution to Maxwell's equations that satisfies the continuity

conditions at the boundary, the allowed modes in a waveguide being defined by the indices of refraction of the constituent parts and the physical dimensions of the guide.

1.10.1 Optical Loss in Waveguides

Optical loss in waveguides is generally a result of scattering, absorption, or radiation, and can also be largely separated into coupling loss and propagation loss. Coupling loss being the loss resulting from coupling light into and out of the waveguide, and propagation loss being the loss occurring during propagation of the allowed mode(s).

Propagation loss is most easily measured using cut-back methods. In order to conduct a cutback measurement, waveguides of identical properties with the exception of length are characterized. This can be done using many waveguides of differing lengths, or by using waveguides of some relatively large initial length and then actively reducing that length for each round of characterization. [41] Having obtained loss measurements of the waveguides, the results can then be plotted in a 'loss vs. length' format. A linear fit can then be applied to this plot, the slope of which will provide a measurement of the propagation loss. The coupling loss can then also be extracted in the form of the y-intercept of the fit. This process will be covered in more detail in Chapter 2.

Chapter 2: FIB Optical Facets

2.1 Introduction

The following chapter is an expansion of an as-yet unpublished paper entitled "Efficient Waveguide Facet Preparation Using Programmable Focused Ion Beam Sculpting". Authorship is provided below.

Connor D. Wong,[1] Henry C. Frankis,[1] Khadijeh Miarabbas Kiani,[1] Richard Mateman,[2] Arne Leinse,[2] Jonathan D. B. Bradley,[1] Andrew P. Knights,[1] Nabil Bassim[3]

[1]*Department of Engineering Physics and Centre for Emerging Device Technologies (CEDT), McMaster University, Hamilton*

[2]*Lionix International BV, Enschede AL 7500, The Netherlands*

[3]*Department of Materials Science and Engineering, McMaster University, Hamilton*

All figures within this chapter are labelled as 'Fig' and are numbered separately from the thesis as a whole.

2.2 Background

Photonic systems offer high speeds, long distance communication, and multiplexing of multiple data channels into single fibers. Taking advantage of existing CMOS processing technology, integrated silicon photonics promises the miniaturization of optical processes, a technology of great interest to both industry

and academia as the benefit of mirroring the scalable, high-volume, low-cost production of silicon-based microelectronics is clear. [42]

Integrated photonic devices require coupling light of external source light onto the chip. As such, optical facet production is of significant concern to the industry. While several facet preparation methods do exist, including cleaving, dicing, and deep trench etching, each has its drawbacks. The most traditional method for achieving high quality optical facets is chip cleaving. This process requires a chip "scoring "step, often with thinned substrates. Dicing, performed using a saw with a thin diamond blade, is more efficient but does not necessarily produce low loss facets due to chatter and uneven mechanical properties in the chip, although it may be possible to achieve low loss with optimized dicing parameters. [12] Diced facets are generally improved post-dicing by lapping and polishing, which does produce reliably high-quality facets but requires additional effort in the form of stacking and bonding the devices for polishing. [12] Deep trench reactive ion etching (RIE), where facets are prepared by plasma etching several hundred microns through the buried oxide layer and substrate, is able to produce relatively repeatable and smooth facets in wafer scale but requires an additional lithography step. These traditional preparation methods using cleaving or dicing, and the newer methods using deep-etching, are being challenged by, for example, the emerging requirement for the integration of chips with different functionality onto the same sub-carrier, or with the need to bond an active device, such as a laser diode, directly to a chip performing other functions such as modulation. This integration restricts the utilization of cleaving due to process flow and the need to keep chips intact or renders deep-etching challenging due to the different chemical compositions of the various chips, and the topology associated with integration.

With the increase in photonic integration through the combination of different chips, new processes are under investigation. In this paper, we report preliminary

studies of an automated method for the production or modification of optical facets using a focused ion beam (FIB). Though the use of FIB in the production of high quality optical facets is not in itself novel, [14] [13] we have addressed the long-standing criticism that FIB is not manufacturable.

Combining capacity for microscopy and fabrication, FIB technology has found use in a wide variety of applications including serial-sectioning tomography, sample preparation, failure analysis, and more. [2] Its appeal in this case stems from its overall flexibility, capacity to produce good optical facets, and the ease with which it lends itself to process customization and, in contemporary instruments, automation. The potential for the use of FIB in photonic processing may well extend beyond the fabrication of optical facets. We note that optical gratings, photonic crystals, nano-antennas, and other photonic devices produced with FIB have been reported in a variety of materials. [14] [15] [43] In micro-electronics, FIB is often used for metal connection repair and lithography mask modification. The utility of FIB is thus undisputed, but the criticism of its use is often related to its relatively slow, serial approach, often requiring significant operator attention. Programmable fabrication addresses these concerns, while the smaller volume of chip production in photonics together with the added value of hybrid integration suggest the photonics industry may benefit significantly from the wide deployment of FIB processing.

A standard dual-beam FIB instrument consists of paired electron and ion columns, set between 52 and 54 degrees to each other. This allows the instrument to act as an SEM when additional imaging functionality is required, and it can be further augmented with characterization tools for Energy Dispersive X-ray Spectroscopy (EDS), Electron Backscatter Diffraction (EBSD) among others. FIB can be used to sputter in a scanning, line-of-sight process to perform a mode of direct-write, resistless and maskless lithography. Gas injection systems can be used in

conjunction with the beam to deposit material in a directed manner, or similarly produce gas assisted etch processes. [33]

The ion beam itself can be produced with several different source configurations, each of which has a range of associated potential ion source materials. The classic ion source is a gallium liquid metal ion source (LMIS), which consists of a needle that is wetted with liquid gallium and an electrode which extracts an axial spray of ions from the gallium, producing an effective point source. Gallium's relatively high mass makes it an effective sputtering tool and its low melting point and vapor pressure contribute to its attractiveness as an ion source. [20]

Gallium has its drawbacks however, including a tendency to cause lattice damage [44], Ga+ ions implant in devices that may interact chemically with the sample. [1] LMIS is also constrained in that above 20 nA, spot size becomes limited by spherical aberration, with the current density decreasing rapidly. [17]

In order to avoid these undesirable side effects of gallium, the FIB used for this work was a ThermoFisher Scientific Helios G4 UXe PFIB which uses an inductively coupled plasma (ICP) of xenon gas as an ion source. Xenon is favorable for its high sputtering rate, chemical inertness, and potentially, reduced lattice damage [17], and the ICP source itself offers a lifetime on the order of years (as compared to the ~1500 hour lifespan of a LMIS) and allows for the use of significantly higher beam currents. Collision cascades are a result of energy transferred from an incident ion displacing an atom in the target, which may then displace an additional atom and so on until the energy is expended. At the end of this process, most of the ions will have been implanted in the sample. This is

problematic for several reasons, firstly because the sample surface will be amorphized up to the depth of the cascade, and secondly because implanted ions (more particularly gallium) can have detrimental effects on the optical properties of the material. [44] SRIM (Stopping and Range of Ions in Matter) simulations of collision cascades for gallium and xenon in silicon nitride (the material under study here) give average penetration ranges of 10.4 nm and 7.2 nanometers respectively at an incidence of 85 degrees.

Another concern of note is process speed. For a FIB process to be practical, it needs to be competitive on at least some level with preexisting facet preparation methods. The reduction in milling time is of great importance to any such method, something for which the PFIB is ideally suited.

The primary goals of this work are to produce optical facets with FIB, characterize them, and optimize the process (in terms of speed and quality) for automation. To do this, several factors must be considered. As mentioned, speed is of great interest, and higher speed necessitates the use of higher current to take advantage of the correspondingly higher milling rate. This comes with the tradeoff of lower resolution, which, as will be clear from the results, can be expected as a limiting factor in terms of both the magnitude and the distribution of deleterious ion beam damage.

The samples used were silicon nitride photonic chips produced with a standard wafer-scale foundry process [45]. A 0.2 μm thick Si_3N_4 film (selected as a standard silicon nitride thickness to compromise between strong lateral confinement and minimizing stress difference with the substrate) was deposited by low pressure chemical vapor deposition onto a 100 mm diameter silicon wafer with an 8 μm thick wet thermal SiO_2 layer. Waveguides with widths varying from 0.5 to 2 μm and

lengths varying from 1 to 10 cm were defined by stepper lithography and reactive ion etching through the silicon nitride layer. The early fabricated devices were initially diced into chips, with the dicing lanes adjacent to the waveguide edge. While this allows coupling to the waveguides, the facets produced exhibit significant variation in quality. For this reason, on the later devices (which are used here) the chip facets were defined in a second exposure step to outline a deep trench etching pattern. The exposed 8 µm buried oxide and silicon substrate were etched 300 µm down by a plasma etching process. Chips were then individually separated by a dicing process. These facets will henceforth be referred to as 'etched' facets. As the basic photonic component, straight waveguides were selected for their availability and relative simplicity. The device structure is schematically described in Fig 1. After facet preparation, a 1 µm thick film of fluoropolymer (Cytop) was spun onto the devices to fulfill refractive index requirements for light confinement.

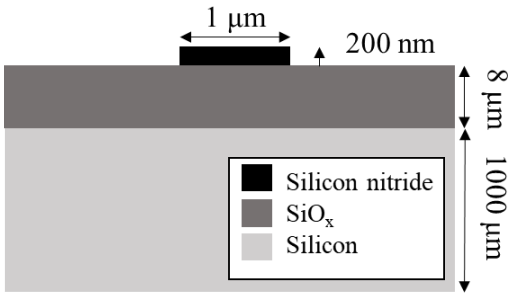

Fig 1. Silicon nitride waveguide schematic (not to scale)

Simulations of the fundamental TE mode profiles at 1550 nm for the silicon nitride waveguides of widths 1 µm and 1.2 µm are shown in Fig 2. The mode sizes are 1.45 μm^2 and 1.26 μm^2 respectively.

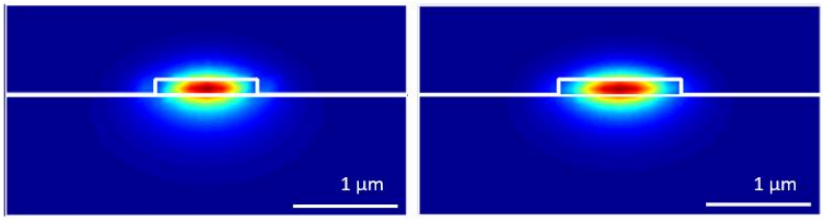

Fig 2. RSoft simulations of mode profile for silicon nitride strip guides of 1 and 1.2 micron widths.

The primary requirement of facet fabrication is to create a smooth undamaged surface of sufficient size to accommodate the optical mode.

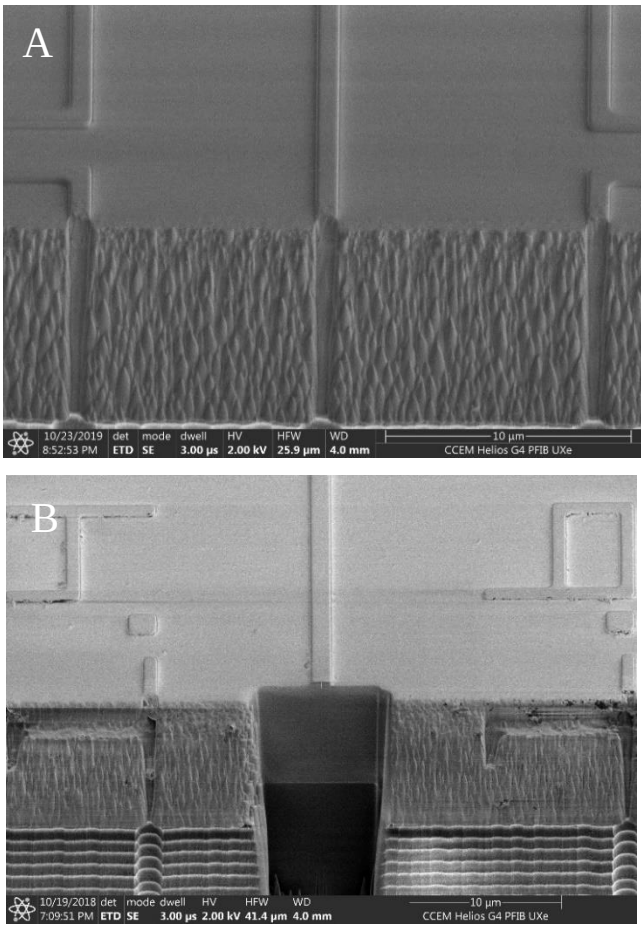

Fig 3. A) Etched silicon nitride facet, B) PFIB modified silicon nitride facet (15 nA current)

Optical loss of light coupled into a photonic waveguides can be described by (1) coupling loss, which arises from mode mismatch between the waveguide and the fiber, and from facet surface scattering, and (2) propagation loss, which arises from some combination of scattering, absorption, and radiative loss as it propagates along the length of the waveguide. In the present case the propagation loss is dominated by the scattering term.

For the initial testing, fiber coupling characterization was used to obtain measurements of total loss in order to verify measurable reduction in loss over the etched facets, and to investigate the necessity of additional time consuming low-current FIB polishing cuts. Using an Agilent 8164A as a source and detector for 1550 nm light (selected as a standard telecom wavelength), the waveguides were mounted between two 2.5 μm tapered fibers on xyz alignment stages which were then positioned to maximize the observed output power. Polarization paddles were used to control the input. Fig 4 shows the total loss across 1 cm long waveguide samples with etched facets, FIB cut facets at 1 nA, and FIB cut facets at 1 nA with an additional FIB polish at 0.1 nA. The results suggest that FIB cut facets lead to significant improvements in facet quality, but additional low current polishing steps offer minimal improvement, though they may improve the quality control throughout a batch.

2.3 Experiments and Results

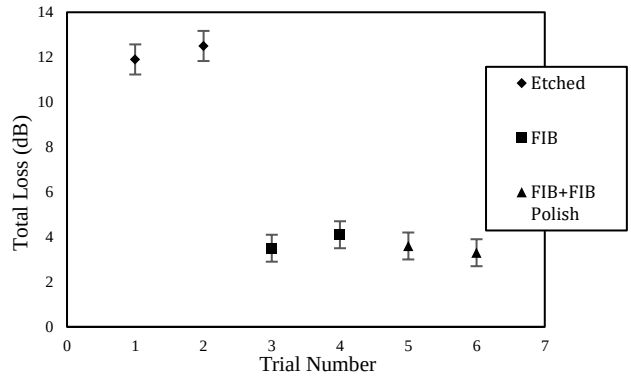

Fig 4. Initial test results comparing etched, FIB at 1 nA, and FIB with an additional 0.1 nA FIB polish cut step on 1 cm guides

The second set of tests used currents of 1, 4, and 15 nA. Milling time for each current, as well as for currents used in later tests are shown below in **Table 1**. While the difference in time is not directly proportional to difference in current, there is still the difference between a 30 second process and a 2 minute 30 second process.

Table 1: Milling Current vs. Time

Current (nA)	**1**	**4**	**15**	**60**	**200**	**500**	**1000**
Time (s)	150	47	30	7	4	2	1

In order to isolate the improvement to coupling loss, a cut-back method was used to determine both coupling and propagation loss, [41] the results of which can be seen in Fig 5. To do this, the same characterization setup as before was employed

on otherwise identical waveguides of several different lengths. From this, the results can be plotted as optical loss in dB vs. length in cm, and a linear model can be applied of the form

$$L = L_p * l + L_c$$

where L is total loss in dB, L_p is propagation loss in dB/cm, and L_c is coupling loss in dB. This study used waveguides of 1, 2.45, 3.93, and 5 cm lengths. Cutback measurements were carried out first on etched waveguides, and then for waveguides with facets modified with each of five beam currents (15, 60, 200, 500, 1000 nA). These were selected to be representative of the range of practical currents available on the instrument (in conjunction with earlier results) and for their availability. The cutback measurement results from the waveguides with etched facets were used to determine the etched guide coupling loss (as per **Table 2**), giving a value of 5.2 ± 0.5 dB per facet. This can be contrasted with the 60 nA FIB cut facet loss of 2.2 ± 0.7 dB/facet. The loss vs. length slopes from the cutback measurements were found to be 2.4 ± 0.3 dB/cm etched, 1.8 ± 0.5 dB/cm at 60 nA, 2.4 ± 0.1 dB/cm at 200 nA, and 1.7 ± 0.2 dB/cm at 1000 nA. The values taken from the 500 nA facets were discarded due to clear lack of consistency

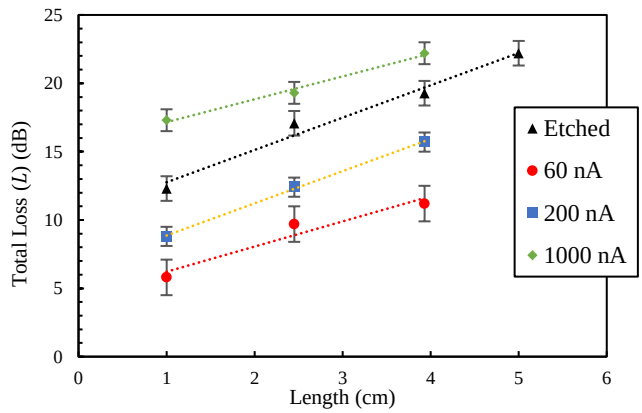

Fig 5. Cutback measurement results

Table 2: Loss vs. Length Curve Constants

Preparation Method	Etch	60 nA	200 nA	1000 nA
L_p (dB/cm)	2.4±0.3	1.8±0.5	2.4±0.1	1.7±0.2
L_c (dB)	10.4±0.9	4.4±1.3	6.5±0.2	15.5±0.5

In Fig 6, images of the facets produced with each of the five selected currents are shown.

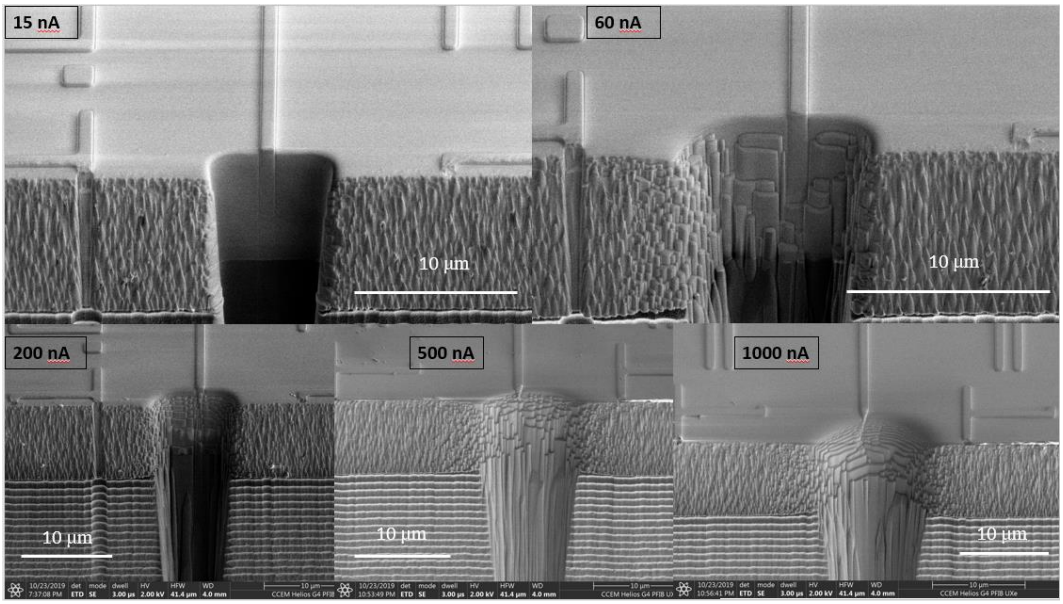

Fig 6. Visual comparison of facets produced with varied FIB currents

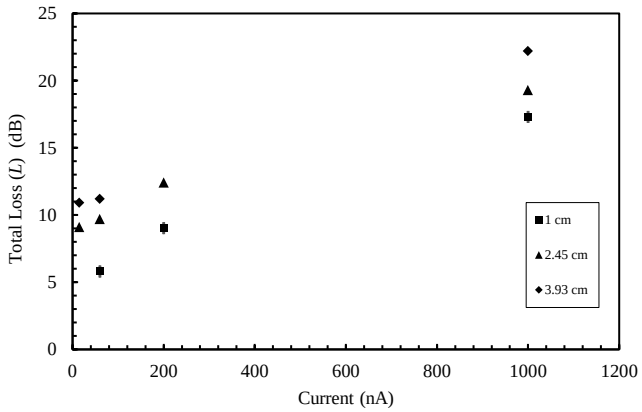

Fig 7. Total loss vs. current measurements for guides of 3 lengths

Fig 7 shows the measurements taken of total loss (L) in dB vs. the milling beam current employed in nA. Different markers correspond to different waveguide

lengths. The loss measurements follow as one might expect from a basic visual inspection of Fig 6, with lower loss in the 15 and 60 nA trials, and increasingly higher loss throughout, especially as seen on the 500 and 1000 nA facets where the guide ends are clearly ablated and deformed. This ablation is partially due to the unusually high currents employed, as the coulombic repulsion of the ions that compose the beam inevitably result in larger beam spot size and thus lower milling resolution It should also be clear from Fig 6 that the immediate surroundings are deformed as well, which likely affects the outer edges of the mode profile. It is clear that total loss increases with higher milling beam current (and with length), but further work is required to determine the exact relationship. It should be noted that the total coupling loss of the etched facets is 10.4 ± 0.9 dB/facet and the total coupling loss from the best FIB modified facets measured here is 4.4 ± 1.3 dB/facet, and that these results relate to the deleterious effects of increasing beam current. As these results were also compared to earlier tests when selecting for speed, the 15 nA current was selected for automation as a good compromise between facet quality and milling time.

Using a combination of ThermoFisher's iFast process development software that accompanies the FIB instrument and direct editing of the underlying Python script, an automation routine for facet modification was built in order to accelerate production. While some limitations still apply (the user must still align and focus the microscope on the first guide manually), it still serves as a useful proof of concept. The process also assumes that the guides are evenly separated on the chip, but this issue could be eliminated by introducing a continuous searching loop.

Once the appropriate focus has been achieved, and the number and separation of the waveguides supplied, the routine may be implemented and will proceed as per the flow chart in Fig 8. Due to variety in guide width (0.5 to 2.0 μm) several conditional statements were used to match the image with training images taken from guides of 0.5, 1.0, and 2.0 μm widths using the inbuilt 'Patmax high

sensitivity' algorithm with tolerances set to 0.5, 0.5, and 0.25 for the respective guide widths. The search region was restricted to a 10 x 10 µm square to reduce the likelihood of false positives.

As can be noted from the slightly smaller notch in the chip edge on the third waveguide from the left in Fig 9, the routine can handle some small variety in the distance from the chip edge to the guide end. Using a 15 nA beam (at 30 seconds per facet) and accounting for built-in process delays, the automation routine takes approximately 1 minute per facet. As minimal oversight is required, this allows the production of significant numbers of facets at reasonable speed. A video of the automated process is available in the supplemental information.

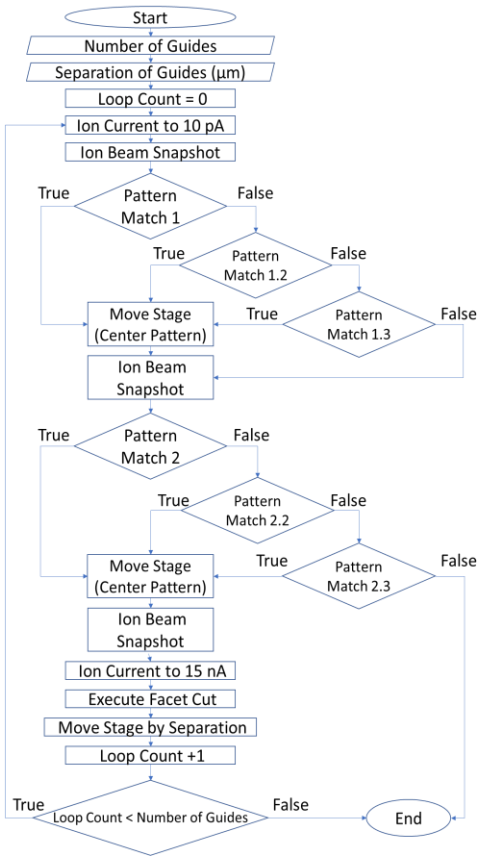

Fig 8. Automation process flow chart

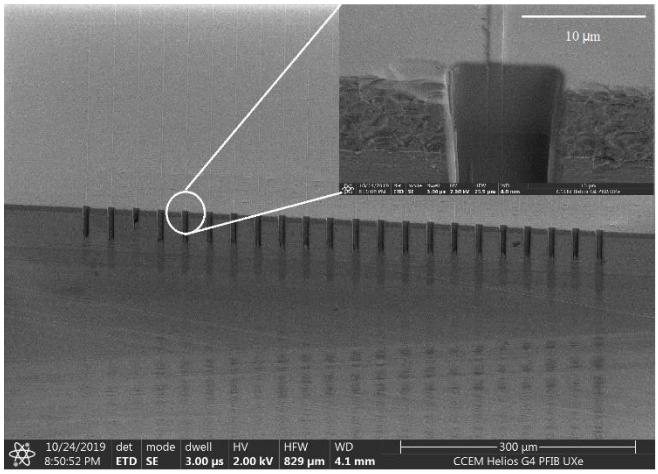

Fig 9. FIB facets produced with iFast automation routine at 15 nA

A second set of silicon nitride waveguides with the addition of a 320 nm thick TeO_2 coating and the same etched facets was used to test the 15 nA automated routine. No Cytop was applied.

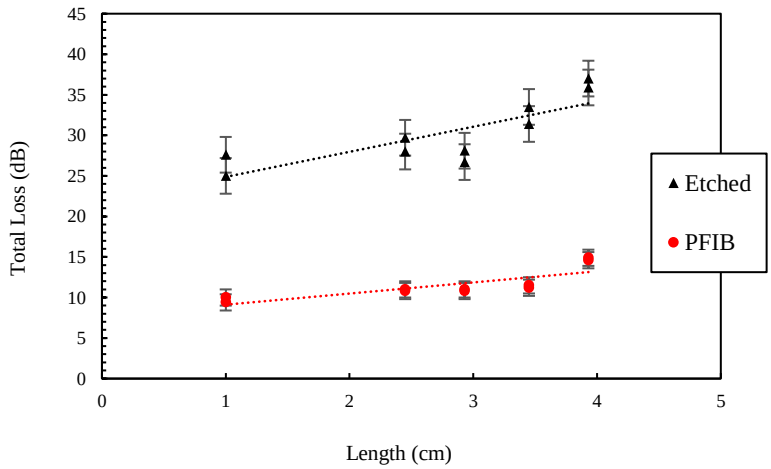

Fig 10. Cutback measurements with 15 nA automated routine in tellurium oxide coated silicon nitride

Table 3: Loss vs. Length Constants (Automation Routine)

Preparation Method	**Etched**	**15 nA Auto**
L_p (dB/cm)	3.1±0.9	1.4±0.4
L_c (dB)	22±2	7.7±1

The results of cutback measurements conducted using the automation routine at 15 nA (seen above in Fig 9 and Fig 10) represent losses per facet of 11 ± 1 and 3.9±0.5 dB for the etched and PFIB edited facets respectively. An overall improvement of 7.1 ± 1.1 dB can thus be seen for the PFIB edited facets.

2.4 Conclusions (FIB Facets)

While this paper presents results from testing done on very straightforward devices, it should be apparent that the methods described are applicable to other scenarios. There are drawbacks to this approach, namely that if a single chip had 100 waveguides on it, it would take 1 hour and 20 minutes (at 15 nA) to complete meaning that wafer scale processing would be prohibitively long with these parameters. However, the nature of FIB facet modification is such that it can be tailored to individual devices if desirable and could potentially be used in cases where cleaving is not practical, such as on stacked devices. As it can also improve diced or etched facets when necessary, including a useful tolerance for snapped guides, it can be used effectively in a research and prototyping context. With the demonstrated capacity for automation, average improvement of ~3 dB/facet over the etched facets used, and overall flexibility, FIB facet modification has the potential to be a powerful tool for a variety of situations in the field of silicon photonics.

Chapter 3: Nanoscale Heat Transfer

3.1 Introduction

The premise of this project was developed by Dr. Maureen J. Lagos (who published related work in his 2017 paper entitled "Thermometry with Subnanometer Resolution in the Electron Microscope Using the Principle of Detailed Balancing") [46] in the interest of continuing his work on investigating nanoscale heat transfer, in particular to determine the available polariton channels for radiative heat transfer between nanogaps. The goal was to produce structures with nanogaps (a nanoscale separation between two crystal regions) below 50 nm and a measurable temperature gradient across those gaps. Heating should enable probing of the modes involved in radiative heat transfer using electron beams for temperature measurement. As the modal contributions from various individual and hybridized modes are unknown, this could provide information significant to a variety of metamaterial applications. Unfortunately, at time of writing the situation resulting from COVID-19 has prevented the completion of characterization work on most of the test structures. It is likely that further results will be available when access to the requisite facilities is once again possible.

3.1.1 Objectives

The objectives of this work are as follows:

1. The fabrication of nanogaps (<50 nm)
2. Fabrication of structures exhibiting thermal gradients across the gaps (complex bridges, serpentines, heat lenses)

3.2 Experimental

3.2.1 Nanogaps: Basic Bridges

The starting point for this work was the production of nanogaps in the form of simple bridge structures, as seen below in Figure 21.

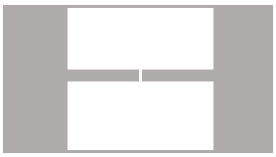

Figure 21: Initial bridge structure concept

The samples were suspended silicon carbide films across which current could be passed to allow heating produced by Protochips [47]. A schematic can be seen below. It is also of note that the film thickness increases with distance from the central heating region.

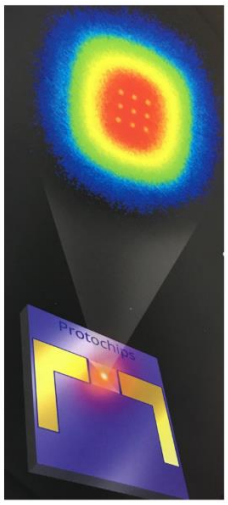

Figure 22: Protochip device schematic. Note the close-up view of the heating region.

In order to create the desired temperature gradient, we began by placing one end of the bridge depicted in Figure 21 within the hotter red region in Figure 22 and

placing the other end in the cooler (yellow and blue) regions. The structure was produced by making two rectangular cuts to define the bridge, both 4 x 10 μm leaving a relatively wide (~4 μm) bridge in between. The bridge was then thinned in several steps, beginning with larger (2 x 10 μm) cleaning cross section cuts oriented away from the bridge, and ending with smaller (0.5 x 10 μm) cleaning cross section cuts. This process can be seen in below in Figure 23. The primary purpose of the simple bridge structures was the creation of nanogaps smaller than 50 nm.

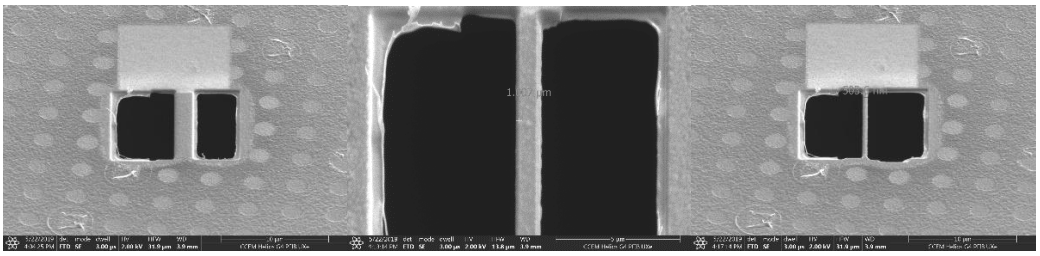

Figure 23: Bridge 1 thinning process. Final width 500 nm.

Bridge 1 also demonstrates an addition to the basic scheme in which a section of the surface abutting the “cool” end of the bridge has been partially amorphized by the ion beam with the intent of reducing heat conduction. As these were very early trials and the film very thin, the amorphization parameters were selected by conducting a series of small area exposures (seen below in Figure 24).

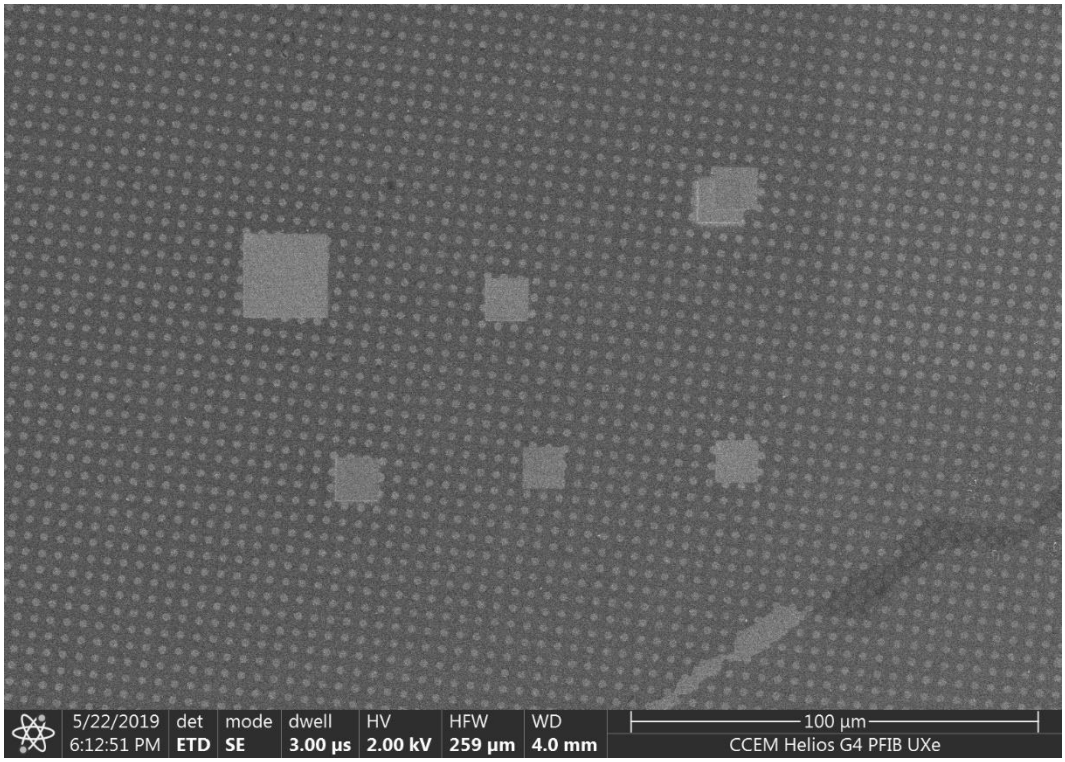

Figure 24: Amorphization trials 1-6

The aim was to achieve maximum amorphization with minimum sputtering as we were concerned that excessive structural change would affect the stability of the bridge structures. Knowing that the film was thinnest near the hot regions (~100 nm) and that the film grew progressively thicker with distance from the center, ~200 nm was selected as a desirable initial damage depth. Using damage depth findings determined by Sam Norris using 0.3 nA for 300 seconds on an area of 144 μm^2 to result in ~210 nm damage depth, exposure time was selected based on a target fluence of 3.9 x 10^9 ions/μm^2.

Using the selected amorphization parameters, an area of 10 x 10 µm was exposed, visible in Figure 23. The final step in the fabrication of the bridge was the creation of the gap.

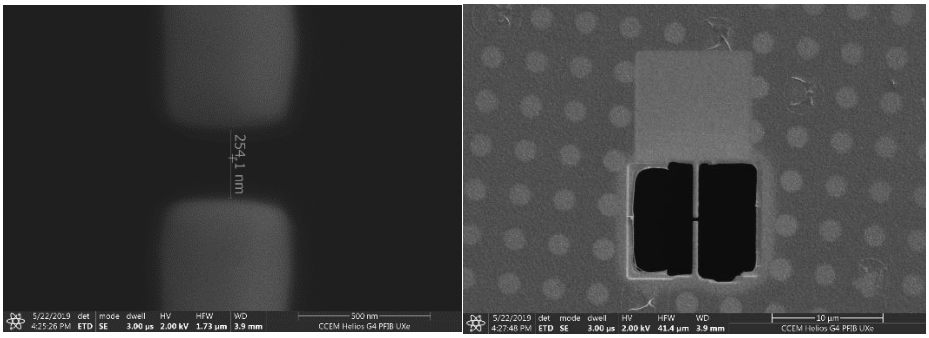

Figure 25: Bridge 1 gap (~250 nm wide), and completed structure

The gap was produced by making a line cut 1 µm long using the 3 pA beam and took 29 seconds. Due to the exploratory nature of the project, there was no specific requirement for the initial structure beyond making the gap as small as possible, but 250 nm was larger than desired and so the 1 pA beam was used for later trials.

Two additional bridge structures were produced for the first set of tests and can be seen below. Bridge 2 was an attempt at faster thinning by polishing to the final width immediately instead of in steps. This approach resulted in more redeposition on the bridge and was discarded.

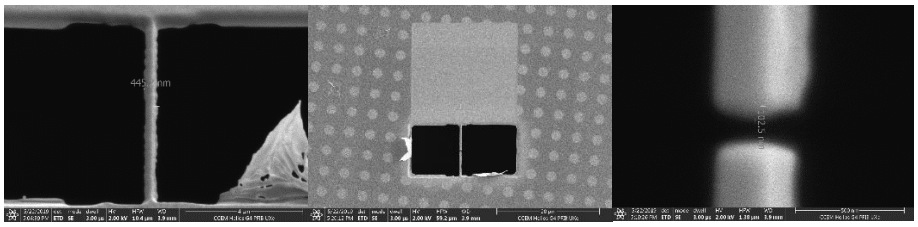

Figure 26: Bridge 2 showing redeposition on the bridge, amorphized region, and gap side of ~102 nm

The gap for Bridge 2 was cut using the 1 pA beam for a line cut 1 µm long and took 1 minute and 27 seconds. This produced a gap width of ~102 nm, which while still large was an improvement over the gap in Bridge 1. In order to further reduce the size of the gap, it was decided that the gaps on the next set of test structures should be produced in the gallium FIB for comparison, as the PFIB was limited by its probe

size at the currents used (~30 nm). The smallest gap successfully created with the PFIB was ~ 60 nm wide and can be seen below.

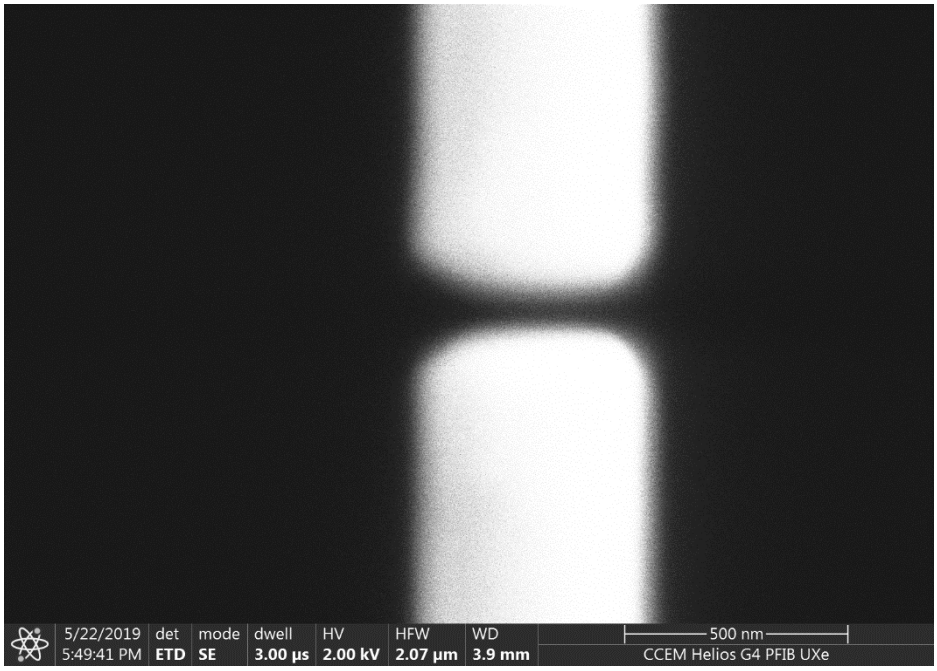

Figure 27: Smallest nanogap created with PFIB (~60 nm wide)

Using a new chip, a set of six test structures was produced. All of the amorphized zones were created first, covering areas of 20 x 20 µm at a dose of 5.5E-18 pC/µm^2. One of the bridges collapsed during an attempt at thinning beyond the previously achieved ~500 nm width in which a thinning cut was somewhat misaligned.

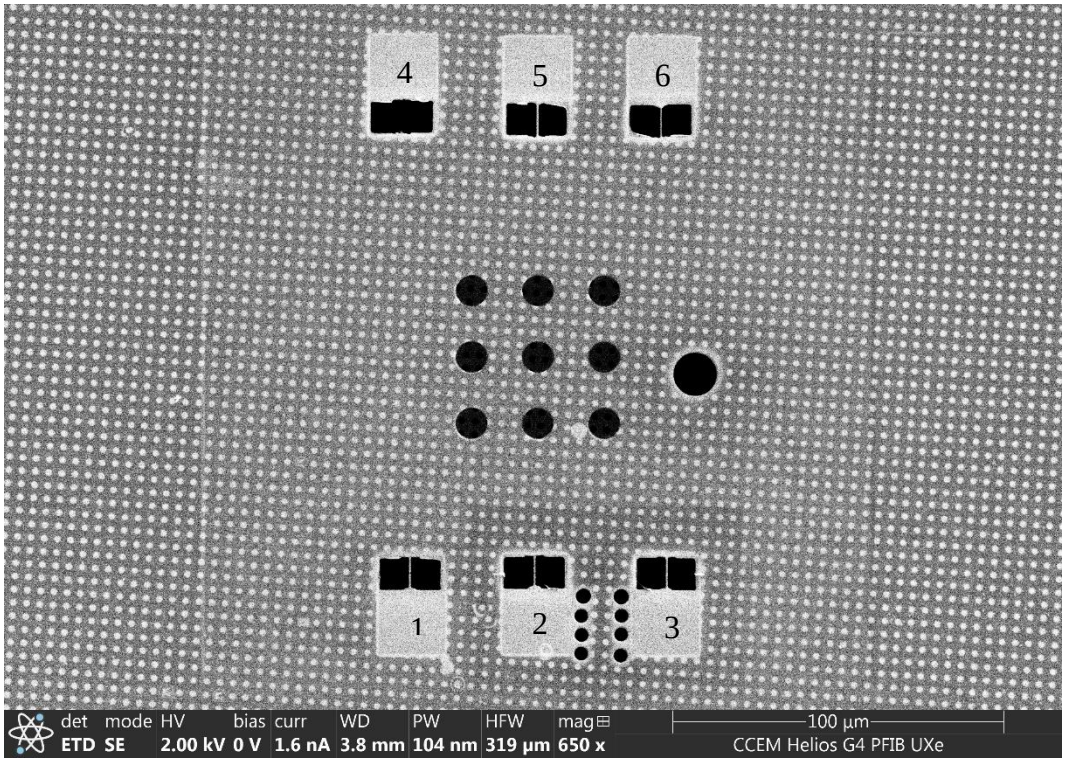

Figure 28: Six test structures produced to compare gap cutting methods. Site 1 cut with PFIB, Site 4 bridge collapsed during fabrication.

The gap for bridge 1 was cut using the PFIB to be used for comparison with the planned gallium FIB gaps. The application of the 1 pA line cut method resulted in an unclear result, appearing not to be severed completely as seen below.

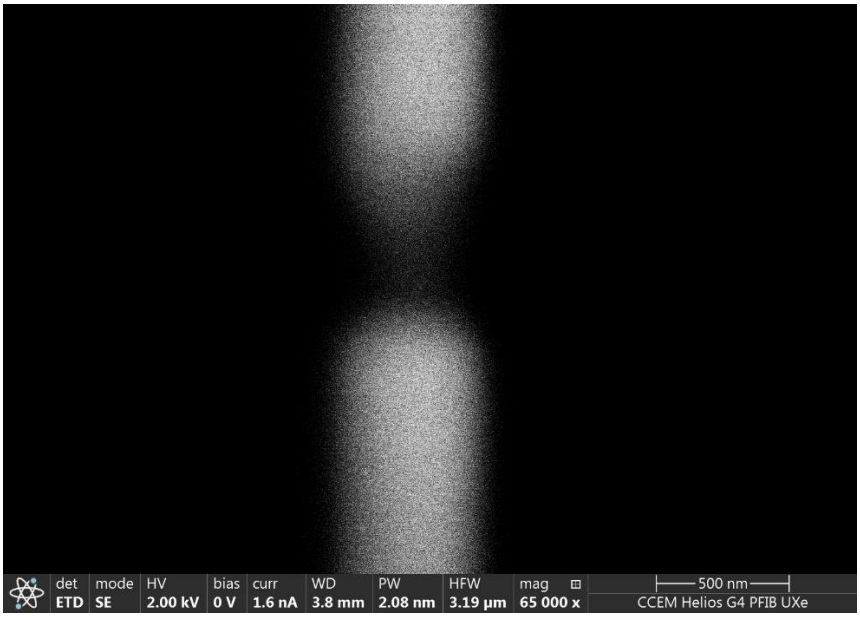

Figure 29: Site 1 gap image, top view. Note apparent connection.

This oddity was later found to be the result of a sagging effect on the amorphized end of the bridge when the structures were observed from the side during the gallium FIB bridge cuts. Hypothesizing that this sagging effect was a result of the amorphization reducing the structural integrity of the bridge, we proceeded to amorphize the surface on the other side of the bridge at site 6.

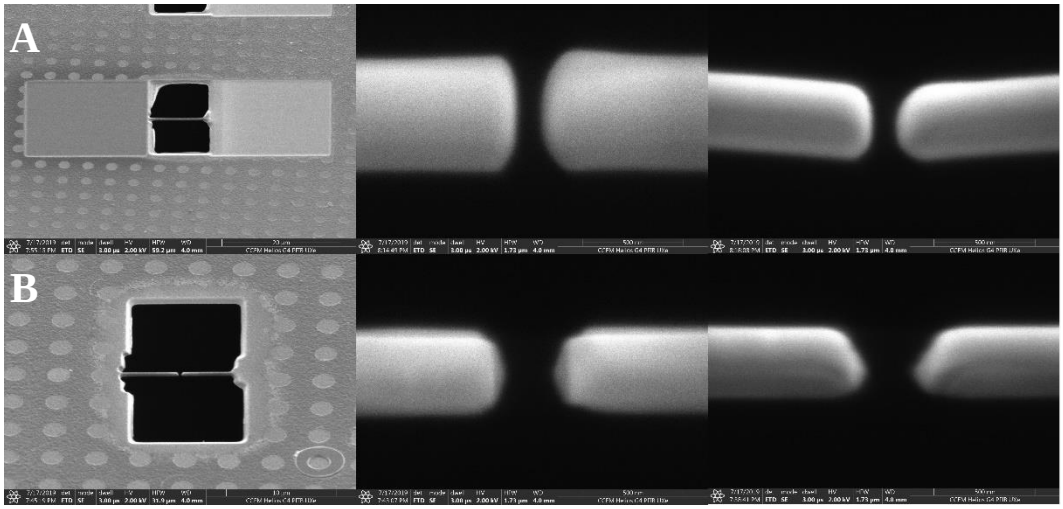

Figure 30: Row A: Site 6 after second amorphization, gap at 0 degrees (top view), and gap at 52 degrees; Row B: New bridge, gap at 0 degrees (top view), and gap at 52 degrees

Figure 30 shows the results of the second amorphization at site 6 (Row A), contrasted with an additional bridge structure, produced without any deliberately amorphized regions (Row B). The second amorphization region at site 6 used the same amorphization parameters as the first and the degree of sag on each side appears to be functionally equivalent. The non-amorphized bridge does not display any observable sag. During attempted characterization of the sagging bridges, Dr. Lagos found that the heating resulted in straightening of the bridges. While interesting, this would introduce additional variables and so it was decided that later structures would have to employ alternative strategies for reducing thermal conduction.

3.2.2 Thermal Gradients: Complex Bridges

Several designs were planned for heat reduction, including a longer, serpentine bridge, a longer straight bridge, and bridge with more complex heat barriers.

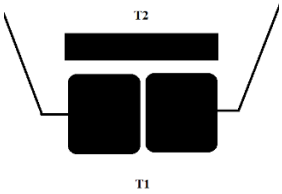

Figure 31: Bridge with barrier holes to reduce heat conduction. T1>T2.

The first of the new strategies to be attempted was the bridge with barrier holes, seen in Figure 31. The low temperature side (T2) was placed in the 'cool' region on the chip with the intention that the physical gaps would further reduce conduction to the cool side of the bridge. The first run of barrier hole structures failed when the thin cuts to either side resulted in the cracking of the membrane.

The design was then modified so that the thin cuts were parallel to the structure instead of at a 45 degree angle. Later versions also incorporated a small circular hole at the end of each line cut to make the potential crack radius less acute.

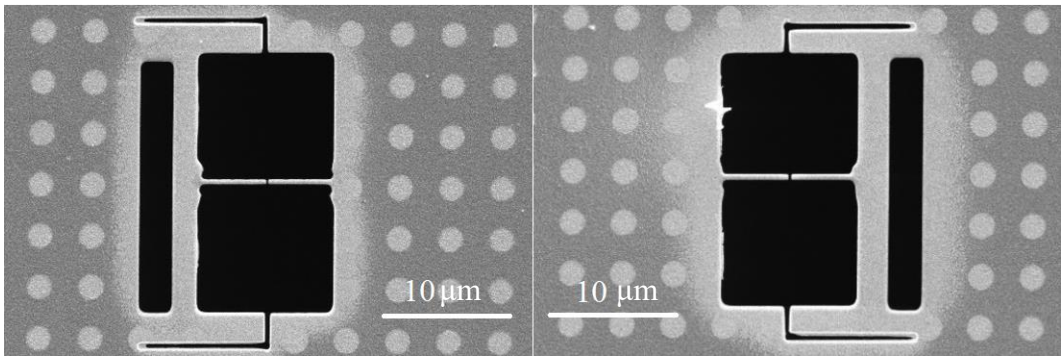

Figure 32: Two modified barrier hole structures

Figure 32 shows the two modified structures produced after the collapse of chip 1. Another modification made to the process at this point was that instead of using set milling times for the gaps, the structure would be rotated so that the gap could be viewed from the side, and the electron beam would be employed to view the milling

in real time, allowing the cut to be halted once the bridge was fully severed. The results of this method can be seen below in Figure 33.

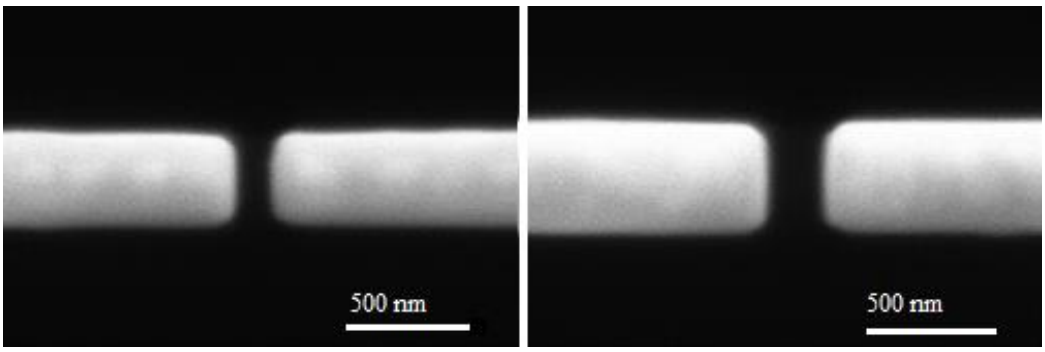

Figure 33: Gaps on modified bridge structures

Another method that was applied during the gap fabrication process was the use of the 'spot burn' function on the PFIB for minor edits to the gap. If there was any drift during the original milling process, or if the mill was misaimed, then the bridge gap would be asymmetrical. This was fixed by placing the spot burn on whichever side of the gap was smaller and then milling with the same real time SEM observation process. The spot burn could be placed anywhere within the gap but was also often placed just outside of the gap to either side as this produced a smaller and very manageable effect on the gap geometry.

An additional design modification, that of holes milled into the structure in regions of interest, was added as thinner probing regions were required for characterization. Using the spot burn function again at 1 pA, we tested a series of milling times. Due to the scale involved, it was difficult to garner exact understanding of the depth of each hole. This was further exacerbated by the varying thickness of the film, and the additional reduction in thickness in parts of the bridge structures.

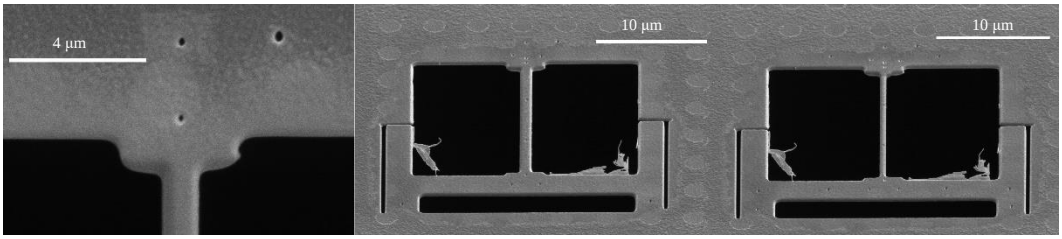

Figure 34: Characterization holes, close up, mid process, and end results

3.2.3 Serpentine Structure

After producing several of the modified barrier hole structures, we attempted to produce a long winding bridge (the results of which can be seen in Figure 35), as similar structures have been demonstrated to exhibit thermal gradients. [48] The initial plan was to sever the remaining thin connection on the far right of the bridge to form the gap, but as the structure was fabricated it became clear that the structure would likely collapse if this were the case.

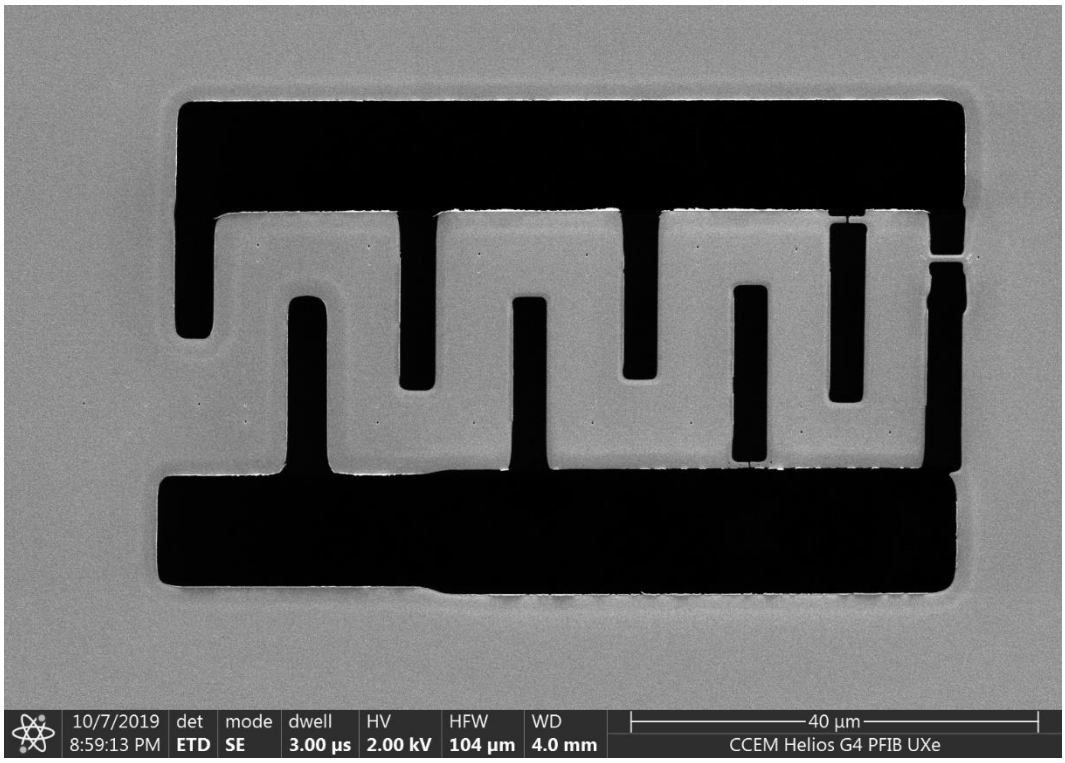

Figure 35: Serpentine bridge structure

Each time one of the connective struts was severed, the structure would twist significantly. This is visible below in Figure 36.

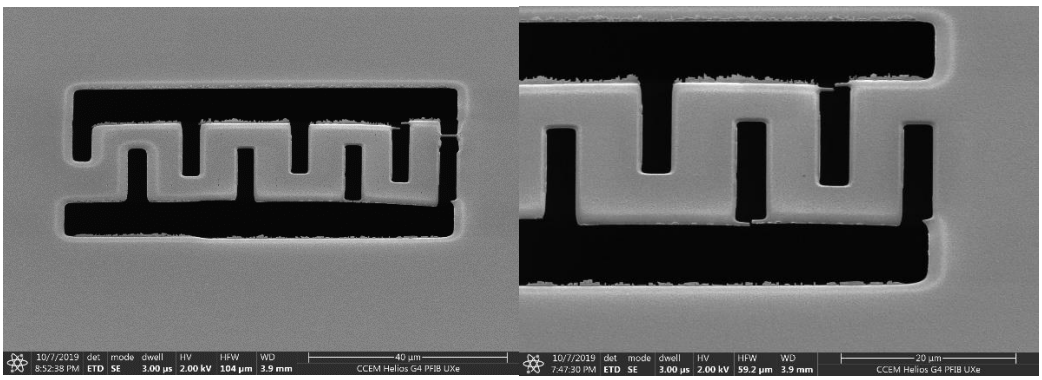

Figure 36: Twisting of structure after cutting of support struts.

At the end of the process, it was decided that the support struts themselves could be used, and characterization holes were milled across the entirety of the structure in order to collect measurements of how well the serpentine structure functioned for radiating heat over its length.

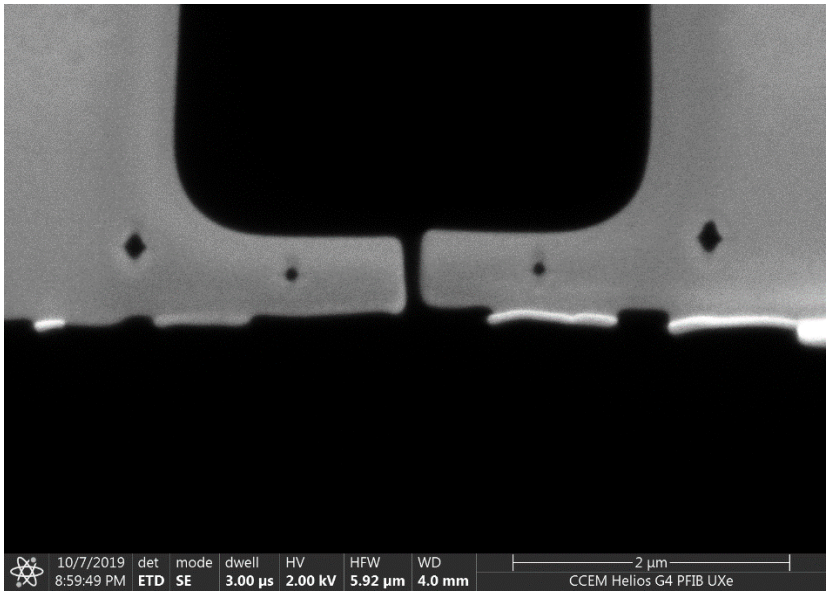

Figure 37: Serpentine structure nanogap, bird's eye view

Above is a close up view of one of the nanogaps on the serpentine structure. While promising from a bird's eye view, the gap is in fact separated in height due to the twisting of the structure.

At this point we returned to some earlier structures that had already undergone some attempted characterization and milled new characterization holes into them. Many of the earliest structures lacked holes entirely, and the holes milled during the fabrication of several of the later ones were found to be insufficient.

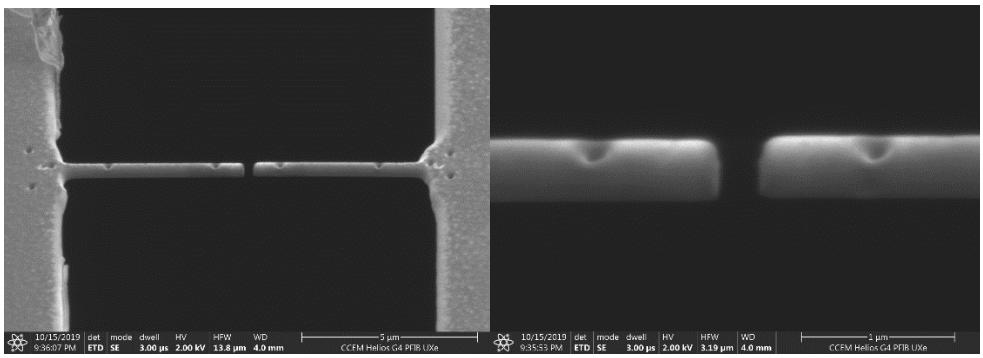

Figure 38: Improved characterization holes

3.2.4 Heat Lens

In order to augment any potential success in blocking heat conduction with the earlier designs, Dr. Lagos proposed that some method of heat concentration should be applied to the hot end of the bridge. Using a design concept previously reported in literature, [49] a heat concentration lens was added to the existing barrier hole structure.

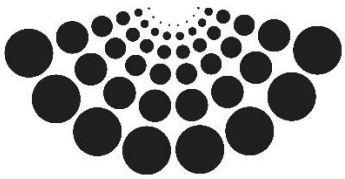

Figure 39: Heat lens bitmap

Using a bitmap, the pattern was milled using a current of 0.1 nA with a 1 µs dwell time. The initial dimensions were 30 x 17 x 1.2 µm, after 0.8 µm depth was found to be insufficient to cut the smallest holes. This produced a complete structure; however, the lattice was very thin and unlikely to be capable of significant heat conduction. This result can be seen below in Figure 40.

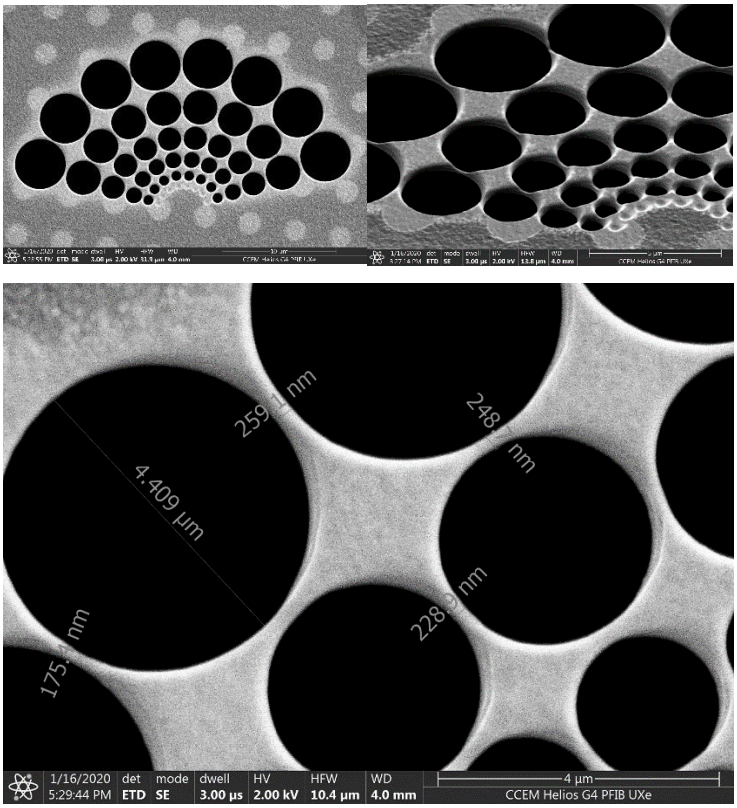

Figure 40: First heat lens trial. Note that the connective structure is very thin.

Despite the apparent fragility of the structure it was deemed to be of potential use and so the remaining components of the bridge were fabricated as well.

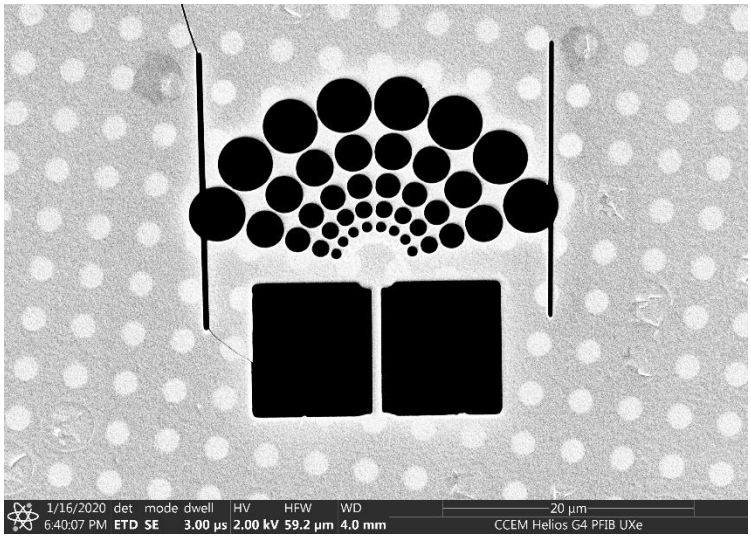

Figure 41: First completed heat lens structure. Note the beginnings of cracks in the membrane.

Cracking in the membrane necessitated the use of circular end holes for all future thin cuts.

A 0.9 scaled version of the heat lens pattern was produced to ensure thicker conduction pathways. A 0.8 scaled version was also produced but was not used beyond a small test as the 0.9 scaled pattern appeared functional. Milling depth was reduced to 0.9 µm in order to avoid over-milling and excessive amorphization of the connective lattice. This required the two smallest rows of holes to be milled individually. The second smallest row was milled using the 0.1 nA beam at a depth of 0.9 µm, and the smallest using the 10 pA beam at the same depth.

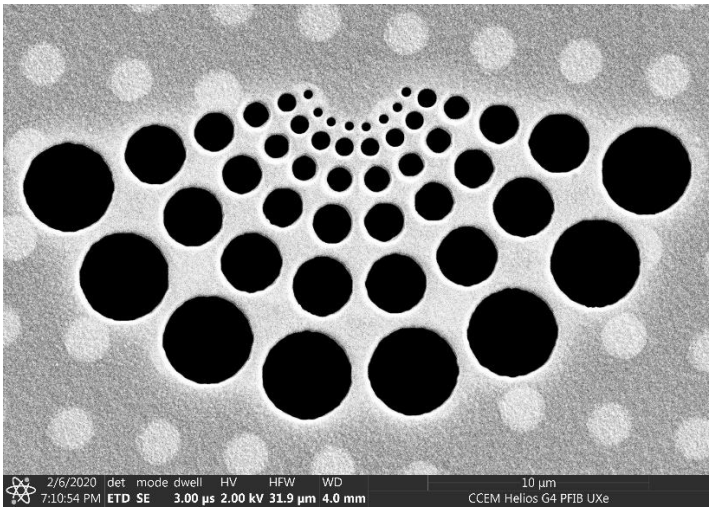

Figure 42: 0.9 scaled heat lens

The process was completed with the standard rectangular cuts, linear cuts, and characterization holes.

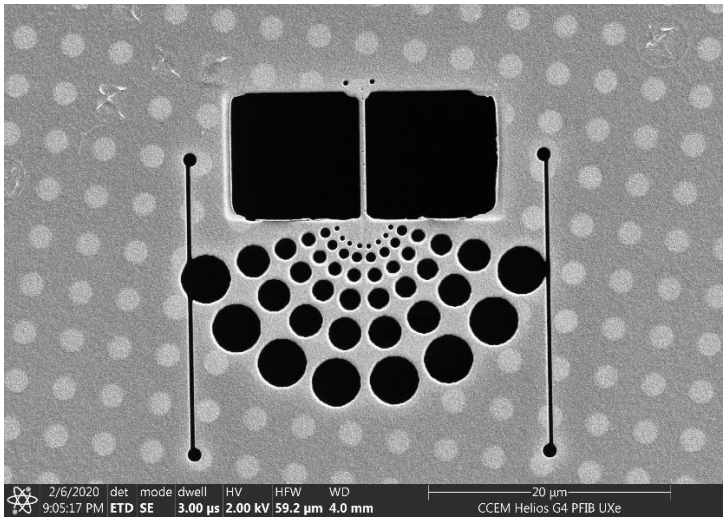

Figure 43: 0.9 scaled heat lens structure

The completed structure does display some sag on the heat lens side of the bridge, as seen below in Figure 44.

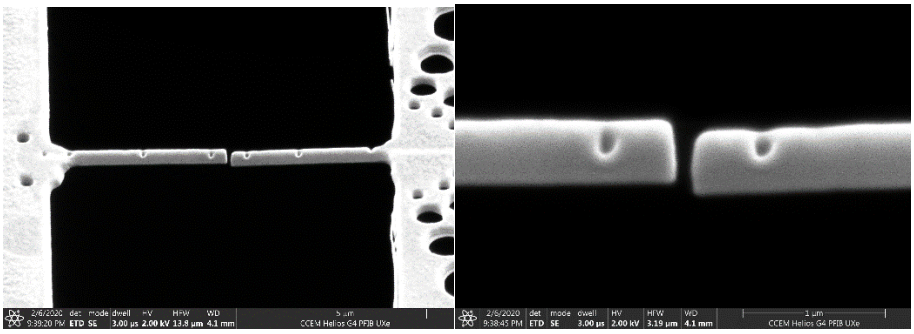

Figure 44: 0.9 scaled heat lens structure bridge gap

3.3 Conclusions

In the execution of this project, nanogap test structures of several different configurations were fabricated, including simple bridges, bridges with amorphized heat barriers, bridges with holes for heat barriers, a large serpentine structure, and bridge structures with heat lenses. The amorphized structures attempted early on were shown to sag, necessitating the addition of holes as barriers, and later the adoption of the heat lens strategy. Earlier bridges were then modified with small holes to allow for characterization. Throughout, the utility of FIB fabrication was demonstrated as new designs and design modifications were implemented with relative ease and rapidity. The testing of the temperature gradients remains to be conducted when facilities become available, and there is potential for future work, which will likely consist of modified or alternative designs for the heat lens system, and some investigation of different combinations of methods for the reduction of heat conduction on the cool end of the bridges.

Chapter 4: Backside Milling with PFIB

4.1 Introduction

This project was a collaborative effort with TechInsights, with the aim of investigating the feasibility of using the xenon PFIB operated by the CCEM for milling backside access trenches for circuit investigation and modification. The use of the PFIB for this purpose would allow the operator to conduct the entire process of delayering, imaging, and editing integrated circuit devices in one machine within a reasonable time frame. Invaluable to this endeavor is the capacity for high beam currents (~100 nA – 2.5 μA) available with the PFIB (and the higher milling rates they enable), with the addition of potential mill rate acceleration using gas assisted etching.

Gas Assisted Etching (GAE) is a method involving the introduction of gas to a milling process (this can be done with FIB, lasers, or even SEM) in order to accelerate (or provide) the mill rate. In a FIB, gas is introduced locally so as not to disturb the vacuum. The gas then adsorbs on the sample surface where it is dissociated by the beam resulting in a chemical reaction after which the volatilized products are swept away by the vacuum. An advantage of GAE of particular interest for this application is that due to this volatilization of the products, redeposition is significantly reduced and higher aspect ratio mills can be achieved. [33]

In this case, the gas is introduced to the FIB chamber via the Gas Injection System (GIS), pictured below in Figure 45.

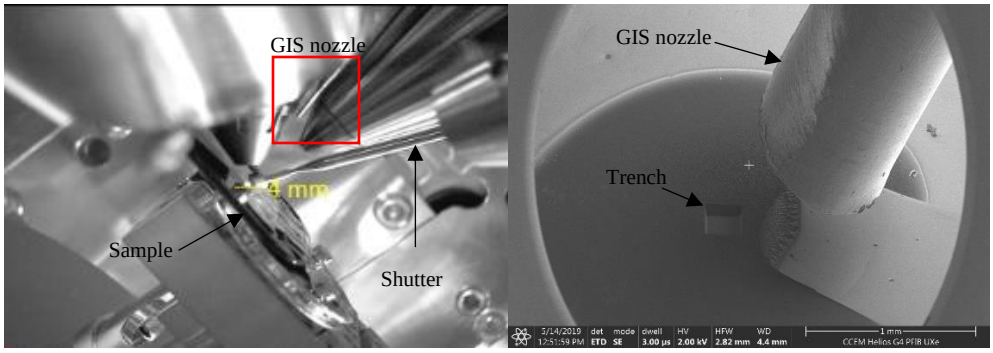

Figure 45: GIS chamber view and SEM view during operation

Xenon difluoride (XeF_2) was selected as an isotropic silicon milling etchant. The expected reaction is as follows:

$$2XeF_2 + Si = 2Xe + SiF_4 \quad [50]$$

Xenon difluoride offers a high etch rate (1-2 µm/minute without assistance) but can produce pitted and uneven surfaces as it does not require the ion beam to dissociate.

4.1.1 Primary Objectives

The primary objective of the TechInsights collaboration work was to assess the feasibility of and develop a functional method for backside sample preparation (local delayering) using the ThermoFisher Helios PFIB with the following goals:

- Determination of the material etch rate with the PFIB
- Determination of useable deep trench geometry
    - Trench base must be smooth and flat
    - Trench base should be ~ 200 x 200 µm
    - Trench depth should be accurate to within 10 µm
- Determination of the material etch rate with gas (XeF_2)

4.2 Deep Trenches

The initial prep work included several large trenches (on the scale of hundreds of microns deep). This was carried out using the 2.5 µA (the highest current available on the PFIB) beam for standard milling. Below are the very first tests done: a trench at ~150 microns deep with no modifications shown at a series of points during milling, followed by a trench that is ostensibly 200 µm deep and done in 50 µm deep steps with alternating scan directions. Step dimensions were laterally reduced by 20 µm at each step as later experiments were planned using stepped sides in order to broaden the trench opening and ensure that redeposited material would not have undue effect on access to the trench base. Trench 1, shown in Figure 46 was halted before the entirety of the projected 252 minutes was completed due to time constraints. The time at completion was 182 minutes, giving an expected depth of 108 µm approximately.

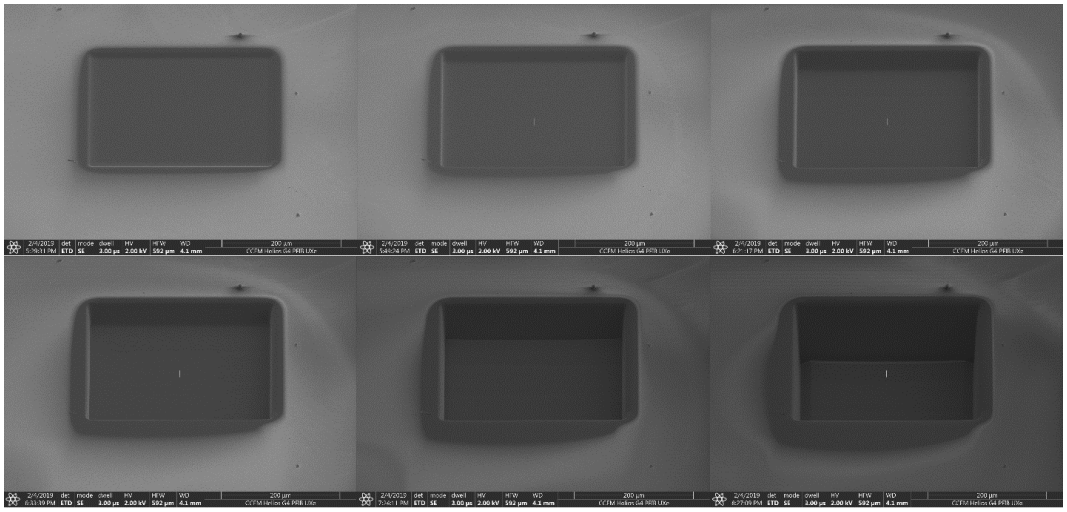

Figure 46: Trench 1: 300 x 300 x 108 µm rectangular mill at 2.5 µA at 12, 30, 60, 72, 120, and 182 minutes

An additional trench is shown in Figure 47 with one image at each step level, followed by one inclined image and one bird's eye image.

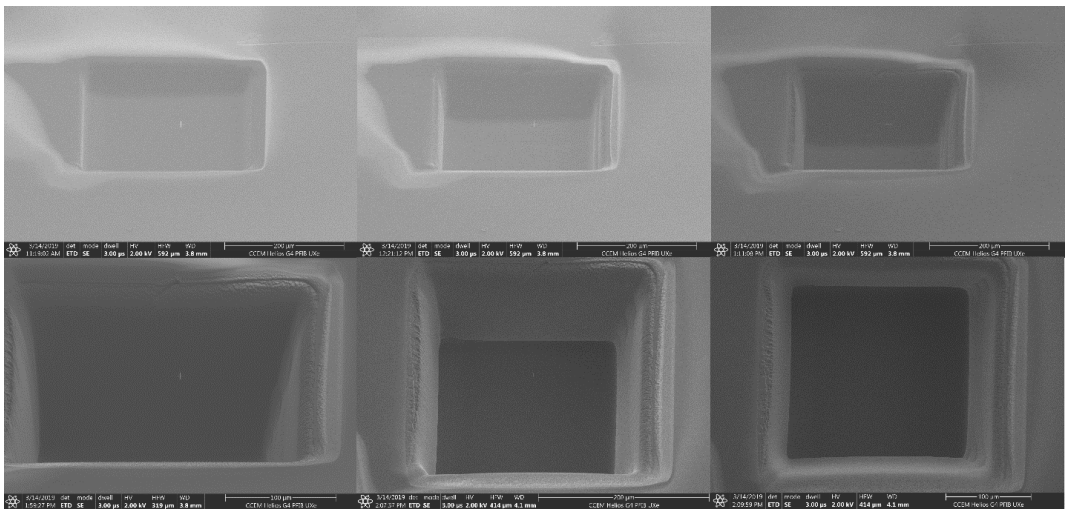

Figure 47: Trench 2: Stepped trench done in four 50 µm deep rectangular steps

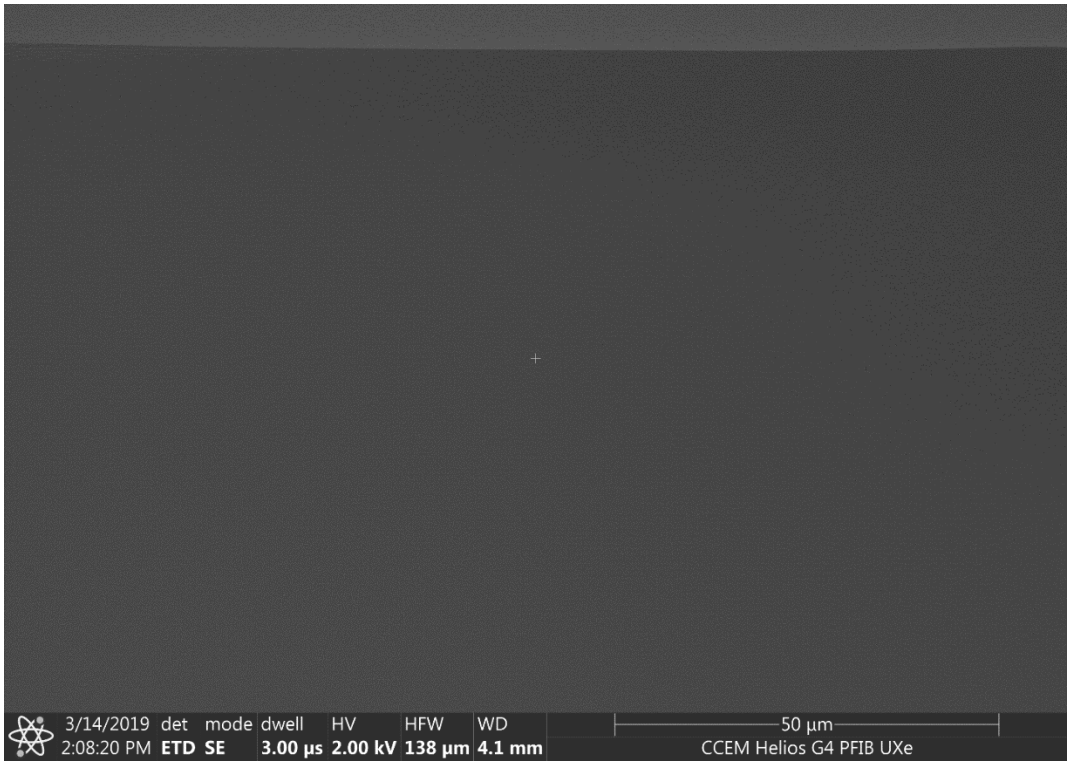

Figure 48: Base of Trench 2, notably smooth

In order to characterize the surface roughness and profile, several methods were investigated. The profilometers available were unsuited to the high aspect ratio of the trench and small feature size, and AFM was likewise not capable of functionally reaching the bottom surface. A form of optical profilometry was attempted, specifically a focus variation device (Alicona Infinitefocus). Unfortunately, the device does not read smooth surfaces (such as the reflective surface of a silicon wafer) very well, resulting in blank spaces where the surface becomes too smooth. The method is still useful in determining whether the bottom surface is smooth enough to be similarly reflective to the surface.

Images of the focus variation characterization can be seen below in Figure 49.

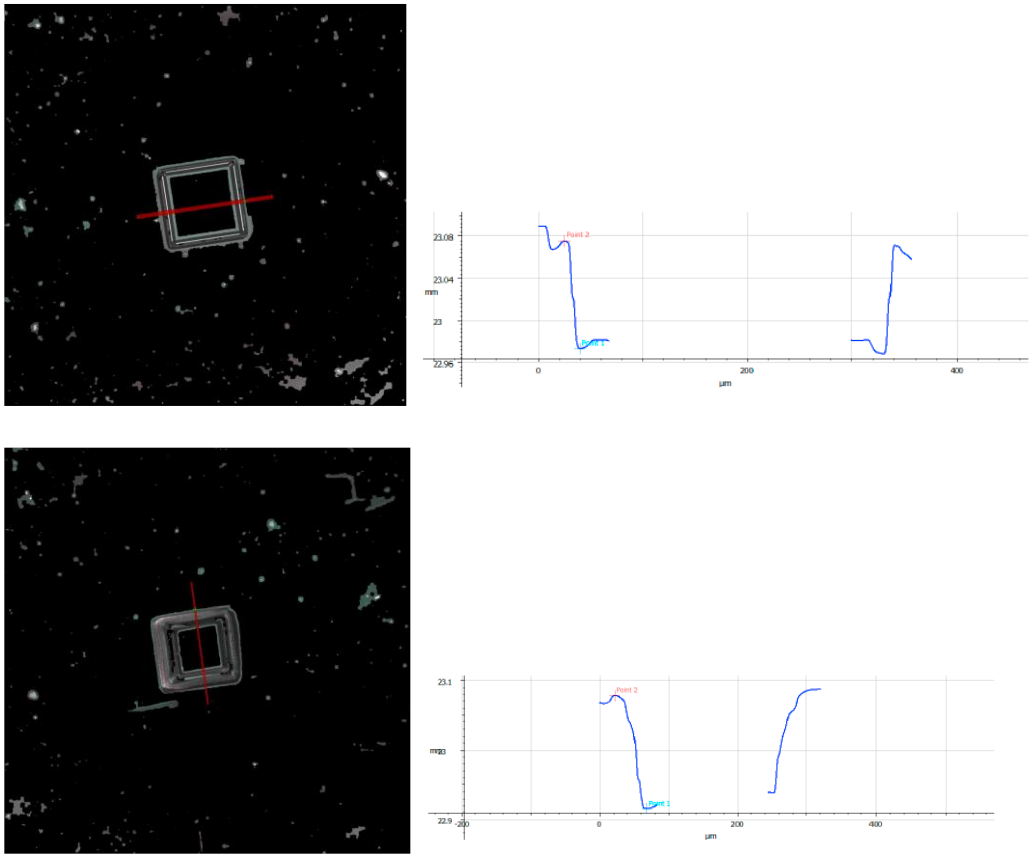

Figure 49: Alicona Infinitefocus images and profiles for trenches 1 and 2 respectively. Red lines indicate scan direction for profile

Due to the material limitation of the focus variation system, it was decided that the most functional method of determining etch depth and surface quality would be to carry out a series of large-scale trenches at a variety of depths and then cross section them for analysis. Images of these tests can be seen below in Figure 50. The large circles surrounding each image are likely redeposited material.

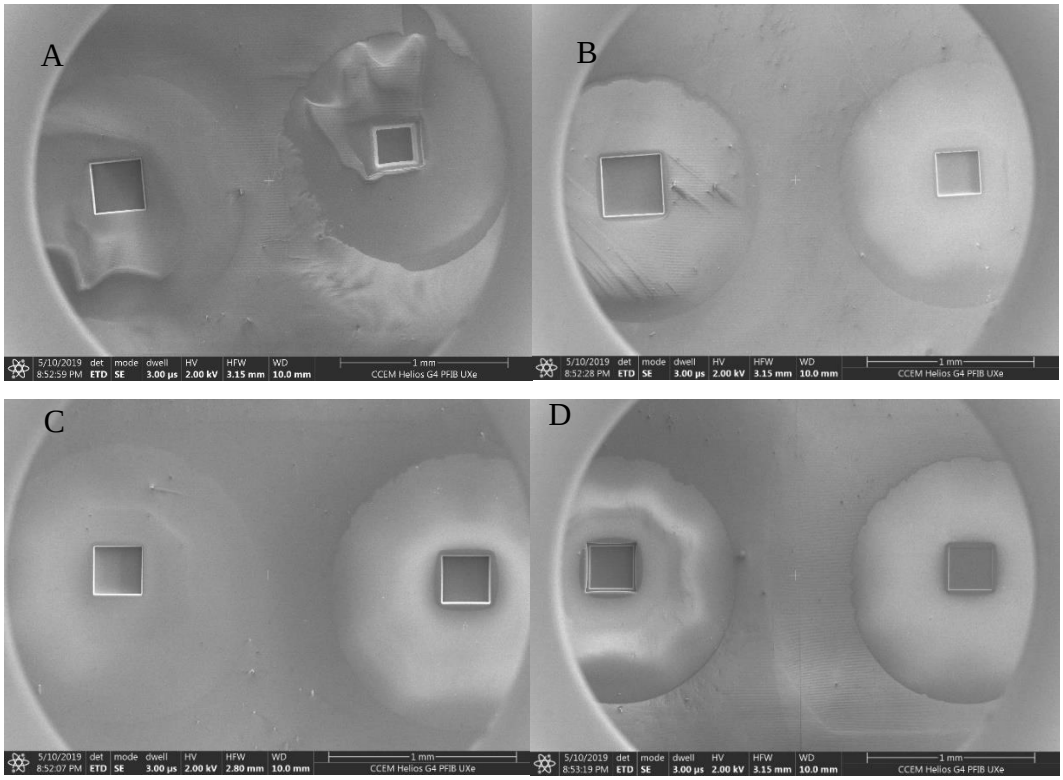

Figure 50: Bird's eye view of trench sides A) 1, 2 B) 4, 5 C) 6, 7 D) 8, 9

Platinum pads were deposited to ensure contrast with the base material, and cross sectioning was carried out. This process is illustrated in the images below from site 7. In order: Site 7, the platinum pad on the surface, and the cross section with measurements.

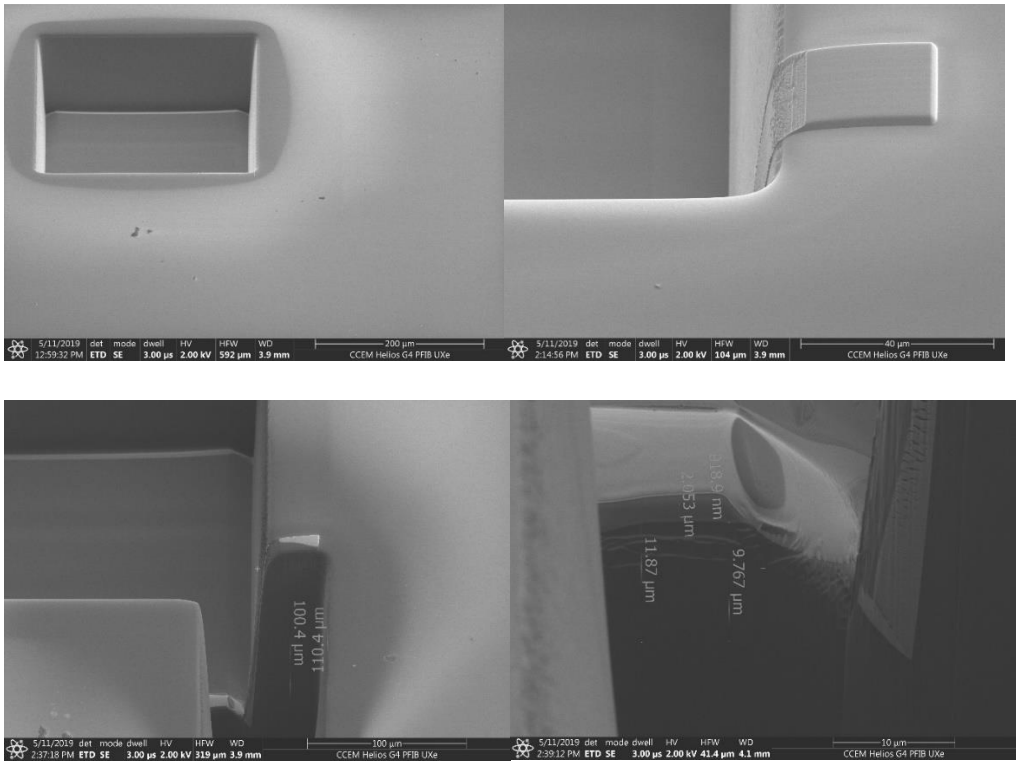

Figure 51: Clockwise from top left: Site 7, deposited pad, close up of cross section, cross section

For comparison, below is the stepped trench at site 8, which was carried out in two cuts of 50 µm depth, with lateral dimensions reduced by 50 µm on the second step.

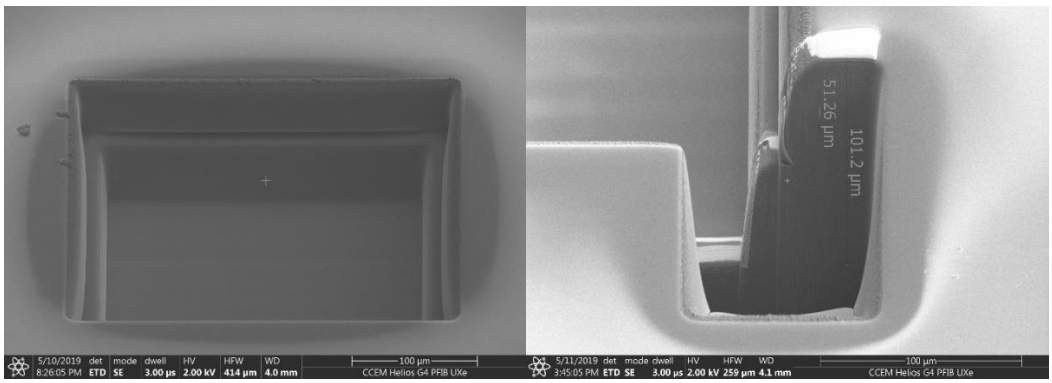

Figure 52: Site 8 and site 8 cross section displaying measurements of both steps

Based on the data found overall, the etch rate as calculated by the software appears to be accurate to within 10 µm at large depths (~100s of µm) and is ~46500

μm^3/minute. Having verified the standard mill rate, the next step was the investigation of the gas assisted etching options.

4.3 Gas Assisted Etching

4.3.1 Experiments

The highest priority task was the development of the gas assisted etching (GAE) method. XeF_2 can offer extreme acceleration of the etch process and is thus of great interest when developing processes.

There are some problems associated with XeF_2, one of which is the pitting that occurs as a result of the highly corrosive nature of the gas. This pitting occurs both globally and (if the etch parameters are poorly chosen) locally in the region of interest. The other is the challenge of matching the ion current, raster parameters, and gas flow to achieve an optimized etch rate. Seen below is an image of the first XeF_2 test, carried out before the visit. Note the damaged area around the ROI.

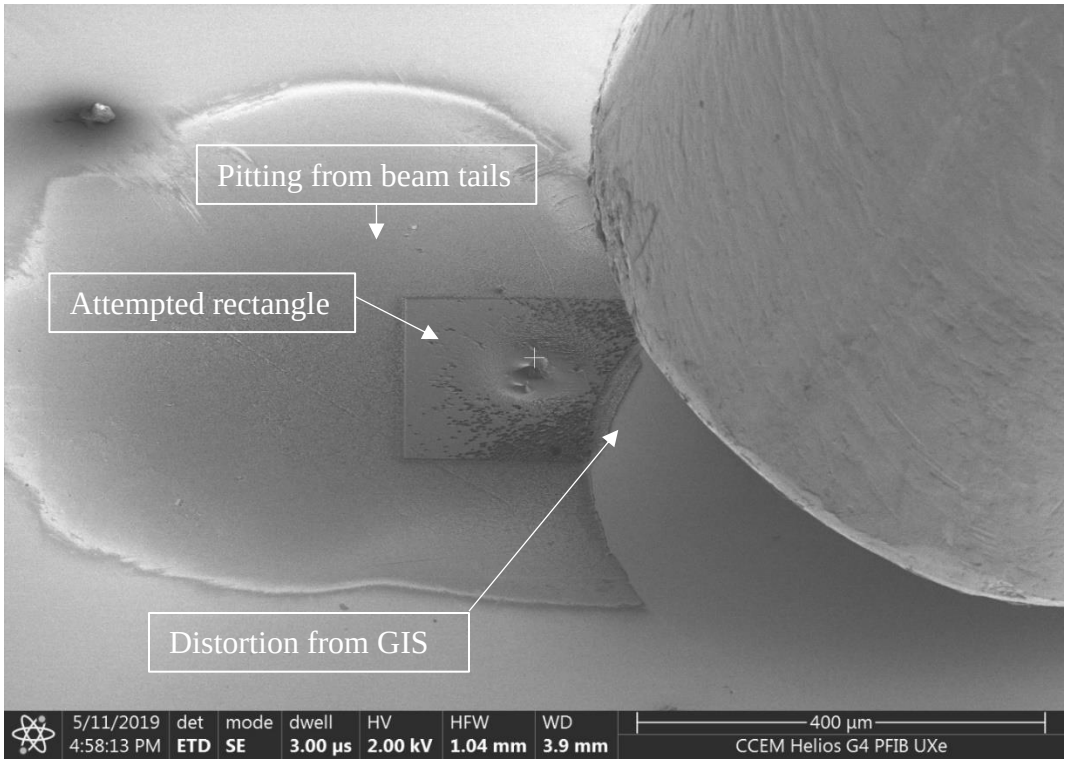

Figure 53: Initial xenon difluoride etch test

This test was an attempt to mill a simple square of 5 micron depth into the surface using GAE. As can be seen from the distortion in the pattern, the GIS nozzle was placed in the path of the beam. Below is a close-up of the damage to the surface.

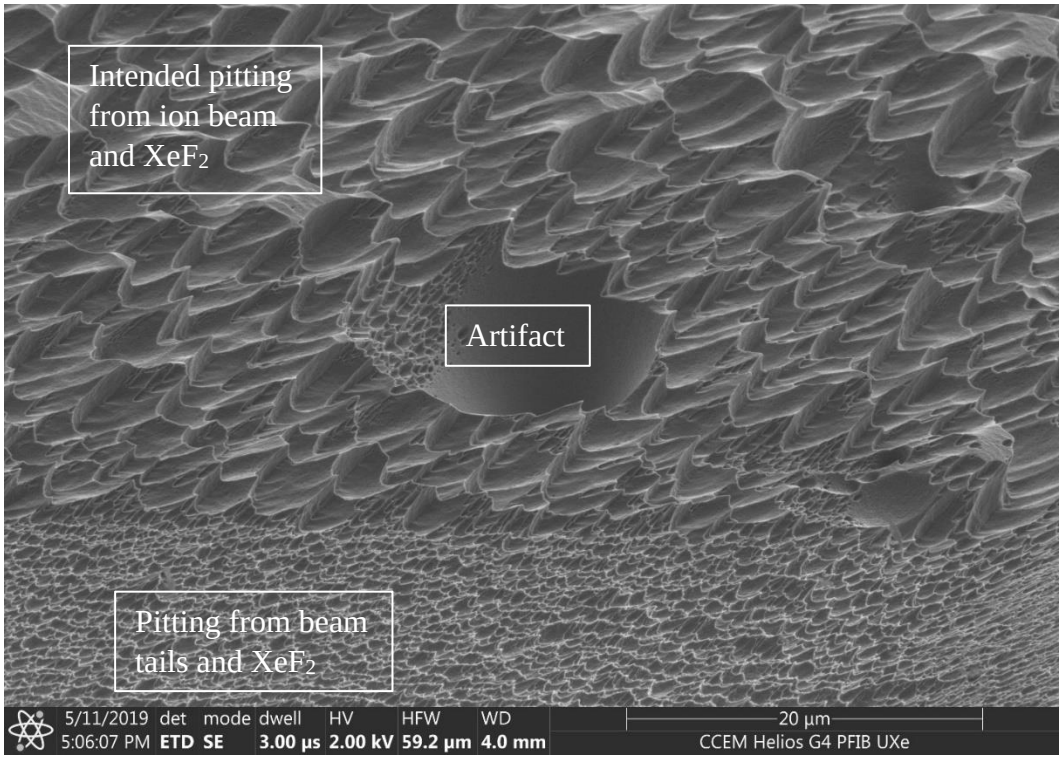

Figure 54: Close up of surface damage from initial GAE test

The first step that improved the pitting issue was to conduct a shallow polish mill (standard mill at 2.5 µA, 5 µm deep) to smooth the surface of the chip in the ROI. This reduces the likelihood of pitting due to surface defects or contamination.

A series of tests, shown in Table 4 below, were conducted to determine the effects of refresh time, dwell, gas flow, overlap, and beam current. Quality (surface roughness) was determined by observing SEM images of the trench surfaces and rated on a scale from 1 to 6 with 1 being the best quality. When varying the current it was discovered that the gas nozzle and the safety shutter used to protect the electron column (from sputtered material) during high current milling were incompatible. This restricted the upper current that could be used to 60 nA, as otherwise the milling would commence without the shutter engaged and could have resulted in contamination of the electron column.

Table 4: GAE Results

Refresh (ms)	Dwell (ns)	Flow (%)	Overlap (%)	Current (nA)	Quality
0	25	5	50	60	1.25
0	25	2	50	60	1
0	25	5	50	15	4
10	25	5	50	60	5
0	25	5	0	60	5.5
5	50	5	-115	15	5

The first row of Table 4, highlighted in grey, represents four tests with the same parameters. These were the parameters selected for the working recipe due to consistent results and good surface quality. Green cells indicate a value higher than the 'reference recipe', while orange cells represent a lower value. The goal of this process was to establish a functioning method for GAE, and as such experimentation was halted once a repeatable recipe for producing a smooth trench bottom was achieved.

Due to the number of parameters, PCA was attempted in order to determine which variables were relevant. Bartlett's test of sphericity returned a value of 1.91 (significantly above the 0.05 cutoff) suggesting that the variables were statistically unrelated. ANOVA was then attempted but was not meaningful due to insufficient data. Manual observation of the data suggests that refresh time, overlap, and current are the strongest influences on surface quality, with lower values of refresh time and greater values of overlap and current producing better results. This in turn suggests that the primary cause of poor surface quality is excess gas adsorbed on the sample surface. As xenon difluoride does not require the ion beam to dissociate,

excess gas may etch in a non-uniform fashion, resulting in undesirable pitting on the trench base. With respect to the model discussed in the theory section, it is possible that the smaller gas to ion flux ratio reduces the overall yield but that the surface roughness may also be reduced to some degree.

Below are images of site 12 to demonstrate a good quality trench surface and contrasting images of sites 18 and 19.

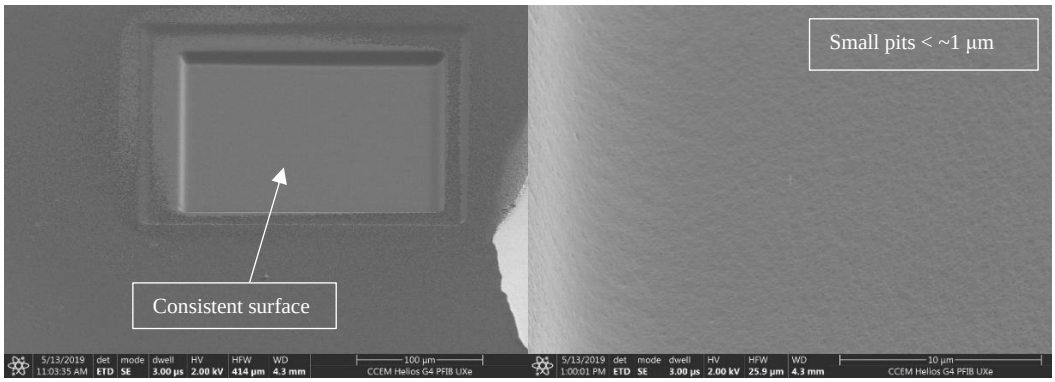

Figure 55: Site 12 GAE test, quality rating 1

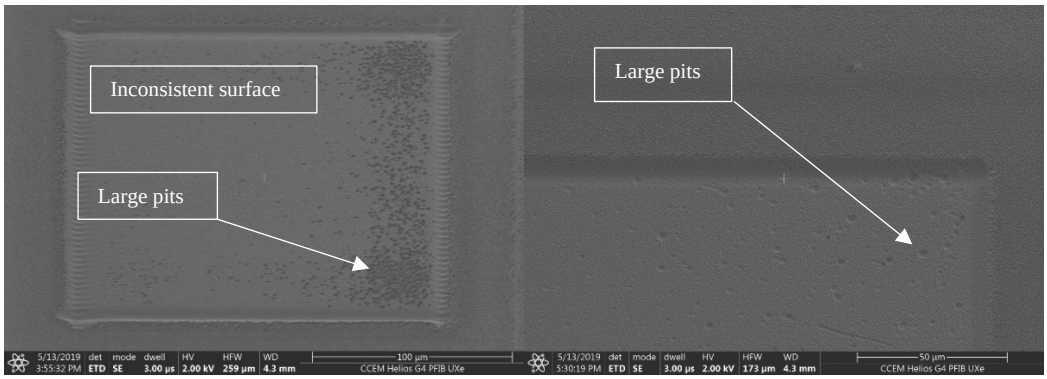

Figure 56: Sites 18 and 19 GAE tests, ratings 5 and 4 respectively

Note that in the images of sites 18 and 19, the pitting is inconsistent across the trench and pits larger than 1 µm are common.

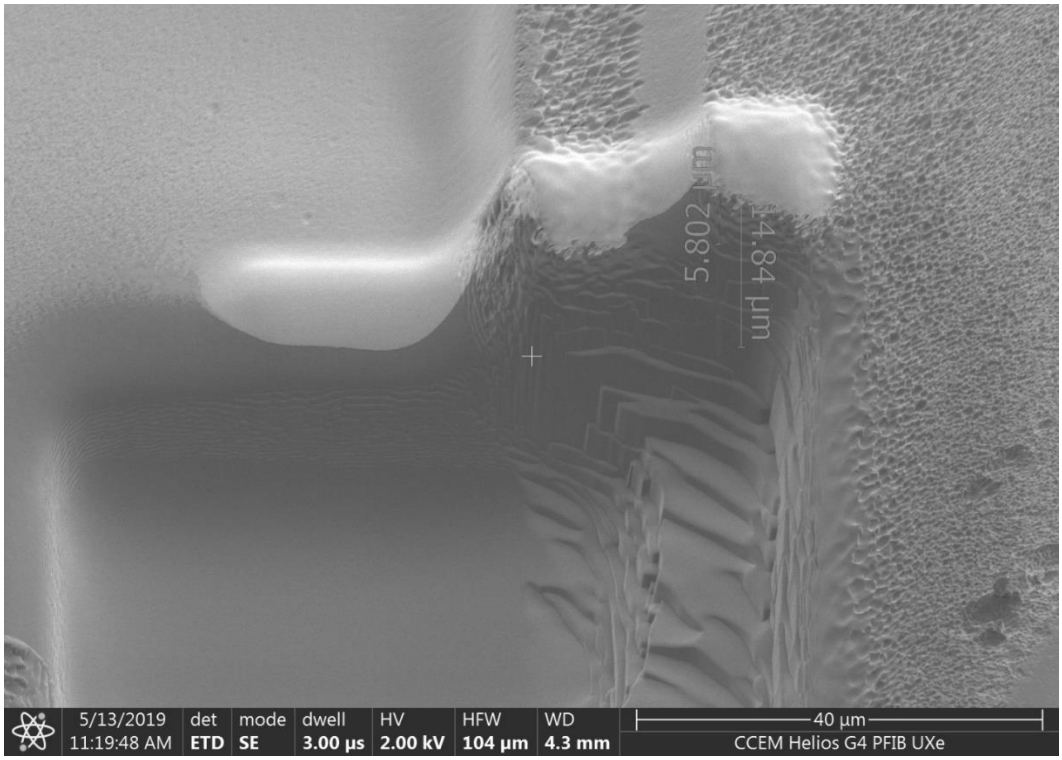

Figure 57: Site 12 cross section

Cross sectioning of good quality trenches (as seen in Figure 57) indicates that the best result was approximately 40000 μm^3/min. While this speed was initially considered to be insufficient, further examination revealed that this was an improvement of 31 times. This was determined by noting that the etch rate of 60 nA with XeF_2 was on par with the etch rate for an unassisted 2.5 µA beam, and then calculated from the time difference between an unassisted 60 nA beam and the unassisted 2.5 µA beam.

After coming to this conclusion, an experiment was designed to study the trenching effect. This attempt was halted after two steps, as it was noted that the removal rate of the GAE being the same as (or less than) that of a 2.5 µA beam but without the safety shutter was a potential danger to the electron column. The final image of the attempted run can be seen below, displaying the characteristic damaged area and a notable distortion of the trench base which we hypothesize is due to gas flow

dynamics at the bottom. As this suggested a limitation based on the nature of the GIS, it was noted that continuing with GAE as a primary method would require the acquisition of a dedicated GIS with symmetrical flow.

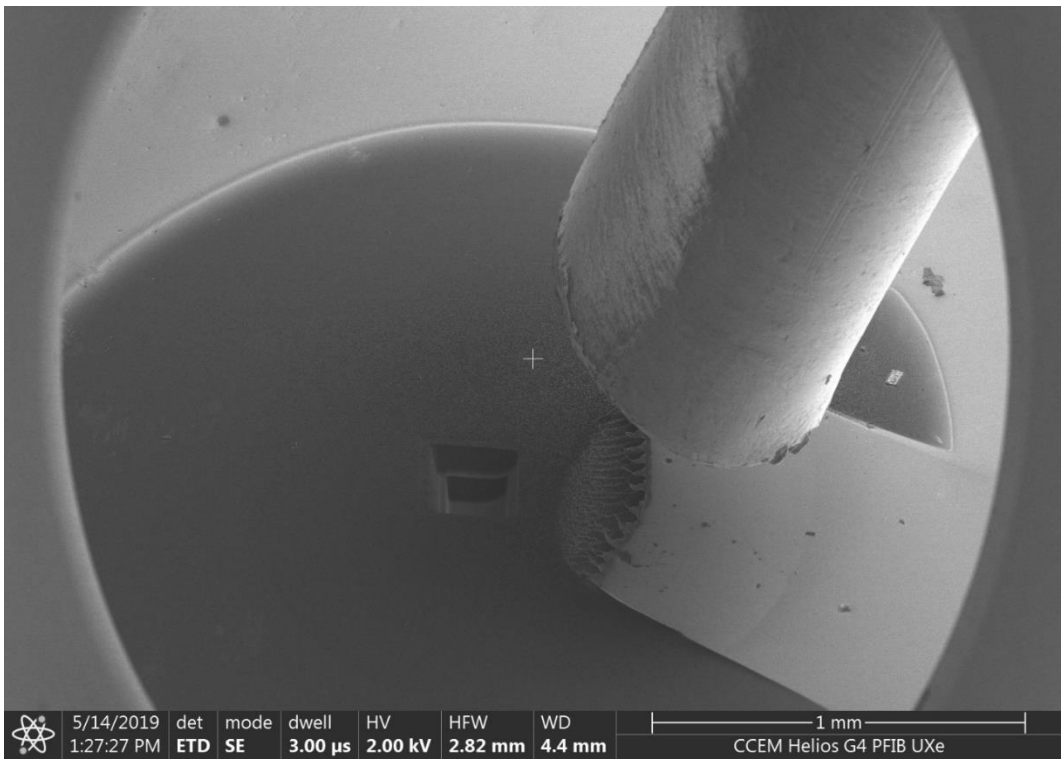

Figure 58: Final GAE Test site 26. Done in two steps, 100 microns deep in total.

As we did not wish to further imperil the electron column, we elected to set aside the GAE experiments and proceed using the standard mill at 2.5 µA for the remainder of the deep trench experimentation.

The preliminary experiments demonstrate great promise in using GAE with a Xe-column plasma FIB to etch backside silicon and remove materials rapidly. A dedicated circuit edit system with a suitable symmetrical nozzle and a proper shutter to protect the electron column should work well for high material removal rate applications.

4.4 Final Deep Trenches

Based on the quality of earlier trials, two final 200 μm deep trenches were cut with the goal of examining the trench base profile at something approaching viable working depths. Both trenches were originally planned as 300 μm deep trenches, but in order to keep the milling time within the limits at hand, both were reduced, taking 5 hours and 44 minutes, and 4 hours and 6 minutes respectively. The first trench was cut with lateral steps of 50 μm ending in a 200x200 μm base with z steps of 50 μm, and the second trench was cut with lateral steps of 25 μm ending in a 200x200 μm base with z steps of 50 μm.

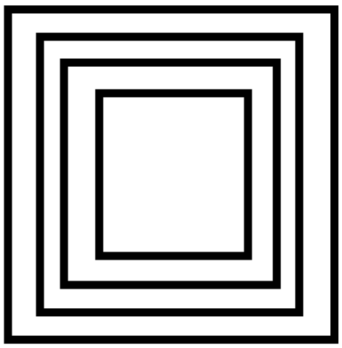

Figure 59: Deep trench mill pattern, four steps

Both had alternating raster patterns on each step starting on the first step and continuing as: bottom to top, top to bottom, left to right, and right to left. This was earlier shown to reduce deformity of the trench from redeposition.

Below are the bird's eye views of the 50 μm lateral step and 25 micron lateral step trenches. The 25 μm step trench has been cross sectioned in this image.

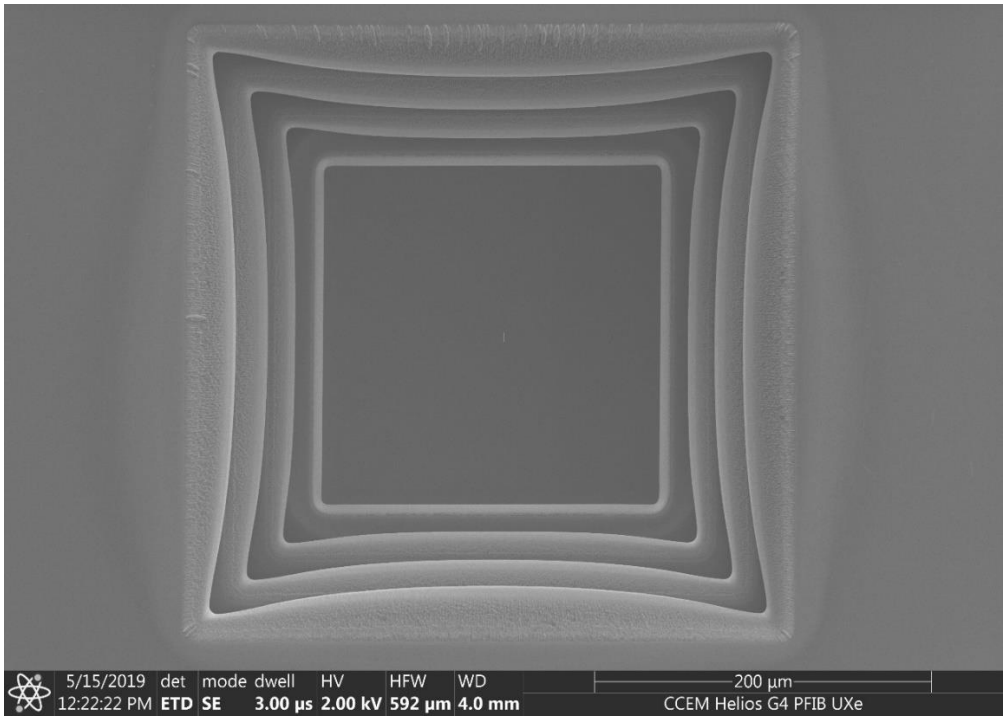

Figure 60: T1 50 micron lateral step trench

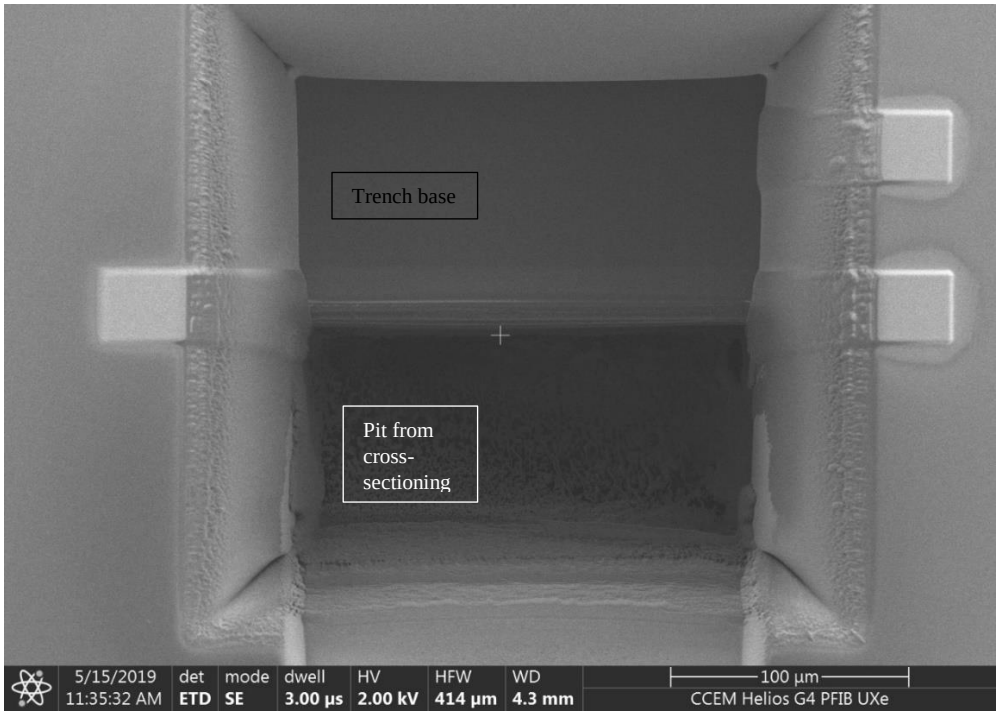

Figure 61: T2 25 micron lateral step trench, cross sectioned

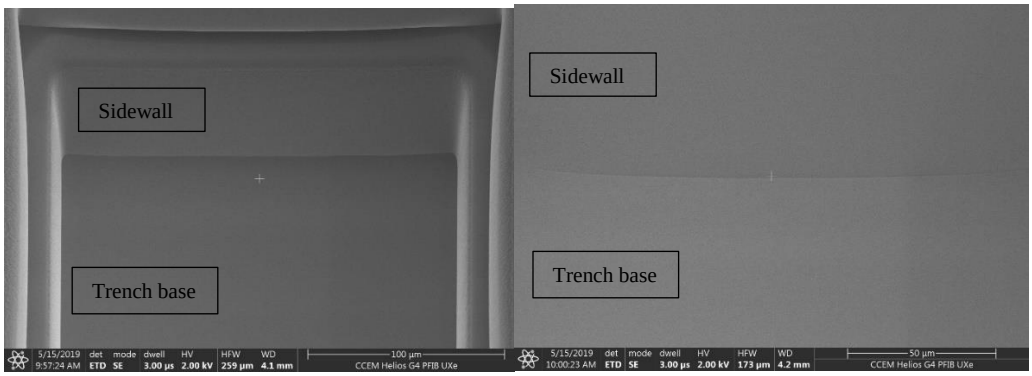

Figure 62: T1 and T2 trench bases

Above are the images of the bases of T1 and T2, showing relative flatness. Below are the images of the cross sectioned trench bases. The paler material is the deposited platinum.

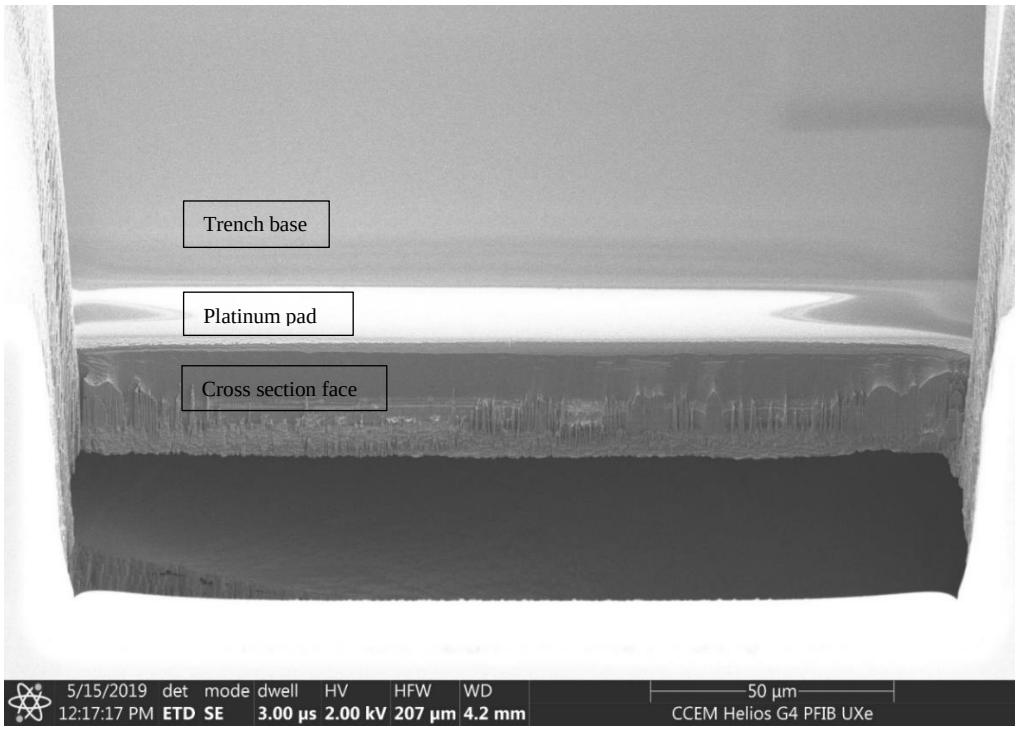

Figure 63: T2 Cross section

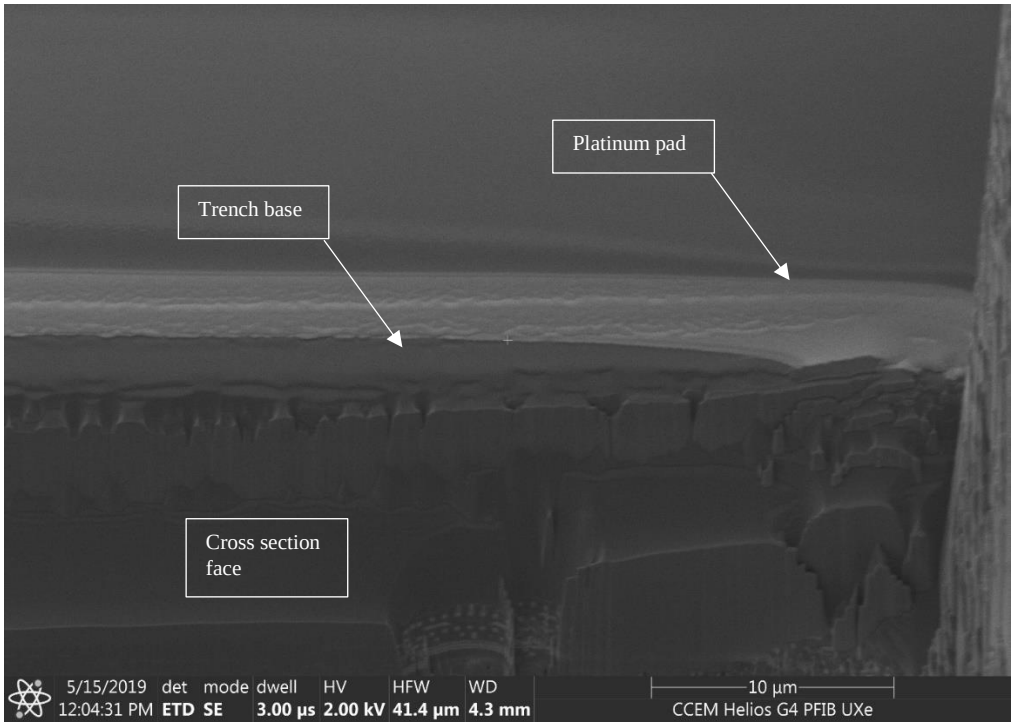

Figure 64: T2 right side bottom geometry

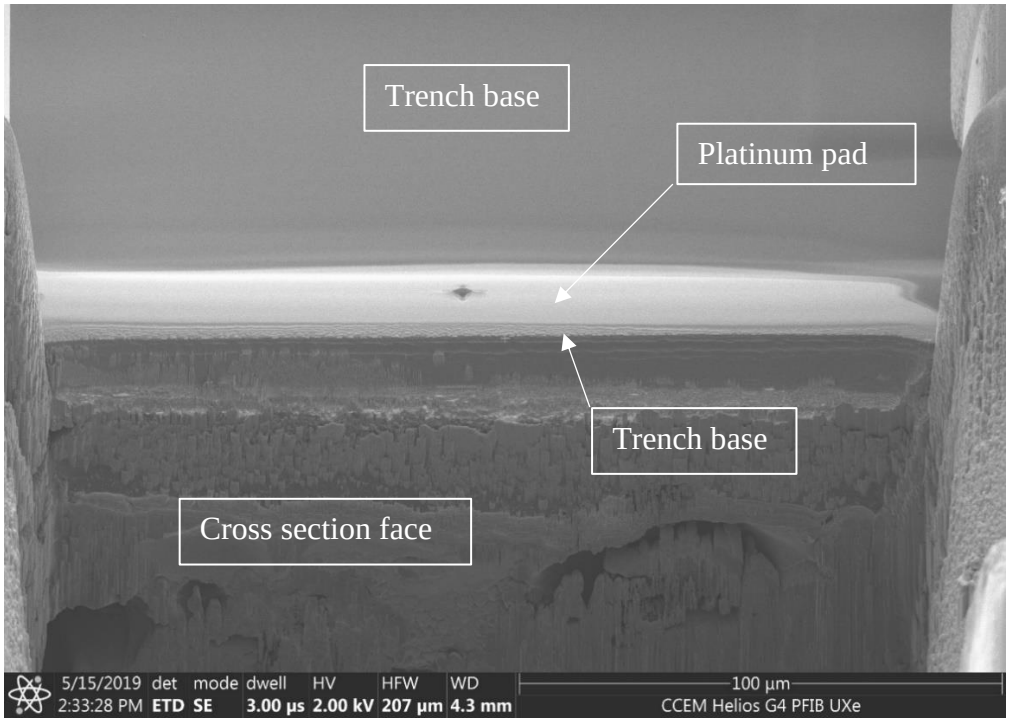

Figure 65: T1 Cross section

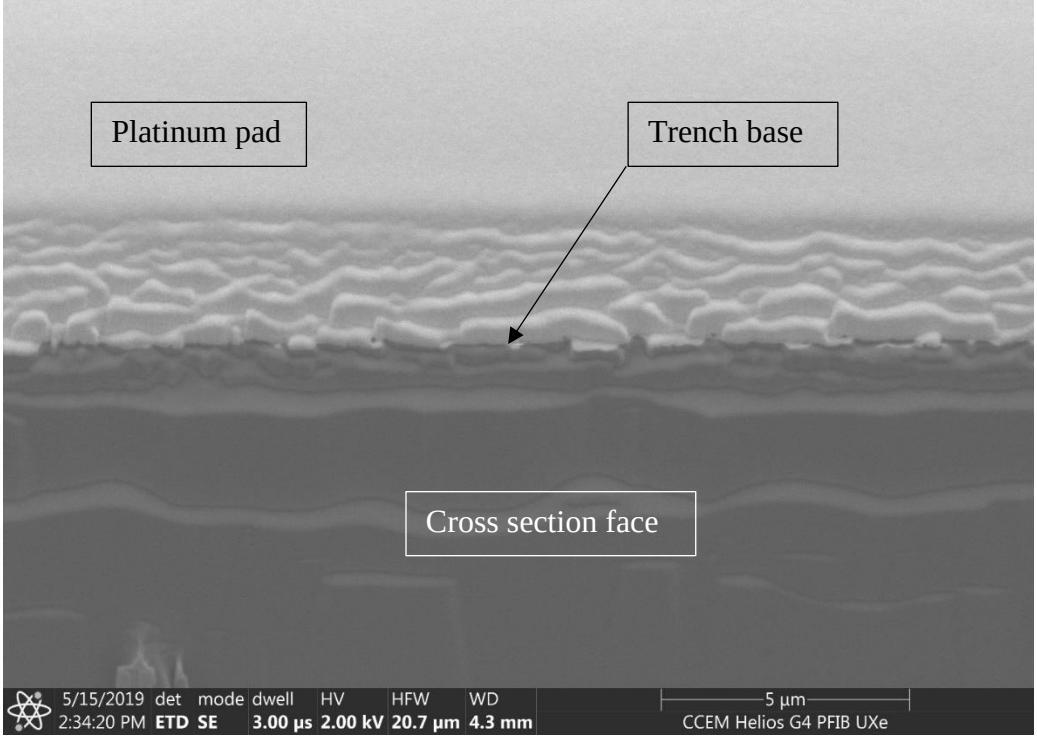

Figure 66: T1 Centre surface

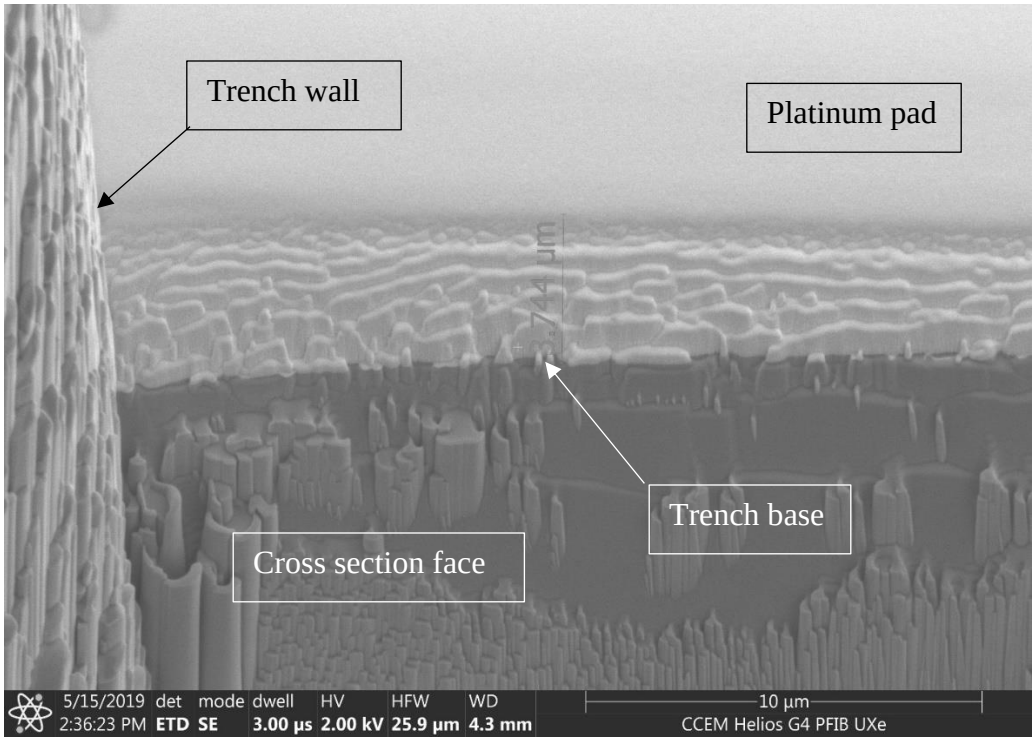

Figure 67: T1 Left side surface shape

It is somewhat unclear from the cross sections whether the base of T1 is rougher. It appeared so under the initial cross sectioning, though this effect was reduced after a polishing step. Polishing had to be carried out at high current (1 µA) due to the size of the cross section and time constraints. The surface geometry of T1 appears flatter overall, where T2 exhibits a slight swelling towards the middle, likely redeposition resulting from the reduced lateral step.

An additional experiment conducted along with the deep trenches was the deposition of platinum intended to undergo resistance testing later by collaborators at TechInsights. While tungsten would have been ideal, the deposition parameters for platinum were better established. Due to time constraints, the pattern was modified into three separate depositions in parallel milling. Two 25 µm square contact pads and one 150 um long “wire” ~10 µm wide. Some shadowing of the pads appears to have occurred during the deposition, as can be seen below.

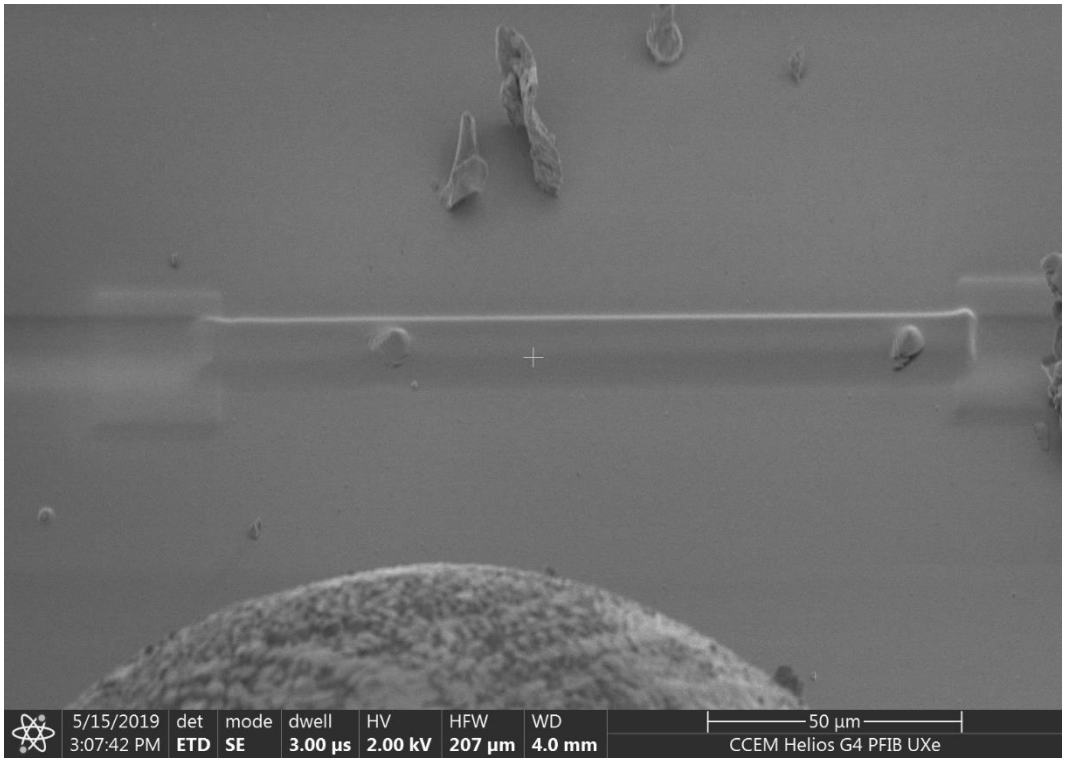

Figure 68: Platinum deposition for resistance testing

Further experimentation was planned, consisting of two further trials on working devices, an additional trench on a functioning memory chip that would then be tested for functionality, and a large scale cross section to be carried out to achieve backside access to a gorilla glass protected device, but due to expense only the glass device cross section was attempted.

4.5 OLED Cross-Section

The device in question was composed of gorilla glass and unspecified polymers and was around 1.3 mm deep. It was proposed that a cross section be attempted with PFIB as cross sectioning with traditional methods proved to be cumbersome and

time consuming. Due to the extreme scale (for a FIB cut), the cut was conducted at 2.5 μA in order for maximum speed. The final dimensions selected for the cross section were 500 x 500 x 1100 μm. Due to the size of the device and insulating nature of the material, the device was mounted on a clip stub with a substantial amount of copper tape to aid with conduction (seen in the bottom left panel below). The cut was conducted at 1 μs dwell time and 85% overlap, and took 30 hours, 24 minutes, and 52 seconds.

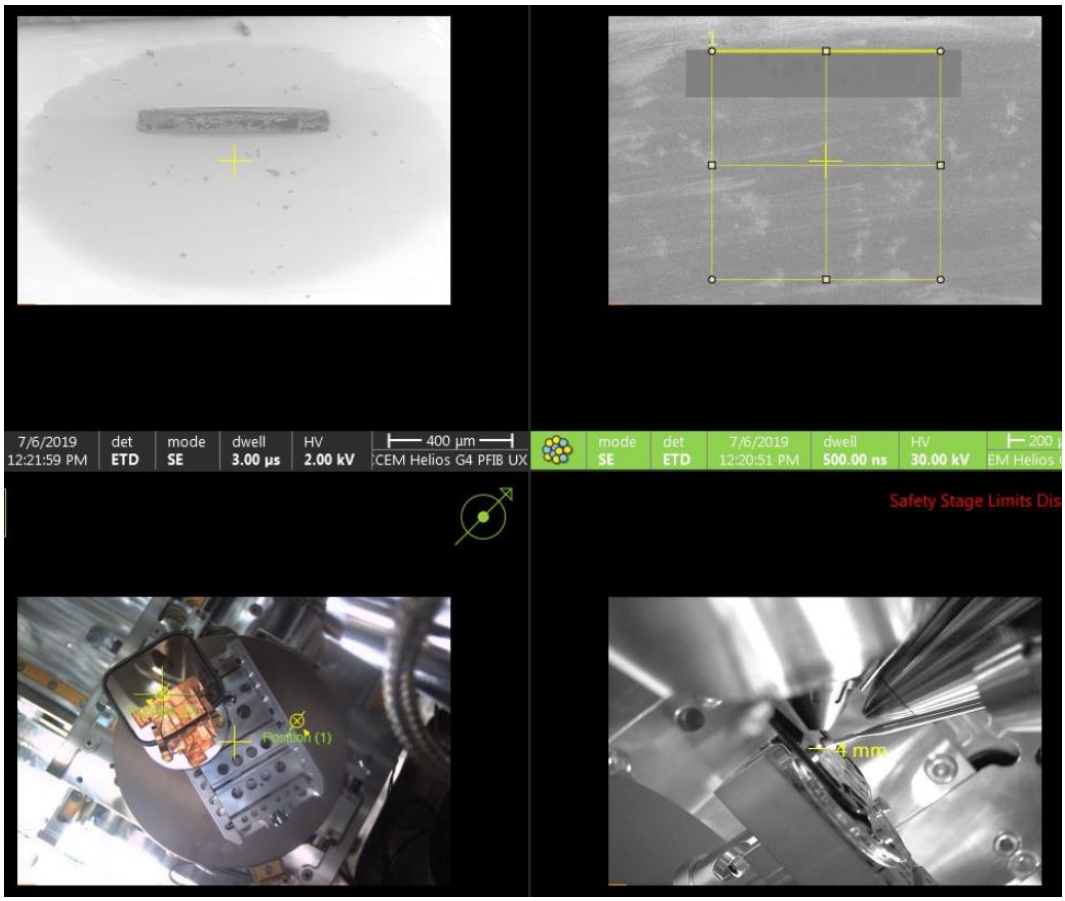

Figure 69: Clockwise from top left: SEM view of cut, Ion beam view of cut, infrared chamber view, navigation camera view

A brief initial cut was conducted to ascertain the surface effects. This can be seen above in the top two panels. It is notable that the surface appears to have melted somewhat during milling. A larger image is provided below.

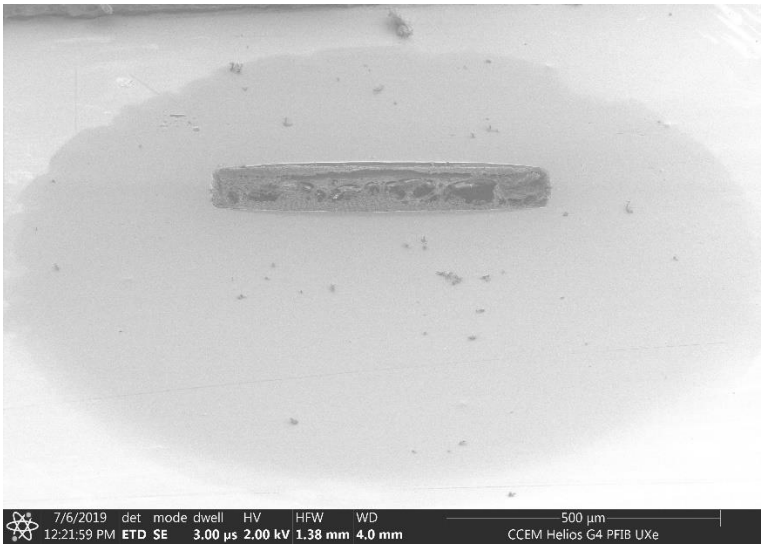

Figure 70: Surface after initial mill. Note melted surface quality.

The case of this is likely heating from the beam, as can be seen in the close up image below, where a small glowing spot at the milling region can be seen in the infrared camera feed from the chamber.

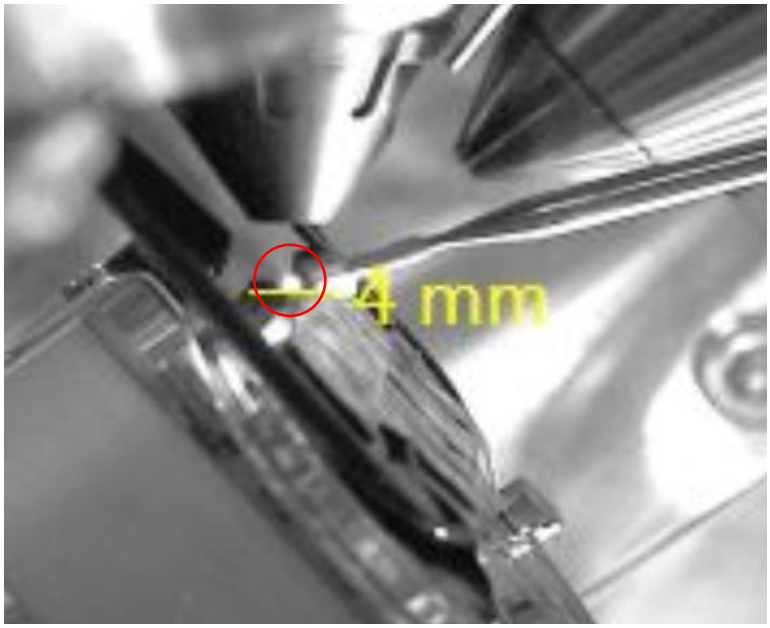

Figure 71: Close up of thermal glow captured by infrared chamber camera (4 mm marker is for stage navigation and does not indicate scale)

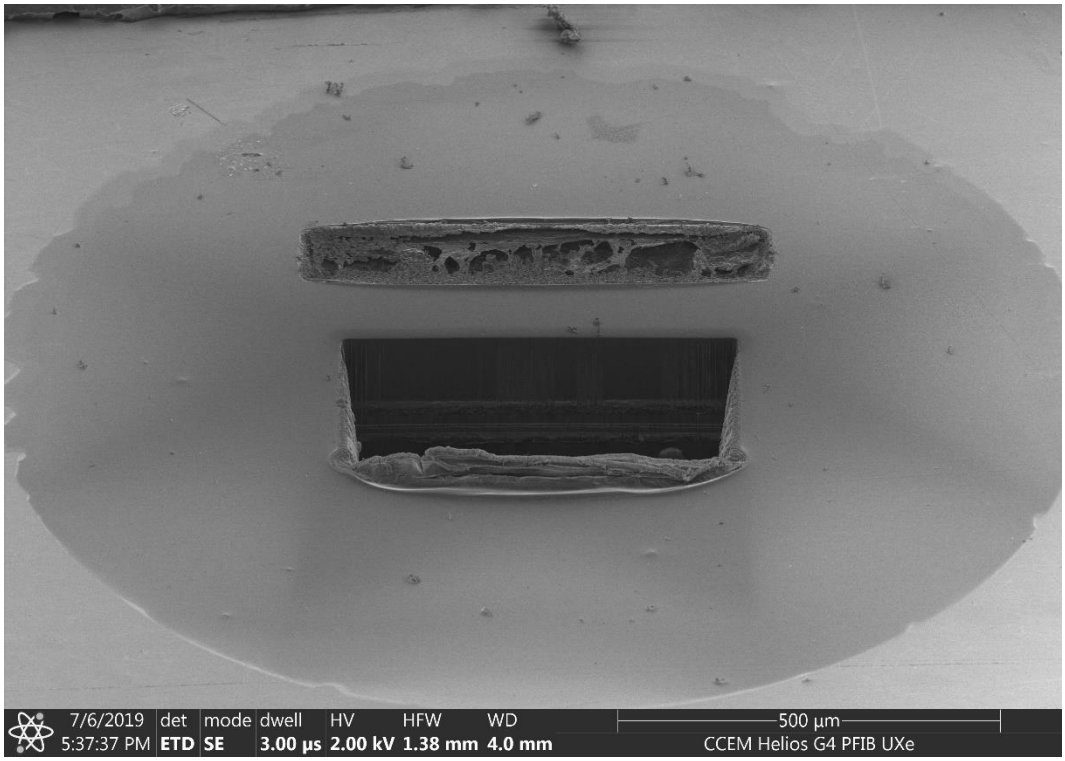

Figure 72: Cut at 25 hours, 16 minutes, 43 seconds

Above is an image of the cut 25 hours in. Some internal structure appears to be visible at this point. Below are images of the completed cross section at 52 degrees, 0 degrees, and 25 degrees with tilt correction. Notable is that the apparent structure is no longer visible.

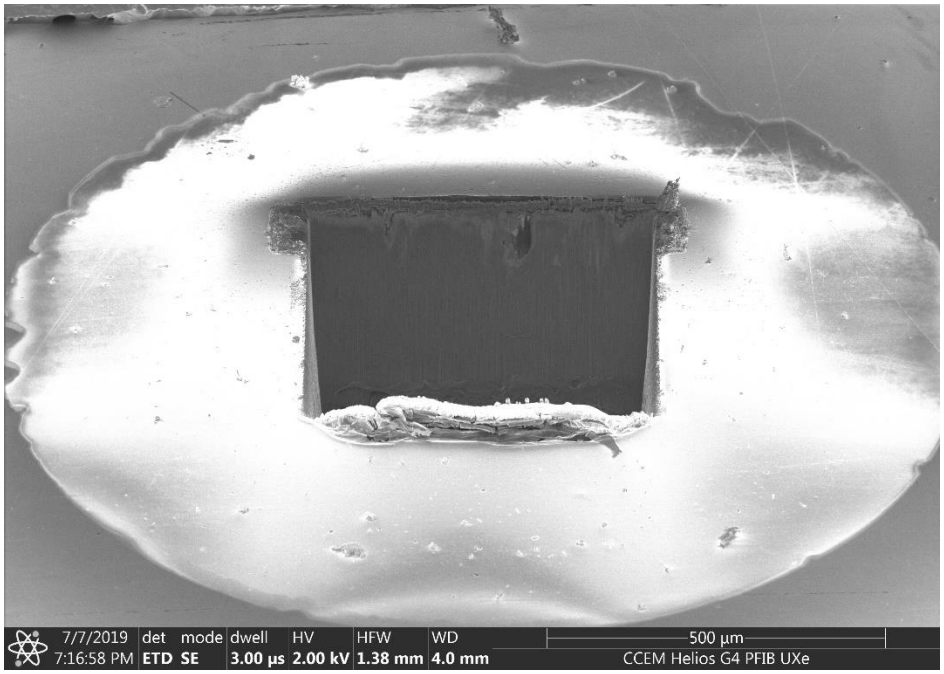

Figure 73: Completed cut at 52 degrees

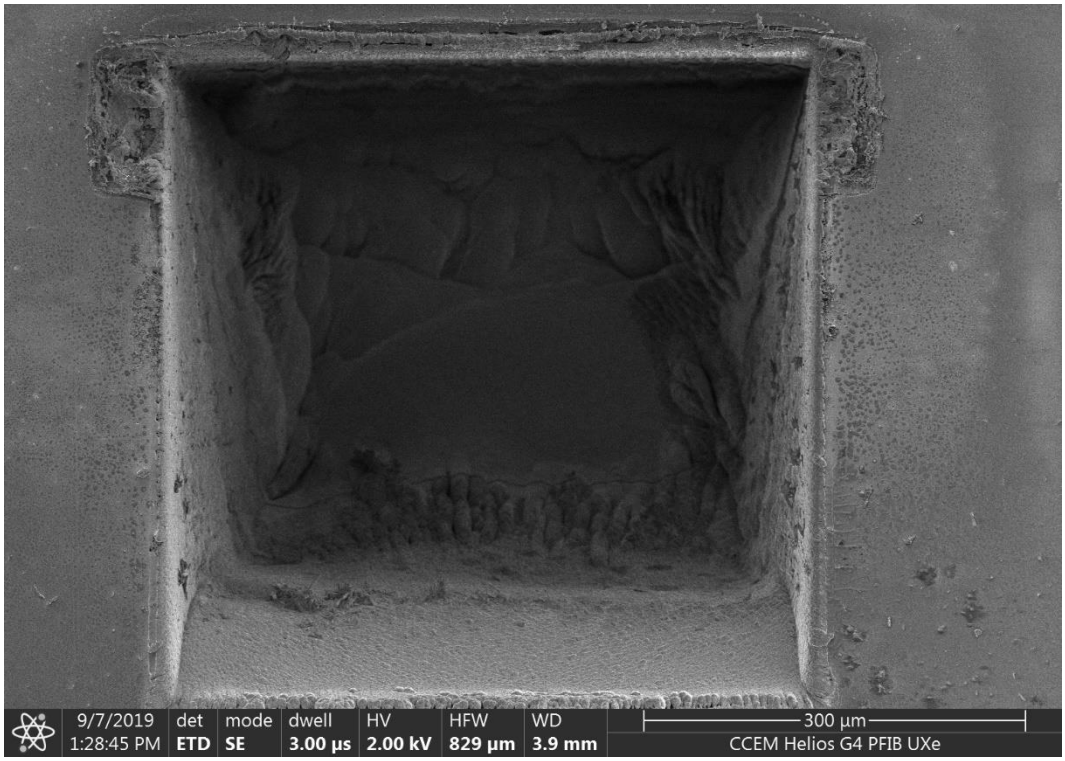

Figure 74: Completed cut, bird's eye view

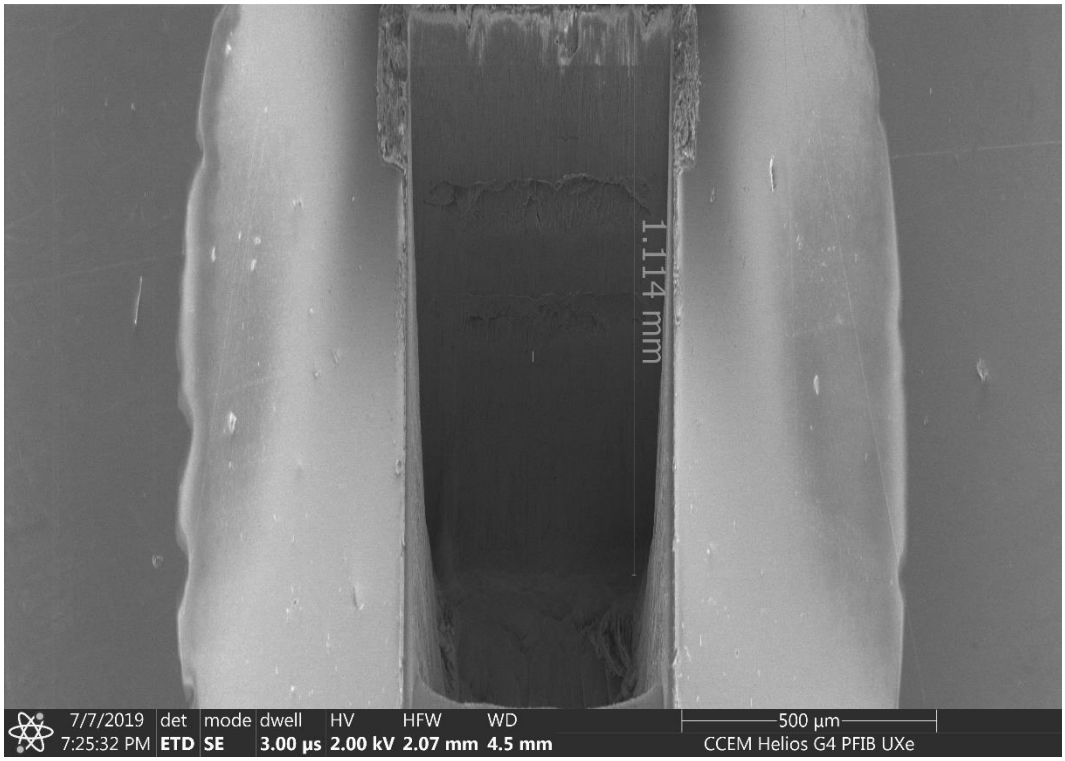

Figure 75: Completed cut at 25 degrees with tilt correction

By observing images without tilt correction applied and using trigonometry, the final depth was found to be between 1074 and 1224 µm. This was deemed reasonable for a target depth of 1100 µm.

As the internal structure was not clearly visible, several cleaning cross sections were applied in an attempt to polish the surface. Very small areas were exposed at 30 pA, 4 nA, and 15 nA, but did not seem significantly better than areas exposed at 1 µA. As using the lower currents would be extremely time consuming, 1µA was selected at the polishing current.

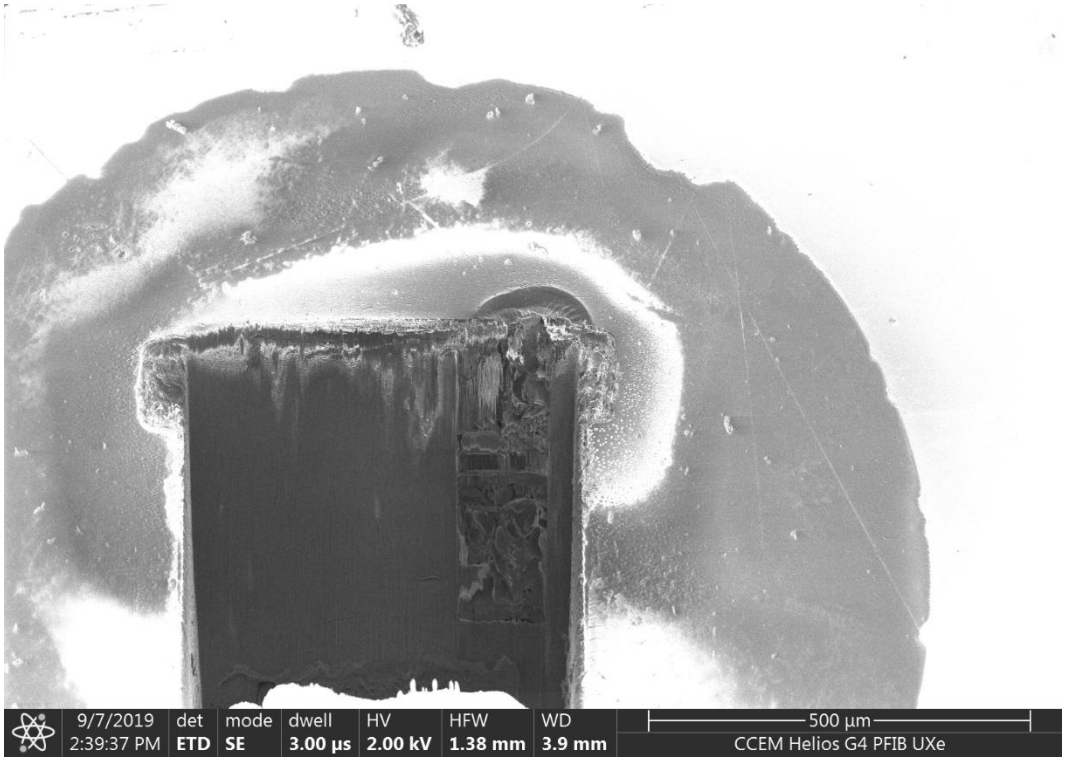

Figure 76: First cleaning cross section at 1 µA

While the surface quality does not appear to be very high, it was clear that there was some internal structure visible, and so an additional polishing round was conducted to clear more of the surface.

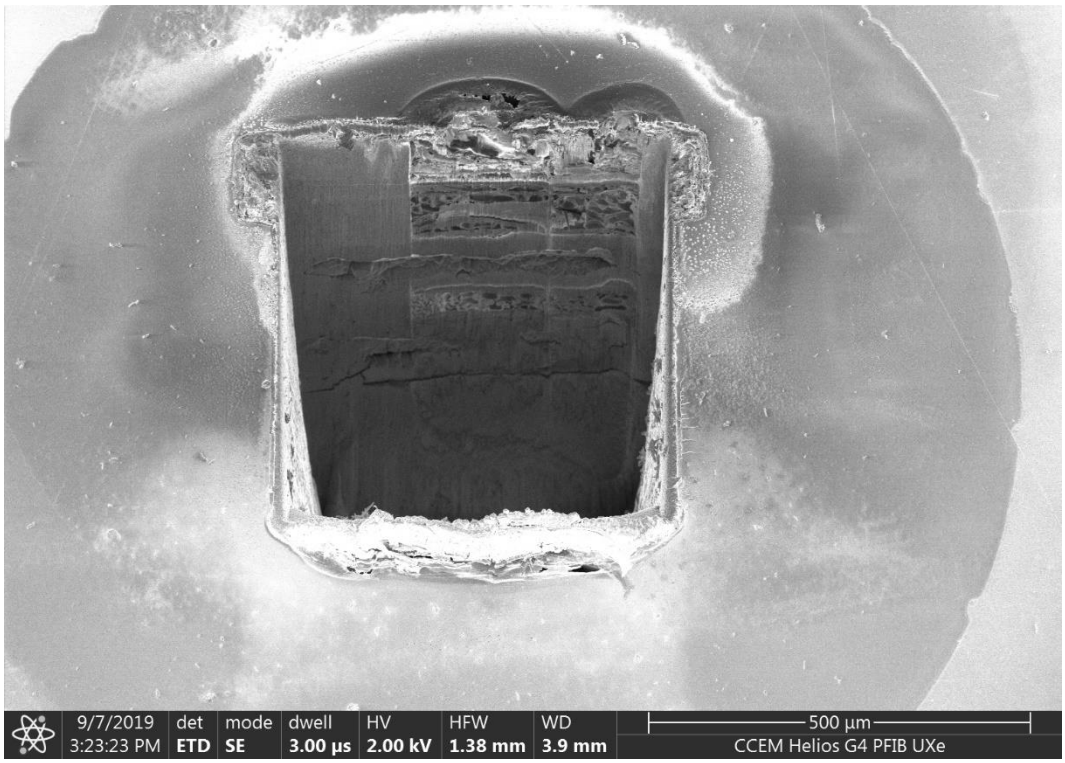

Figure 77: Both cleaning cross sections

Here again, it is clear that some internal structure is present, but it remains partially obscured by the melted material and inconsistent surface quality.

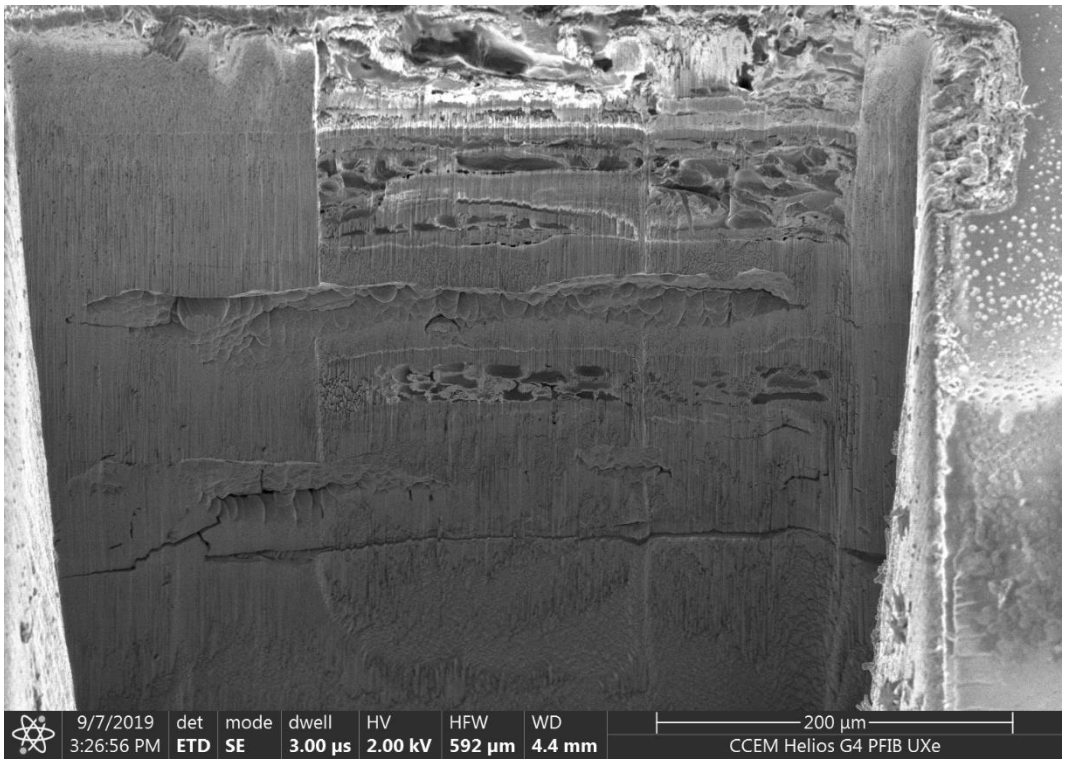

Figure 78: Close up of cross section after polishing rounds

Above is the final state of the OLED cross section project. The internal structure remains partially obscured, though it is clearly present. It may be possible to further clarify the structure with additional polishing rounds, the use of a pad, or modified milling parameters, though the melting bulk material could prove to be a significant obstacle to the use of PFIB for this purpose.

5. Conclusions and Suggestions for Future Work

The overarching purpose of this project was the application of the PFIB to a number of different tasks in a variety of fields. The optical facet work was selected to make use of the versatility of the instrument and the more modern automation capacity available, as well as to provide potential value to both research and commercial applications. The backside circuit access project was selected to take advantage of the large currents available with an ICP ion source, and to produce a new method for the purposes of semiconductor failure analysis, prototyping, and reverse engineering. The heat transfer work was conducted with the hope of contributing to a burgeoning field of research and providing a useful platform for further investigation of nanoscale radiative heat transfer phenomena. The PFIB proved to be a useful and versatile tool for all of these applications, with many potential avenues for continued work.

5.1 Future Work

With the optical facet project providing a significant improvement in facet quality on the order of 3 dB and resulting in a functioning automated process capable of producing a facet every 30 seconds with minimal oversight, the use of PFIB for this application has promising implications. With this in mind, there are process improvements that ought to be considered. The automation routine could potentially be improved by implementing a continuous searching loop in order to eliminate the requirement for waveguides to be evenly spaced along the chip, though this would likely be somewhat detrimental in terms of speed and might result in a higher rate of failure. If the operator were to be sufficiently bold, a statement could be added to rotate and translate the chip such that operator participation would not be required between cutting the facets on one end of the

waveguides and the other. Another point of interest is that the work presented in this thesis used the automation routine at a 15 nA beam current. While the results in chapter 2 do indicate that 15 nA is a functional beam current to use, it is possible to see from the results obtained that 60 nA may be comparable in quality for a drastic reduction in time required.

With regard to the backside circuit access project, there is one primary avenue for improvement, this being the acquisition and use of a GIS suitable to the purpose of high aspect ratio milling. This would enable not only the use of GAE with a more even flux at high aspect ratios, but also with beam currents up to the maximum current available on the instrument. Further testing could then be conducted to establish the maximum etch rate. Additional testing could also be conducted on working devices.

Potential further work on the heat transfer project includes the complete characterization of existing test structures, further improvements to existing designs to reduce bridge sag and minimize gap width, and additional designs for feasible test structures.

References

[1] J. Melngailis, "Focused ion beam technology and applications," *Journal of Vacuum Science & Technology B: Microelectronics Processing and Phenomena,* vol. 5, no. 2, pp. 469-495, 1987.

[2] N. Bassim, K. Scott and L. A. Giannuzzi, "Recent advances in focused ion beam technology and applications," *MRS Bulletin,* vol. 39, no. 4, pp. 317-325, 2014.

[3] W. Van Heddeghem, S. Lambert, B. Lannoo, D. Colle, M. Pickavet and P. Demeester, "Trends in worldwide ICT electricity consumption from 2007 to 2012," *Computer Communications,* vol. 50, pp. 64-76, 2014.

[4] N. Jones, "How to stop data centres from gobbling up the world's electricity," *Nature,* vol. 561, pp. 163-166, 2018.

[5] M. McNerney, "The Data Center Dilemma: Is Our Data Destroying the Environment?," Data Center Knowledge, 19 April 2019. [Online]. Available: https://www.datacenterknowledge.com/industry-perspectives/data-center-dilemma-our-data-destroying-environment. [Accessed 2 April 2020].

[6] D. Thomson and e. al, "Roadmap on silicon photonics," *Journal of Optics,* vol. 18, no. 7, p. 073003, 2016.

[7] MarketWatch, "Silicon Photonics Market Size, Share 2020| Global Industry Analysis by Trends, Growth, Factors, Business Outlook, Competitive Strategies, Forecast till 2024," 28 January 2020. [Online]. Available: https://www.marketwatch.com/press-release/silicon-photonics-market-size-share-2020-global-industry-analysis-by-trends-growth-factors-business-outlook-competitive-strategies-forecast-till-2024-2020-01-28. [Accessed 2 April 2020].

[8] MarketsandMarkets, "Silicon Photonics Market by Product (Transceiver, Switch, Variable Optical Attenuator, Cable, Sensor), Application (Data Center, Telecommunications, Military & Defense, Medical and Life Sciences, Sensing), Component, and Geography - Global Forecast to 202," 13 December 2019. [Online]. Available: https://www.marketsandmarkets.com/Market-Reports/silicon-photonics-116.html. [Accessed 2 April 2020].

[9] M. Schnarrenberger, L. Zimmermann, T. Mitze, J. Bruns and K. Petermann, "Facet preparation of SOI waveguides by etching and cleaving compared to dicing and polishing," in *First IEEE International Conference on Group IV Photonics*, 2004.

[10] H. Baghsiahi, K. Wang, W. Kandulski, R. C. A. Pitwon and D. R. Selviah, " Optical Waveguide End Facet Roughness and Optical Coupling Loss," *J. Lightwave Technol.*, vol. 31, no. 16, pp. 2959-2968, 2013.

[11] C. Wu, "Etching Mirror Facets on SOI Optical Waveguides," TechBriefs , 1 June 2002. [Online]. Available: https://www.techbriefs.com/component/content/article/tb/supplements/ptb/briefs/29389. [Accessed 5 April 2020].

[12] L. G. Carpenter, H. L. Rogers, C. Holmes, J. C. Gates and P. G. R. Smith, "Facet machining of silica waveguides with nanoscale roughness without polishing or lapping," in *Conference on Lasers & Electro-Optics Europe & International Quantum Electronics Conference CLEO EUROPE/IQEC*, Munich, 2013.

[13] M. P. Mack and e. al, "Improvement of GaN-based laser diode facets by FIB polishing," *Electronics Letters*, vol. 34, no. 12, pp. 1315-1316, 1998.

[14] M. J. Cryan, Y.-L. D. Ho, P. S. Ivanov, P. J. Heard, J. Rorison and J. G. Rarity, "Chapter 18: FIB Etching for Photonic Device Applications," in *Nanofabrication Using Focused Ion and Electron Beams*, New York, Oxford University Press, 2012, pp. 553-583 (564).

[15] V. Callegari, U. Sennhauser and H. Jaeckel, "FIB Etching of InP for Rapid Prototyping of Photonic Crystals," in *Nanofabrication Using Focused Ion and Electron Beams*, New York, Oxford University Press, 2012, pp. 584-599 (594).

[16] L. Burnett and e. al, "Large volume serial section tomography by Xe Plasma FIB dual beam microscopy," *Ultramicroscopy*, vol. 161, p. 119–129, 2016.

[17] N. S. Smith and e. al, " High brightness inductively coupled plasma source for high current focused ion beam applications," *Journal of Vacuum Science and Technology B.*, vol. 24, no. 6, pp. 2902-2906, 2006.

[18] E. Suhir, "Predicted Bow of Plastic Packages of Integrated Circuit (IC) Devices," in *Thermal Stress and Strain in Microelectronics Packaging*, New York, Van Nostrand Reinhold, 1993, pp. 385-409.

[19] K. S. Wills and S. Perungulum, "Deprocessing and Sample Preparation," in *Microelectronics Failure Analysis Desk Reference (6th Edition)*, Stafford, ASM International, 2011, pp. 397-416.

[20] C. Volkert and A. Minor, "Focused Ion Beam Microscopy and Micromachining," *MRS Bulletin,* vol. 32, pp. 389-399, 2007.

[21] Orsay Physics, "Scientific Overview: What is FIB," Tascan Orsay Holding, [Online]. Available: http://www.orsayphysics.com/what-is-fib. [Accessed 27 July 2020].

[22] R. Gauvin, P. Hovongton, D. Drouin, P. Horny, H. Demers and A. R. Couture, *CASINO.*

[23] N. Bassim and K. G. L. A. Scott, "Recent advances in focused ion beam technology and applications," *MRS Bulletin,* vol. 39, no. 4, pp. 317-325, 2014.

[24] L. W. Swanson, "Use of the liquid metal ion source for focused beam applications," *Applied Surface Science,* vol. 76/77, pp. 80-88, 1994.

[25] N. S. Smith, J. A. Notte and A. V. Steele, "Advances in source technology for focused ion beam instruments," *MRS Bulletin,* vol. 39, pp. 329-335, 2014.

[26] M. T. Postek, A. E. Vladar, J. Kramar, L. A. Stern, J. Notte and S. McVey, "Helium Ion Microscopy: a New Technique for Semiconductor Metrology and Nanotechnology," in *AIP Conference Proceedings*, 2007.

[27] D. C. Cox, Introduction to Focused Ion Beam Nanometrology, Morgan & Claypool, 2015.

[28] C. Perez-Martinez, S. Guilet, J. Gierak and P. Lozano, "Ionic liquid ionsources as a unique and versatile option in FIB applications," *Microelectronic Engineering,* Vols. 2088-2091, 2011.

[29] S. Rubanov, *Doctoral Thesis: The Study of the Focused Ion Beam Induced Damage in Semiconductor Materials,* Sydney: Univeristy of New South Wales, 2002.

[30] O. Wilhelmi and H. Mulders, "Focused Ion Beam and DualBeam Technology Applied to Nanoprototyping," in *Nanofabrication using Focused Ion and Electron Beams*, New York, Oxford University Press, 2012, pp. 381-409.

[31] J. J. L. Mulders, D. A. M. de Winter and W. J. H. C. P. Duinkerken, "Measurements and calculations of FIB milling yield of bulk metals," *Microelectronic Engineering,* vol. 84, no. 5, pp. 1540-1543, 2007.

[32] ThermoFisher Scientific, "Nanofabrication and Rapid Prototyping with DualBeam Instruments: Application Note," 2018.

[33] V. Friedli, H. D. Wanzenbock and I. Utke, "Gas Injection Systems for FEB and FIB Processing Theory and Experiment," in *Nanofabrication using Focused Ion and Electron Beams: Principles and Applications*, New York, Oxford University Press, 2012, pp. 126-183.

[34] I. Utke, P. Hoffmann and J. Melngailis, "Gas-assisted focused electron beam and ion beam processingand fabrication," *Journal of vacuum science & technology B,* vol. 26, no. 4, pp. 1197 - 1276, 2008.

[35] Labtech, "Kleindiek GIS-EM gas injection system," Labtech, [Online]. Available: https://www.labtech-em.com/em/kleindiek-gis-em-gas-injection-system. [Accessed 28 July 2020].

[36] V. Ray, "Gas delivery and virtual process chamber concept for gas-assisted material processing in a focused ion beam system," *Journal of Vacuum Science & Technology B,* 2004.

[37] L. R. Harriot, "Digital scan model for focused ion beam induced gas etching," *Journal of Vacuum Science & Technology B,* vol. 11, no. 6, pp. 2012-2015, 1993.

[38] J. C. Cuevas and F. J. J. García-Vidal, "Radiative Heat Transfer," *ACS Photonics,* 2018.

[39] R. Torrance and D. James, "Reverse Engineering in the Semiconductor Industry," in *Custom Integrated Circuits Conference,* 2007.

[40] J. Jagerska, Thesis: Dispersion Properties of Photonic Crystals and Silicon Nanostructures Investigated by Fourier-Space Imaging, UiT the Arctic University of Norway, 2011.

[41] R. G. Hunsperger, Integrated Optics: Theory and Technology 6th Edition, Newark: Springer, 2009.

[42] D. Thomson and e. al, "Roadmap on silicon photonics," *Journal of Optics,* vol. 18, no. 7, p. 073003, 2016.

[43] V. J. Gadgil, "Applications of FIB for Rapid Prototyping of Photonic Devices, Fabrication of Nanosieves, Nanowires, and Nanoantennas," in *Nanofabrication Using Focused Ion and Electron Beams*, New York, Oxford University Press, 2012, pp. 600-616.

[44] S. Norris, *Comparison OF Beam-Induced Damage from Xenon and Gallium Focused Ion Beams*, Hamilton, Ontario: McMaster University, 2019.

[45] C. G. H. Roeloffzen, M. Hoekman, E. J. Klein, L. S. Wevers, R. B. Timens, D. Marchenko, D. Geskus, R. Dekker, A. Alippi, R. Grootjans, A. van Rees, R. M. Oldenbeuving, J. P. Epping, R. G. Heideman, K. Wörhoff, A. Leinse, D. Geuzebroek, E. Schreuder, . P. . W. L. van Dijk, I. Visscher, C. Taddei, Y. Fan, C. Taballione, Y. Liu, D. Marpaung, L. Zhuang, M. Benelajla and K. J. Boller, "Low-Loss Si3N4 TriPleX Optical Waveguides: Technology and Applications Overview," *IEEE JOURNAL OF SELECTED TOPICS IN QUANTUM ELECTRONICS*, vol. 24, no. 4, 2018.

[46] M. J. Lagos and P. E. Batson, "Thermometry with Subnanometer Resolution in the Electron Microscope Using the Principle of Detailed Balancing," *Nano Letters*, vol. 18, no. 7, p. 4556–4563, 2018.

[47] Protochips, "TEM Sample Supports: E-Chips," Protochips, 2020. [Online]. Available: https://www.protochips.com/products/e-chips/. [Accessed 28 July 2020].

[48] M. Mecklenburg, W. A. Hubbard, E. R. White, R. Dhall, S. B. Cronin, S. Aloni and B. C. Regan, "Nanoscale temperature mapping in operating microelectronic devices," *Science*, vol. 347, no. 6222, pp. 629-632, 2015.

[49] R. Anufriev, A. Ramiere, J. Maire and M. Nomura, "Heat guiding and focusing using ballistic phonon transport in phononic nanostructures," *Nature Communications*, vol. 8, no. 1, p. 15505, 2017.

[50] F. I. Chang, R. Yeh, G. Lin, P. B. Chu, E. Hoffman, E. J. J. Kruglick and K. S. J. Pister, "Gas-phase silicon micromachining with xenon dffluoride," in *Micromachining and Microfabrication*, Austin , 1995.

[51] I. Utke, S. Moshkalev and P. Russell, Nanofabrication Using Focused Ion and Electron Beams: Principles and Applications, New York: Oxford University Press, 2012.

[52] O. Wilhelmi, S. Reyntjens, L. Roussel, D. J. Stokes and D. H. W. Hubert, "High Resolution Nanolithography Using Focused Ion Beam Scanning Electron Microscopy (FIB SEM)," in *NSTI-Nanotech*, 2007.

[53] M. J. Lagos, A. Trügler, U. Hohenester and P. E. Batson, "Mapping vibrational surface and bulk modes in a single nanocube," *Nature*, vol. 543, no. 7646, p. 529–532, 2017.

[54] J. F. Ziegler, *SRIM and TRIM*, 2013.

[55] K. Erdinger and T. Kraus, "Modelling of focusion ion beam induced surface chemistry," *Journal of Vacuum Science & Technology B*, vol. 18, no. 6, pp. 3190-3193, 2000.